A COMPARATIVE EVALUATION FOR LIVER SEGMENTATION FROM SPIR IMAGES AND A NOVEL LEVEL SET METHOD USING SIGNED PRESSURE FORCE FUNCTION

A Thesis Submitted to
the Graduate School of Engineering and Sciences of
İzmir Institute of Technology
in Partial Fulfillment of the Requirements for the Degree of

DOCTOR OF PHILOSOPHY

in Electronics and Communication Engineering

by
Evgin GÖÇERİ

July 2013
İZMİR

We approve the thesis of **Evgin GÖÇERİ**

Examining Committee Members:

Prof. Dr. Aydın AKAN
Department of Electrical and Electronics Engineering
İstanbul University

Prof. Dr. Cüneyt GÜZELİŞ
Department of Electrical and Electronics Engineering
İzmir University of Economics

Assist. Prof. Dr. Şevket GÜMÜŞTEKİN
Department of Electrical and Electronics Engineering
İzmir Institute of Technology

Assist. Prof. Dr. Engin ÖZÇİVİCİ
Depertment of Mechanical Engineering
İzmir Institute of Technology

Assist. Prof. Dr. M. Zübeyir ÜNLÜ
Department of Electrical and Electronics Engineering
İzmir Institute of Technology

12 July 2013

Assist. Prof. Dr. M. Zübeyir ÜNLÜ
Supervisor,
Department of Electrical and Electronics Engineering
İzmir Institute of Technology

Prof. Dr. Acar SAVACI
Head of the Department of
Electrical and Electronics Engineering

Prof. Dr. R. Tuğrul SENGER
Dean of the Graduate School
Engineering and Sciences

ACKNOWLEDGEMENTS

I would like to express my sincere gratitude to my committee members, Prof. Dr. Cüneyt GÜZELİŞ, Assist. Prof. Dr. Şevket GÜMÜŞTEKİN and to my advisor, Assist. Prof. Dr. M. Zübeyir ÜNLÜ for their contributions, guidance and recommendations throughout my thesis study.

I thank my parents for their support during my life.

ABSTRACT

A COMPARATIVE EVALUATION FOR LIVER SEGMENTATION FROM SPIR IMAGES AND A NOVEL LEVEL SET METHOD USING SIGNED PRESSURE FORCE FUNCTION

Developing a robust method for liver segmentation from magnetic resonance images is a challenging task due to similar intensity values between adjacent organs, geometrically complex liver structure and injection of contrast media, which causes all tissues to have different gray level values. Several artifacts of pulsation and motion, and partial volume effects also increase difficulties for automatic liver segmentation from magnetic resonance images. In this thesis, we present an overview about liver segmentation methods in magnetic resonance images and show comparative results of seven different liver segmentation approaches chosen from deterministic (K-means based), probabilistic (Gaussian model based), supervised neural network (multilayer perceptron based) and deformable model based (level set) segmentation methods. The results of qualitative and quantitative analysis using sensitivity, specificity and accuracy metrics show that the multilayer perceptron based approach and a level set based approach which uses a distance regularization term and signed pressure force function are reasonable methods for liver segmentation from spectral pre-saturation inversion recovery images. However, the multilayer perceptron based segmentation method requires a higher computational cost. The distance regularization term based automatic level set method is very sensitive to chosen variance of Gaussian function. Our proposed level set based method that uses a novel signed pressure force function, which can control the direction and velocity of the evolving active contour, is faster and solves several problems of other applied methods such as sensitivity to initial contour or variance parameter of the Gaussian kernel in edge stopping functions without using any regularization term.

ÖZET

SPIR GÖRÜNTÜLERİNDE KARACİĞER BÖLÜTLEMENİN KARŞILAŞTIRMALI DEĞERLENDİRİLMESİ VE İŞARETLİ BASKI KUVVET FONKSİYONU KULLANAN YENİ BİR DÜZEY KÜMESİ YÖNTEMİ

Karaciğerin bitişik organlar ile benzer gri seviye değerlerine sahip olması, belirgin bir şeklinin olmaması ve tüm dokuların farklı gri seviye değerlerinde olmasına sebep olan kontrast maddenin vücuda verilmesi gibi nedenlerden dolayı manyetik rezonans görüntülerinden karaciğer bölütlemesi için dayanıklı bir yöntem geliştirmek zor bir iştir. Titreşim ve hareketten oluşan çeşitli yapay dokular ve kısmi hacim etkisi manyetik rezonans görüntülerinden otomatik karaciğer bölütleme işleminin zorluklarını arttırmaktadır. Bu tez çalışmasında, bilimsel yazında öne çıkan manyetik rezonans görüntüleri ile karaciğer bölütlemesi yöntemlerini sunmakta ve deterministik (öbekleme tabanlı), olasılıksal (Gauss model tabanlı), denetimli sinir ağı (çok katmanlı algılayıcı tabanlı) ve deformable model tabanlı (düzey kümesi) bölütleme yöntemlerinden seçilen yedi farklı karaciğer bölütleme yaklaşımının karşılaştırmalı sonuçlarını göstermekteyiz. Özgüllük, duyarlılık ve doğruluk ölçütleri kullanılarak yapılan nicel ve nitel inceleme sonuçları göstermektedir ki, bazı kesitler üzerinde çok katmanlı algılayıcı ve düzey kümesine dayalı yaklaşımlar yağ baskılı görüntülerde (spectral pre-saturation inversion recovery images) kabul edilebilir yöntemlerdir. Fakat çok katmanlı algılayıcı tabanlı bölümleme yönteminin ihtiyaç duyduğu çalışma zamanı çok fazladır. Uzaklık düzenleme terimine dayalı otomatik düzey kümesi yöntemi Gauss fonksiyonu için seçilen varyans değerine çok duyarlıdır. Aktif çevritin evrimini ve hızını kontrol edebilen, yeni bir işaretli baskı kuvvet fonksiyonu kullanarak önerdiğimiz düzey kümesi yöntemi, ilk aktif çevrit evrimine veya kenar durdurma fonksiyonundaki Gauss çekirdek fonksiyonun varyans değerine duyarlılık gibi çeşitli problemleri herhangi bir düzenleyici terim kullanmadan çözebilmektedir.

To my sister

TABLE OF CONTENTS

LIST OF FIGURES

Figures **Page**

LIST OF TABLES

LIST OF ABBREVIATIONS

ANN	Artifical Neural Network
CT	Computed Tomography
DRLSE	Distance Regularized Level Set Evolution
EM	Expectation Maximization
FID	Free Induction Decay
FTC	Fast Two Cycles
GMM	Gaussian Mixture Model
IVC	Inferior Vena Cava
LBF	Local Binary Fitting
LSM	Level Set Method
LSF	Level Set Function
MLP	Multi-layer Perceptron
MRI	Magnetic Resonance Image
NMR	Nuclear Magnetic Resonance
PDE	Partial Differential Equation
PET	Positron Emission Tomography
RF	Radio Frequency
SBGFRLS	Selective Binary Gaussian Filtering Regularized Level Set
SPECT	Single Photon Emitted Computed Tomography
SPF	Signed Pressure Force
SPIR	Spectral Pre-saturation with Inversion Recovery
VLSM	Variational Level Set Method

CHAPTER 1

INTRODUCTION

Digital imaging technologies have become indispensable components for clinical procedures. Major advances in the field of medical imaging and computer technology have created opportunity for quantitative analyses of medical images and provided powerful techniques to probe the structure, pathology and function of the human body. The availability of many different imaging modalities increased the requirement for significant innovations to obtain accurate and fast results in all aspect of image processing.

Some of the current researches in medical imaging are focused on pathology diagnosis of abdominal organs such as spleen, liver, kidney and gallbladder. Segmentation is an important step for radiological operations such as diagnosis, study of anatomical structures, quantification of volumes of tissues, treatment planning, localization of pathologies and computer aided surgery. Manual segmentation process is not only tedious and time consuming due to the high number of slices but also depends on the skills and experience of the operator. For example, Figure 1.1 shows liver edges identified manually by different radiologists and also by the same radiologist at a different time on a sample Magnetic Resonance Image (MRI). Therefore, automatic segmentation is a fundamental step.

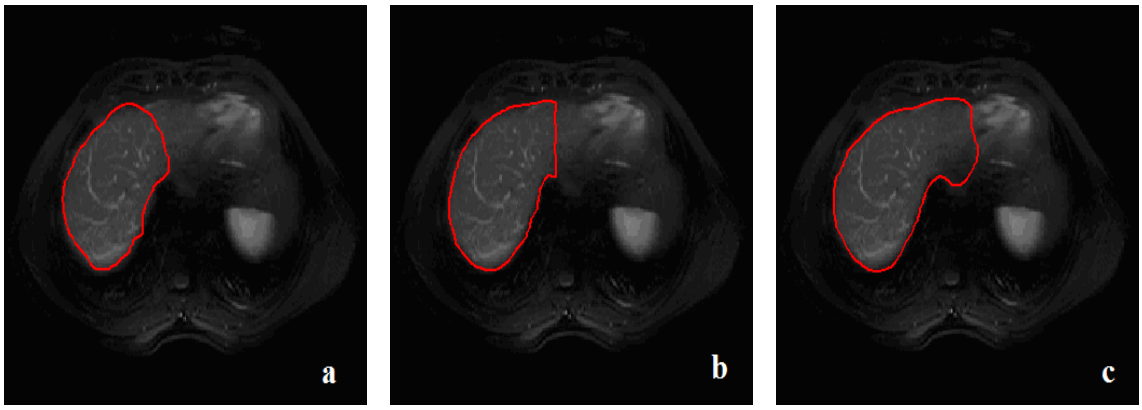

Figure 1.1. Liver edges defined by radiologist R1 (a), by radiologist R2 (b) and by radiologist R2 at different time (c)

Many different segmentation techniques have been proposed and the advances in this area (Zhang 2006) increase each year. However, currently there is no segmentation technique that gives successful results for all type of medical images, and even for the same organ in different imaging modalities. For example, liver and brain segmentation requirements are different. Also, the requirements for liver segmentation from Computed Tomography (CT) images are different with its segmentation from MRIs. Therefore, organ segmentation from medical images is still an open problem and liver segmentation is much more challenging task among other organ segmentations due to several reasons. One of them is high intra- and inter-patient variability of liver shapes. Another reason is that the artifacts such as beam hardening, reconstruction artifacts and noise cause image quality degradation while movements of patients cause blurred boundaries. Also, injection of contrast media and varying conditions for machine setup lead to very high variabilities of intensity values both in datasets of different patients and even in each slice of the same dataset of a patient. Moreover, liver has different positions and very similar intensity values with the adjacent organs that are kidney and heart.

1.1. Problem Description

Liver imaging can be performed with ultrasonography, CT and MRI. When MRIs and CT images are compared, MRIs have higher contrast resolution than CT images. MRIs have many advantages for image navigation, such as good soft tissue contrast, free form ionizing radiation and multi-planar capabilities. However, the automated segmentation of MRIs is more challenging than CT images. Because, smaller edge magnitudes in MRIs cause edge-based segmentation algorithms to be more complicated compared to CT images. Also, partial volume effects and artifacts due to motion and pulsation in MRIs lead to more challenges in automatic liver segmentation. Therefore, in comparison with CT-based liver segmentation approaches (Tsai 1994, Husain and Shigeru 2000, Lee et al.2003, Bae et al.1993, Gao et al.1996, Lim et al.2006, Masumoto et al.2003, Montagnat and Delingette 1996, Chou et al.1995, Gao et al.2000, Heimann and Meinzer 2006, Heimann et al.2007, Pohle and Toennies 2001, Rusko et al.2007, Bekes et al.2007, Lee et al.2007, Selver et al.2008, Kainmueller et al.2007, Park et al.2003, Shitong et al.2007, Suzuki et al.2010, Linguraru et al.2010,

Goryawala et al.2011, Wang et al.2011, Oliveira et al.2011), there exist fewer studies in the literature for liver image segmentation from MRIs. Example abdominal MRIs, which are from T2 weighted Spectral Pre-saturation with Inversion Recovery (SPIR) data sets, are given in Figure 1.2 to show why liver segmentation is a challenging task because of gray level similarities.

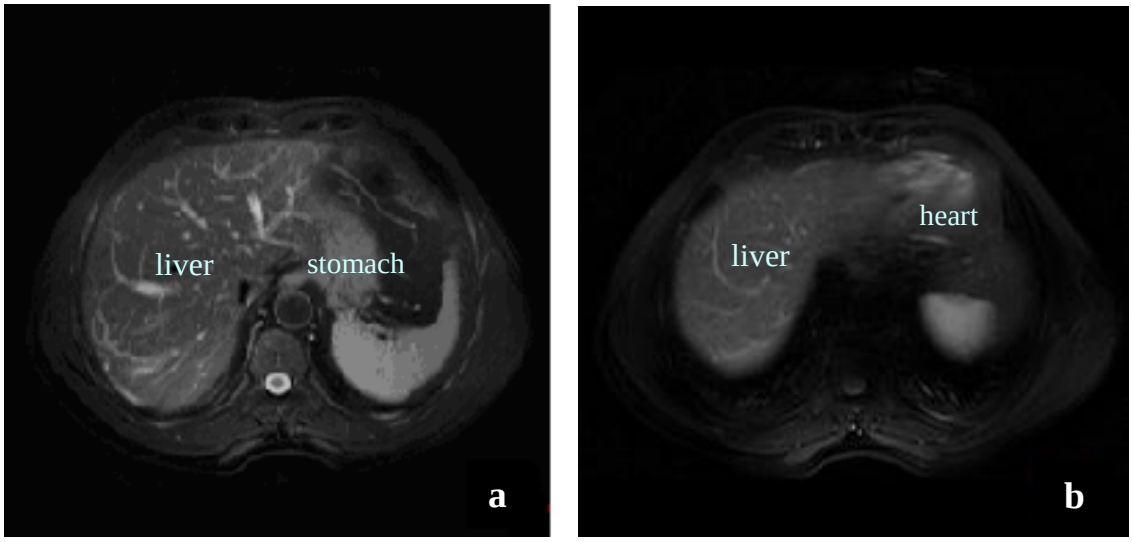

Figure 1.2. Example images show why segmentation of the liver organ from SPIR images is a challenging process because of gray level similarities. Gray level similarity between liver and stomach (a), and between liver and heart (b)

Main Magnetic Resonance (MR) based image segmentation approaches appeared in the literature can be listed as fuzzy c-means classification (Positano et al. 2007, Lu et al.2007), graph-cut (Massoptier and Casciaro 2007), Level Set Method (LSM) (Hermoye et al. 2005, Cheng et al. 2008), synchronized oscillator network (Strzelecki et al. 2007), active shape model (Platero et al. 2008, Fenchel et al. 2008), watershed (Rafiee et al 2009), iterative quadtree decomposition (Dongxiang and Tiankun 2009), Gaussian model and markov random field (Jha et al.2010), modified region growing (Gloger et al. 2010), and the application of free form registration on manually segmented CT images (Tang and Wang 2010). In the present literature, each proposed method for liver segmentation using MRIs has some problems such as over/under segmentation or leakage problems (Chen et al. 2009, Dongxian and Tiankun 2009, Lu et al. 2007, Positano et al. 2007), or testing with only a few data sets (Gloger et al. 2010, Massoptier and Casciaro 2007) or having complex calculations as in active

contour based approaches (Tang and Wang 2010). Neural network based methods have also been used for liver recognition in MRIs as in (Rafiee et al. 2009). In this approach, the abdominal MRIs are partitioned to subregions using watershed transform. Then a feed forward neural network is used to extract liver features in training stage. These features are used in liver recognition afterwards. However, the MRI modality characteristics used in the study are not clearly given.

There exists no method, which is capable of solving all the problems of different modality characteristics, atypical liver shapes and similar gray values with adjacent tissues at the same time. The methods in the literature can not cope with all the variations in MR data sets. Therefore, there is need for an accurate and efficient automatic liver segmentation method to work on MR sequences. Also, it should be noted that T2 weighted SPIR datasets have not been used for liver segmentation until now. However, SPIR images are capable of visualizing liver vessels better. Then the segmented liver images can be used to label hepatic and portal veins and then to obtain Couinaud segments (Couinaud 1999) as shown in Figure 1.3. Because, the importance of the functional anatomy of the human liver has increased for radiologists in many cases such as requirement of an accurate pre-operative localization of lesions or estimation of the volume of each liver segment to plan living donor liver transplantation.

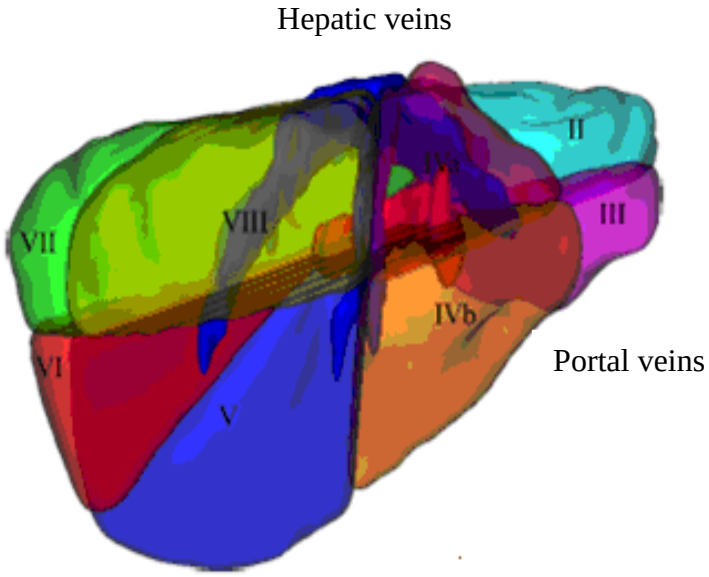

Figure 1.3. Functional Anatomy of Liver: Couinaud segments. Portal vein and hepatic veins define the segments except segment I, which is drained by cava vein (Source: Oliveira et al.2011)

Figure 1.4 shows segmental anatomy of the portal veins on a liver organ (Lafortune et al. 1991). Each number indicates different segments.

Figure 1.4. Segmental anatomy of the portal veins
(Source: Lafortune et al. 1991)

1.2. Liver Segmentation Approaches Using CT Images in the Literature

Many different automatic and semi-automatic techniques have been proposed and implemented for liver segmentation by using CT data sets in the literature (Mharib et al. 2012). As an example, Figure 1.5 shows original images, highlighted liver regions and segmented liver images from three different slices of an abdominal CT data set.

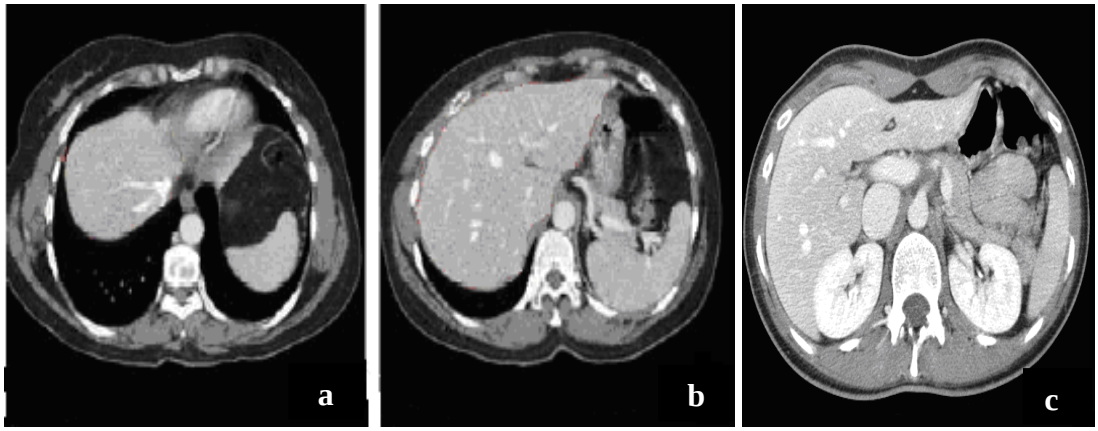

Figure 1.5. Different liver slices from a CT data set. Original images (a,b,c); Liver regions surrounded with red color (d,e,f); Segmented liver organ (g,h,i)

(cont. on next page)

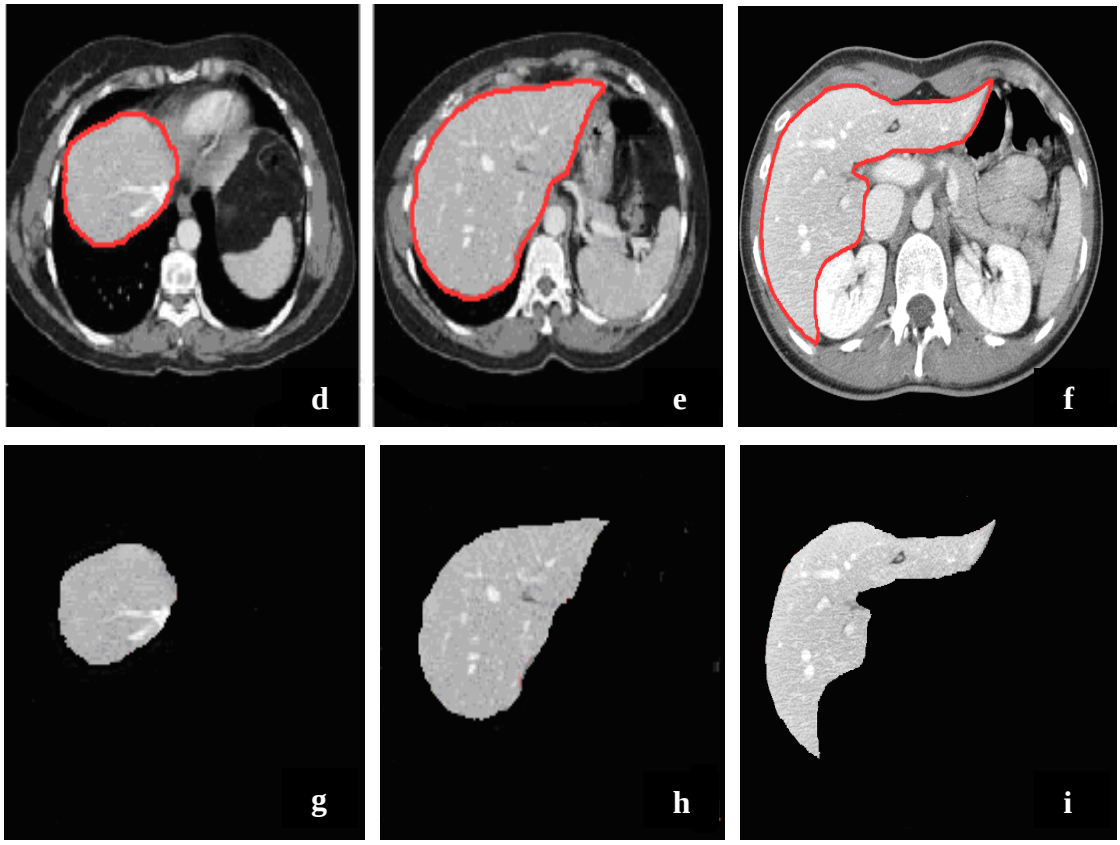

Figure 1.5. (cont.)

We can group some of liver segmentation methods from CT images as neural networks based (Tsai 1994, Husain and Shigeru 2000, Lee et al.2003), morphological operation based (Bae et al.1993, Gao et al.1996, Lim et al.2006, Masumoto et al.2003) and deformable models based approaches (Montagnat and Delingette 1996, Chou et al.1995, Gao et al.2000, Heimann et al.2006, Heimann et al.2007, Soler et al.2005). However, the problems originated from geometrically complex liver structure, datasets with low contrast adjacent tissues and various modality characteristics are not handled together in these methods. Therefore, these methods do not deal with all the variations in CT datasets at the same time.

1.3. Liver Segmentation Approaches Using MRIs in the Literature

To our knowledge, there is no a review study on liver MRI segmentation methods. Also, we have observed that there exist only a few studies for liver segmentation from MRIs when we searched. One of them is (Nowozin and Lixu 2005)

that applies three steps, which are location of a seed region, application of the fast marching method and initialization of a level set based segmentation. The first approximation for the shape of the liver is performed by the fast marching method. This shape is used for the initialization step. Segmentation results have been improved. However, drawing of conclusions is possible with more research for this study related to the performance of the algorithm in case the segmented objects have a different and atypical shape.

Another method for liver segmentation from MRIs is presented in (Hermoye et al. 2005) to determine liver volume in living liver transplant donors. The actual graft volume is inferred by its weight value and it is assumed that the liver has a unit density in this study, which uses a level set technique. As identified by the authors, manual delineations and corrections of the liver segments are required after the segmentation method.

Synchronised oscillators network based 3D liver MRI segmentation method (Strzelecki et al. 2007) is another approach. An oscillator network is defined by two differential equations. Oscillators are connected to form a three dimensional network since the network dimension is equal to the analyzed image and each oscillators represent a single pixel. Every oscillator is connected with a global inhibitor, which receives information from oscillators and can inhibit the network. Because of these local excitatory connections, an oscillator spreads its activity over to the oscillator group that represent image object. Synchronization of this group is provided by this way. Each region is represented by different oscillators groups.

In (Lu et al. 2007), liver nodule detection is performed using MRI. Fuzzy c-means (c=3) classification is used for nodule, vessel and parenchyma segmentation. Smoothing is performed as the next step using morphological operations in this study. The method should be investigated for different resolutions and applied to more than two patients. Another fuzzy c-means (c=2) based liver MRI segmentation method has been proposed in (Positano et al. 2007) for assessment of iron overloaded in liver. This method achieves classification of an image dataset by calculating a fuzzy membership measure at each pixel for two classes, which are parenchyma and vessels in this study. K-means and fuzzy c-means based methods are not directly adapted to noisy abdominal images.

A graph-cut technique has been applied for liver segmentation (Massoptier and Casciaro 2007). The graph is designed as composed by vertices, which represent voxels,

and edges, which connect these vertices. The energy function is minimized by summing the weights of cut edges. The energy function consists of a region term (which assigns penalties by using neighborhood context and also labels each voxel as background or object region) and a boundary term (which assigns penalties by using the dissimilarity values of neighborhood voxels).

The other approach to segment the liver organ from MRIs is explained in (Platero et al. 2008). This anisotropic diffusion processing based method is performed without using a control parameter. Not only edge detection, analysis of histograms and binary morphological image processing techniques but also active contour evolution has been implemented for the purpose of liver segmentation by the authors. The luminance variance between liver and its closest neighborhood has been used to evaluate the active contours. The required computation time for a volume of 350x250x55 pixels is given as 28s for diffusive filtering and morphological post-processing operations, and 6s is given for evolution of the active contour. It is identified in the paper that the Hausdorff distance value between the edge of the segmented image data and the edge of the manually segmented ground truth has been used to validate the segmentation result. The result is 2.3 mm for 95% percentile.

In (Cheng et al. 2008), a variational level set technique that incorporates prior knowledge of the liver shape into the improved Chan-Vese's method has been proposed. Usually, the boundary parts of the liver are not clear in MRIs because of liver movement and blood flow. Also, inhomogen intensities exist, where the Chan-Vese model does not work well. Therefore, the authors introduce the feature image according to intensity values of objects. The proposed algorithm needs an initial segmentation image, which has been obtained by implementing the Chan-Vese method. However, there are some flaws such as over segmenting and leakage due to the low quality of the liver in abdominal MRIs. The problem has been solved by using prior shape knowledge and the level set approach in this study. It is identified by the authors that the experimental results from MRI data sets reveal that the level set based shape prior technique can segment the liver precisely. However, precision and running time statistics are not presented in this study.

Fenchel et al. used active shape model for liver segmentation to reconstruct liver shape and position from MRI slices (Fenchel et al. 2008). The active shape model is created from a training set of liver segmentations from a group of volunteers. The training set is set up with semi-manual segmentations of T1-weighted volumetric MRIs.

Searching for the optimal shape model that best fits to the image data is done by maximizing a similarity measure that is based on local appearance at the surface. Hovewer, for high-quality clinical liver segmentations, more generalizability of the model search to unknown datasets have to be integrated for this method.

Chen et al. proposed a multiple-initialization, multiple-step LSM to overcome the over-segmentation and leakage problems (Chen et al. 2009). In this method, a rough contour of the liver is obtained by combining multiple initialized curves, which are first evolve separately, and a convex hull algorithm. Contour evolution is performed by using LSMs and the fast marching methods. Precise boundaries of the liver are obtained by evolving the contour with global level set smoothing. An important difficulty for multiple-initialization of LSMs is to determine the number of initializations automatically. Therefore, under-segmentation problem occurs at lower sharp corners because of the low-gradient of the lower half of the liver.

Starting from a seed point or a ranking order of liver area, a segmentation result of liver in MRI has been obtained by a quadtree decomposition, regional morphology operation and ordering of ROI in (Dongxiang and Tiankun 2009). The main problem with quadtree decomposed liver images is that the zigzag outline of the initial segmented image does not conform to smooth human tissues.

A neural network based approach has been used for liver detection in MRIs in (Rafiee et al. 2009). In this method, the abdominal MRIs are partitioned to some regions and feed forward neural network is used to extract liver features in training stage. These features are used in liver recognition. An intensity-based liver segmentation method in (Ruskó and Bekes 2010), which uses probabilistic approach to increase the precision of the segmentation, has been proposed. In this study, the probabilistic model is built using built by using sixty manually contoured CT images. Different intensity statistics at different parts of the liver is used after the partitioning of the model according to the functional anatomy of the liver. The used approach provides a modality independent model by registration, which exploits some characteristics of LAVA images. As identified by the authors, although the presented model in this work does not depend on modality, some characteristics of LAVA images, which shall be eliminated for adaptation of the segmentation algorithm for a wide range of MRIs, are exploited by the model fitting.

In contrast to previous methods for segmentation of the liver from MR data sets, available MR channel information of different weight values are used and liver tissue

with position probabilities in a probabilistic framework is formulated by the authors in (Gloger et al. 2010). The automatic three dimensionals liver segmentation approach is based on a modified region growing algorithm and a further thresholding method has been proposed. In this liver approach, multiclass linear discriminant analysis is applied as a dimensionality reduction method and probability maps are generated and used for segmentation. It is identified by the authors that the proposed segmentation method gives successful results in the automatic liver segmentation of three dimensionals MR data sets and provides important potential for the assistance of volumetric analysis of the liver.

In (Tang and Wang 2010), liver is extracted from CT images by hand. Active contour is used to extract liver region from MRIs. As the next step, B-spline based free form deformation is used to register the extracted liver regions from CT and MRIs.

A clustering algorithm for liver lesion segmentation of diffusion weighted MRIs incorporates spatial information and geometric constraint in (Jha et al. 2010). Finite Gaussian Mixture Model is applied for liver segmentation but this model does not take spatial information into account. There might be pixels whose intensities are different from other pixels in the same region. Therefore, Markov Random Field is used to account spatial information in this study.

The proposed method in (Chen et al. 2010) applies K-means based liver segmentation approach by using Open-MRIs. The authors apply K-means method before implementation of Graph-Cut algorithm to identify liver pixels.

Although there are only a few studies for liver MRI segmentation, it has been observed that different algorithms with different MRI modalities have been applied for liver segmentation. Each of them has their own advantages and disadvantages in terms of accuracy, robustness or computational cost. However, SPIR images have not been used until now.

1.4. The Aim of the Thesis

In this thesis, the aim is to make a comparison of various approaches and to present their experimental results for liver segmentation on abdominal MRIs. Six different approaches have been implemented and their results from SPIR datasets are presented in this work. These methods include probabilistic, deterministic, supervised and unsupervised approaches with different techniques. In addition, we propose a novel

level set based liver segmentation algorithm by using a Signed Pressure Force (SPF) function and automatically obtained adaptive weight values on pre-processed images. The methods that are presented in this thesis for liver segmentation are as follows:

- The first method is a model based unsupervised classifier that uses a probabilistic approach. Gaussian Mixture Model (GMM) with Expectation Maximization (EM) has been applied iteratively in this method to get optimal results.
- The second method performs the liver segmentation process similar to the first method. However, K-means clustering has been applied iteratively instead of the probabilistic GMM algorithm in this method.
- The more complex third method uses a supervised classifier that is based on neural networks. Multi-Layer Perceptron (MLP) has been applied to classify three different features that are extracted from current and previously segmented images to increase segmentation performance in this method.
- The fourth implemented method is an unsupervised classifier that is based on a pixel switching mechanism. This method uses a Fast Two Cycles (FTC) algorithm that is similar to classical level set technique. However, this approach is applied without using any Partial Differential Equation (PDE).
- The FTC algorithm has been applied for all slices in a dataset without any user interaction in the fifth presented method. This automatic FTC based liver segmentation method uses pre-processed images.
- The next one is a Variational LSM (VLSM) that is applied by using PDE with a distance regularization term to avoid re-initialization of the Level Set Function (LSF) and an SPF function to stop curve evolution efficiently. We have developed this method after implementation and observation of liver segmentation results from three different VLSMs, which use either a regularization term or an SPF function.
- The last method that we have developed is a novel level set based technique. It has been implemented to overcome all challenges for the liver segmentation from SPIR images. A new SPF function that includes both edge and region information has been proposed in this segmentation method. Also, instead of to use constant coefficients for each term of the proposed PDE, the weight values

are computed automatically by using geometric properties of the active contour at each iteration for each slice.

The results of quantitative and qualitative comparison of the seven different liver segmentation methods (K-means, GMM, MLP and level set based methods) show that the developed PDE based level set algorithm with the proposed SPF function gives efficient results from SPIR datasets in terms of accuracy and computational cost according to both qualitative and quantitative performance analyses. The quantitative performance of all methods presented in this thesis is evaluated in terms of sensitivity, specificity, accuracy and required processing time.

1.5. The Organization of the Thesis

This dissertation is organized as follows; Chapter 2 includes the background information about anotomy of the human abdomen, abdominal imaging and image segmentation techniques. The properties of the data sets that are used in this thesis are and applied approaches for liver segmentation from MRIs are explained in Chapter 3. The proposed segmentation method is presented in Chapter 4. Experimental results of all implemented methods in this thesis are given in Chapter 5. Performance analyses of the methods are explained in Chapter 6. Finally, conclusions are presented in Chapter 7.

CHAPTER 2

BACKGROUND

2.1. Anatomy of the Human Abdomen

The abdomen is a roughly cylindrical chamber constitutes the part of the human body between the inferior margin of the thorax at the thoracic diaphragm and the superior margin of the pelvis at the pelvic brim (Figure 2.1.a). The inferior thoracic aperture is the superior opening to the human abdomen and it is closed by the diaphragm. The boundaries of the abdominal cavity is the abdominal wall. The human abdominal wall, which is a muscular structure protected by fascia, skin and fat, is continuous with the pelvic wall at the pelvic inlet. Abdominal viscera, which include major elements of the gastrointestinal system, major neurovascular structures, the spleen, kidneys and ureters, are either suspended in the peritoneal cavity by mesenteries or are located between the cavity and the musculoskeletal wall (Figure 2.1b) (Drake 2004).

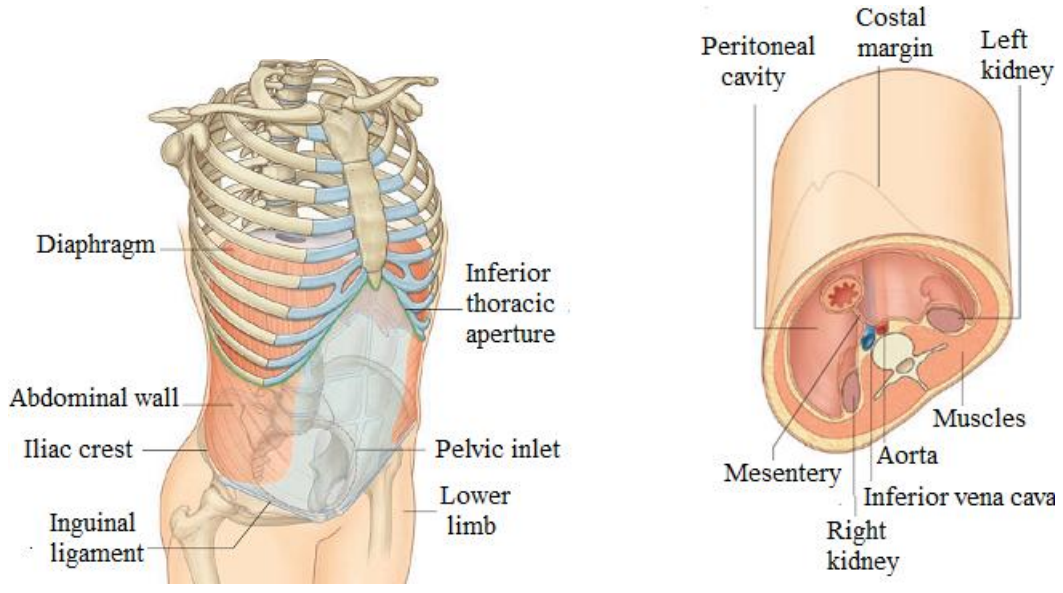

(a) (b)

Figure 2.1. Human abdomen boundaries (a); Arrangement of abdominal contents at inferior view (b) (Source: Drake 2004)

Functionally, the human abdomen anatomy comprises most of the alimentary tract. This is the part of the body, where the food is digested and the nutrients are absorbed. The alimentary tract in the abdomen includes the esophagus, the jejunum, the stomach, the duodenum, the cecum, the ileum, the appendix, the sigmoid colon, the transverse, ascending and descending colons and the rectum. Other than the organs, which are directly associated with digestion, the vital organs in the abdomen include the liver, the kidneys, the spleen and the pancreas (Figure 2.2).

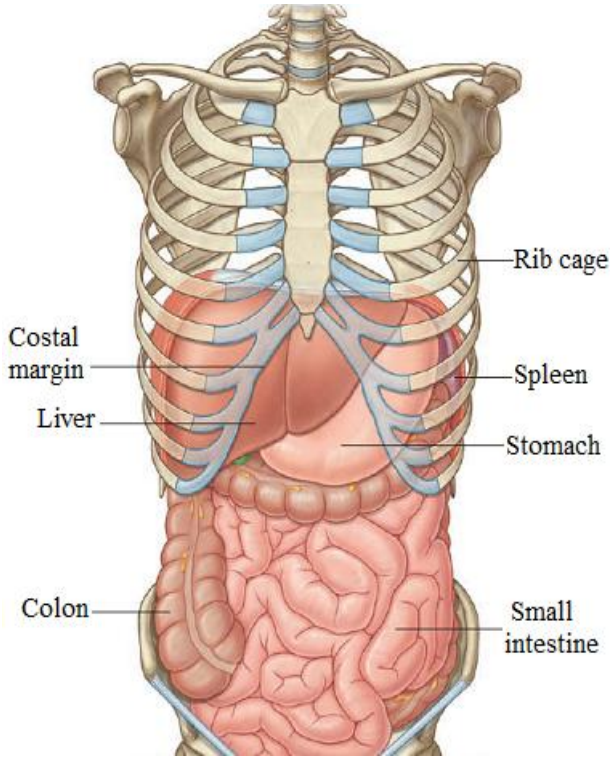

Figure 2.2. The abdomen contains and protects the abdominal viscera
(Source: Drake 2004)

All organs of the human abdomen are tubular (tube like organs) in nature. The digestive tract contains interdependent and connected organs that include the stomach, the small intestine, the colon and appendix. The gallbladder, liver and the pancreas aid digestion, which are connected to the digestive organs. The other organs that are the spleen, kidneys and adrenal glands are connected via blood vessels such as the aorta and inferior vena cava. The pelvic organs, which are the urinary bladder, ovaries, fallopian tubes and uterus, are covered by the same elastic peritoneum membrane, which covers most of the human organs.

2.1.1. Liver

The liver that is a reddish brown organ and positioned in the right upper quadrant of the human abdomen is one of the largest organs of the body, which has a weight of about 2% or 3% to the total body weight (Skandalakis et al. 2004).

The liver is an unshaped organ since its shape is mainly determined by the surrounding structures such as the lower ribs and the diaphragm. The liver can be small and only located in the right half part of the abdomen or extend all to the left and cover the spleen. Figure 2.3 includes three orthogonal slices to show an example size, shape and location of the liver.

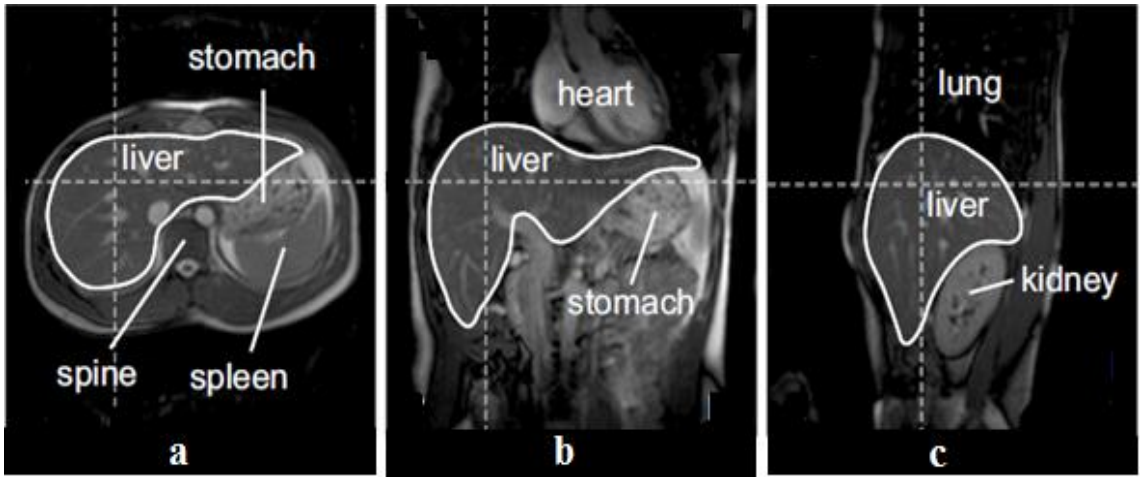

Figure 2.3. Orthogonal slices showing the liver and its position in the upper abdominal image. Transversal (axial) slice (a); Coronol slice (b); Sagital slice (c) (Source: Siebenthal 2008)

The liver has lobes that are connected with blood vessels. The portal vein and the hepatic veins are the largest vessels in the liver, which are illustrated in Figure 2.4. The portal vein brings venous blood from the spleen, the pancreas, and the intestines. The three hepatic veins drain into the Inferior Vena Cava (IVC).

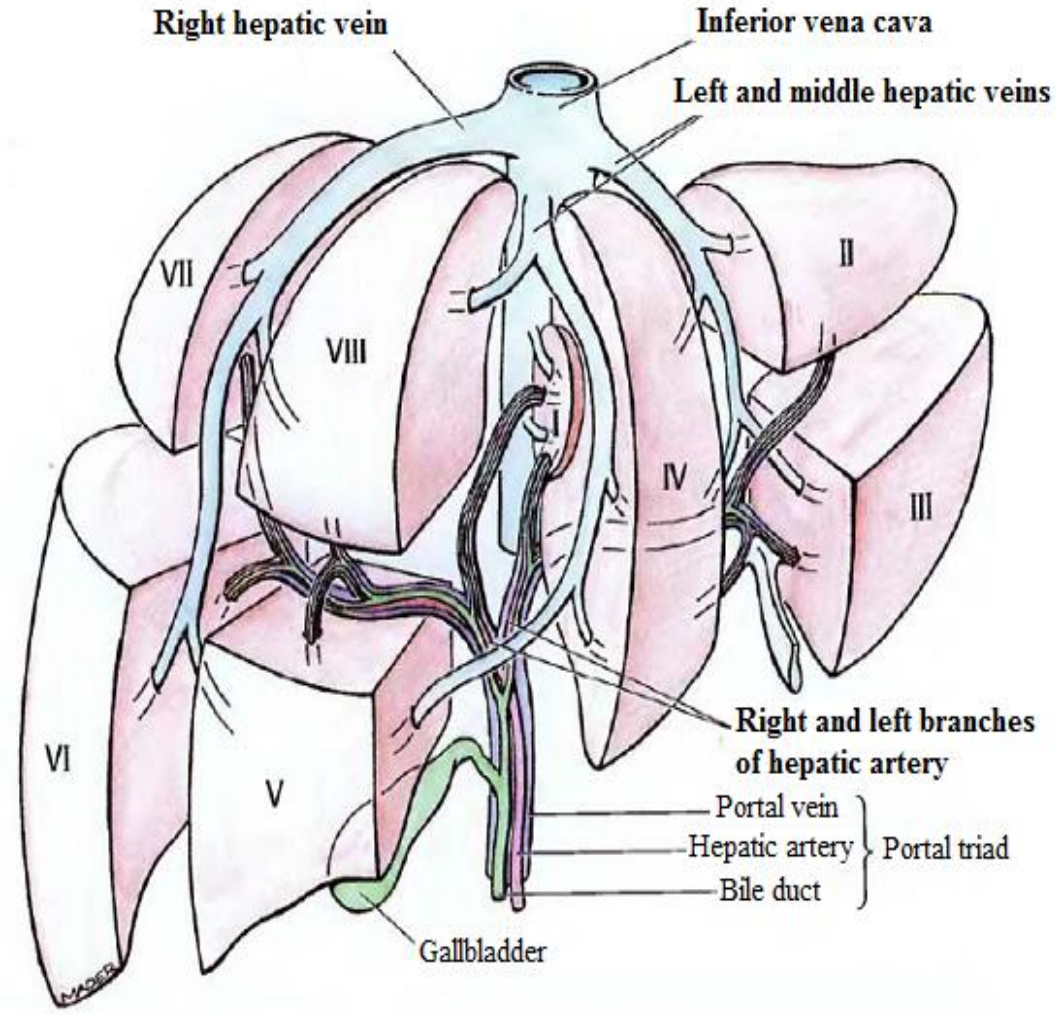

Figure 2.4. Subdivision of the liver into the eight Couinaud segments by the portal vein and the hepatic veins (Source: Moore and Dalley 1999)

There are several schemes for the anatomical subdivision of the liver. A good comprehensive review about the subdivision is in (Rutkauskas et al. 2006). The most widely known liver segmentation scheme is shown in Figure 2.4, which was introduced by Couinaud (Couinaud 1999). It has eight segments obtained according to the planes spanned by the hepatic and the portal veins.

The liver organ is necessary for vital functions. Currently, there is not any technique or device to use in order to compensate the absence of this organ. The liver has many important functions such as protein synthesis and detoxification. It regulates biochemical reactions that include the synthesis or breakdown of complex and small

molecules. Also, it produces bile, which is an alkaline compound aids in digestion, by the emulsification of lipids.

2.1.2. Kidneys

The left and right kidneys are located at the left and right side of the spine. The right kidney is below the diaphragm and posterior to the liver. The left kidney is at the left below the diaphragm and posterior to the spleen.

Kidneys are important for urinary system and homeostatic functions such as acid-base balance, blood pressure, reabsorption of amino acid and glucose. The kidneys carry blood from the paired renal arteries to the paired renal veins.

Each renal artery is divided into interlober arteries, which supply blood to the accurate arteries through the boundary of the cortex and the medulla.

2.1.3. Stomach

The human stomach is a pear-shaped bag, elastic and muscular organ that is positioned on the left upper region of the abdomen.

The stomach is a distensible organ, which churns flood after chewing (mastication) phase. Normally, the stomach expands to hold approximately one liter of food. The size and shape of the stomach change according to the amount of the food inside and the position of the body. Gastric juices are used to break down the food when the food enters to the stomach from the esophagus. The stomach wall is similar to other regions of the digestive tube. However, there exists an extra oblique layer inside the circular layer.

2.1.4. Spleen

The spleen is positioned in the left upper quadrant of the abdomen. It is about 11 centimeters in length and generally weighs 150 grams in healthy adult humans.

The spleen helps our body fight germs and infections. Also, it filters some foreign substances from the blood, disintegrates old cells in blood and produces lymphocytes in addition to serves to store blood.

2.1.5. Gallbladder

The gallbladder is a small and pear-shaped organ in the gallbladder fossa, which is about 4 cm in diameter and 8 cm in length if it fully distended. It is a vascularized alveolar artery.

The gallbladder aids mainly in fat digestion. Also, it concentrates bile that is produced by the liver. It seems darker than the liver due to the high content of bile. The bile, which is a digestive liquid, neutralizes acids in partly digested food. Concentration of the bile increases when it left the liver after it is stored.

2.1.6. Pancreas

The pancreas is located behind the stomach and in front of the spine. The pancreas produces juices to help break down food. Also produces different hormones such as insulin, somatostatin and glucagon, to help control blood sugar levels.

2.1.7. Heart

The heart is a cone-shaped organ located between the lungs and superior to the diaphragm in the chest cavity just posterior to the breastbone. It has approximately the size of a clenched fist.

The heart supplies blood and oxygen to all regions of the body. The heart has four chambers, two superior atria and two inferior ventricles in the human body. The atria, which are upper two chambers of the heart, receive bloods and the ventricles, which are lower two chambers of the heart, discharge bloods. The blood pathway through the heart consists of a pulmonary circuit (Web1) and a systemic circuit.

2.2. Abdominal Imaging

Abdominal imaging that provides diagnostic imaging and intervention of abdominal and pelvic disorders is an important specialty in diagnostic radiology. Interactions with surgical and medical subspecialties, extensive clinical experience for optimal patient care are provided by this specialty of the diagnostic radiology. Digital

image processing methods are used to extract more detailed information or to obtain measurements that are useful for planning treatments or surgeries.

Many different medical imaging modalities are used for the human abdomen (Bidaut 2000). Different properties of the body are used to acquire data. Also, different methods are used for image reconstruction. CT records X-ray attenuation to obtain information about the density of tissues. Excitation and relaxation mechanisms of the proton density are used in MR imaging. MR Spectroscopy (MRS) imaging is based on the contents of the tissues. The varying type of tracers that are injected through a vessel prior to the acquisition is used in Positron Emission Tomography (PET) and Single Photon Emitted Computed Tomography (SPECT) imaging. Also, different information can be acquired using the same modal imaging type through different methods. For example, injection of contrast agents in MR or CT, different tracers in SPECT and PET, dynamic acquisitions, etc.

2.2.1. CT Imaging

CT scanner is mainly used in radiology since it is cheap and has a fast applicability in many clinic situations. X-ray attenuation is measured by CT scanners. The attenuation of X-rays are transmitted by rotation of the X-ray tube around the patient by using detectors positioned on the gantry (Flohr et al. 2005). These measurements and mathematical methods are used to reconstruct 2-D data by using multiple 1-D projections and 2-D cross-sectional images are generated.

Several methods have been developed for CT imaging due to the advancements in technology. Spiral or helical CTs are obtained by rotating the CT tube in one direction around the patient. While the tube is continuously rotated, the table where the patient is lying is moved through the X-ray beam. It is possible to obtain information as a continuous volume with this method (Flohr et al. 2005). The main benefit of this approach is reduced acquisation speed, which allows acquisation of volume data without any mis-registration. Mis-registration is caused by patient movements and breath hold time of the patient. Recently, CT scanners uses the same principles with the spiral scanner. Also the CT scanners contain multiple rows of detector rings that provides multiple slice acquisition possibility at each rotation of the X-ray tube (Flohr et al. 2005).

2.2.2. MR Imaging

MR imaging is widespread used for several clinical purposes as a medical imaging technique and will be used in future more intensively. Interpretation of an MR image contrast resolution is based on how the image was acquired. Image quality optimization and improvement, conspicuity of pathologic findings with reduced error can be provided by understanding the fundamental principles of MRI. Therefore, the methods used to obtain the image are extremely important and should be well understood. However, by nature MRI, which is based on observation of the resonance phenomenon through electromagnetic detection at the resonance frequency, is considered a complex modality by many radiologists and clinicians. There are many degrees of freedom in acquisition parameters for MRI when we compare with other imaging techniques. The main difficulty to understand MRI and its different modalities are due to its technique that involves physics, digital signal processing, electronics and mathematics areas. There are several articles on the principles of MRI (Gibby 2005, McGowan 2008, Nacher 2008) in the literature.

2.2.2.1. Nuclear Magnetic Resonance

Physicists found that orientation of the proton spin is resonated for a certain magnetic field strengths and they discovered Nuclear Magnetic Resonance (NMR) in 1946. Strengths of different magnetic fields resonate different materials. Usage of the magnetic resonance in NMR spectroscopy is discovered by chemists, who studied chemical and physical properties of matters by using the NMR (Hornak 2012).

Nuclei of atoms have magnetic properties. The NMR phenomenon is based on the magnetic properties of nuclei atoms. Hydrogen protons (^{1}H) are the most abundant nuclei in living organisms and they have the best MRI sensitivity so the most frequently studied nuclei.

Protons, neutrons and electrons, the nucleus of an atom rotates about an axis, like the earth itself, and the rotation is known as spin. Paired spins cancel each other and so there is no overall spin in the nucleus of some atoms. However, in many atoms, nucleus possesses a spin. Rules to determine the spin of a given nucleus are that there is no spin in the nucleus when both the number of protons and neutrons are even. There is

a half-integer spin in the nucleus when both the number of protons and neutrons are odd such as 1/2 or 3/2. There is an integer spin when both the number of neutrons and protons are odd such as 1, 2, 3.

Action of protons, which are spinning their axes and positively charged, is similar to randomly oriented tiny magnets so that their magnetic fields cancel out. A kinetic momentum J is possessed by each nucleus. The momentum is related to its current, which is created by a spinning particle and can be quantified as $I = q \times v / 2\pi r$ with q the charge on the particle, r the radius of the particle, and v the tangential velocity of a point on the surface of the particle.

Spins tend to align with an external magnetic field (called B_0) and there are two preferred alignments as up and down relative to the direction of the applied field. A large number of proton spins will be aligned parallel to B_0, producing a net magnetization which are the source of the MR signal and is used to produce MRI, with a somewhat smaller number of proton spins will be oriented antiparallel. A slight energy difference exists between the two orientations, and thus a system of many spins can be characterized by its energy state. A stronger field will develop stronger polarization between the two states.

The force of the magnetic field interacts with the protons when these protons are spinning and enter in a strong magnetic field. The force of the magnetic field causes precession motion of the protons.

2.2.2.2. The Effect of Radiofrequency

Spinning protons in a magnetic field can be excited by the application of Radio Frequency (RF) energy. The RF energy is transmitted by using RF transmit coils such as head coil or knee coil in an MR scanner. The RF is transmitted in a short period of time that is called an RF pulse. The resonance effect is available only when the precessional proton frequency is equal to the transmitted RF pulse and so the energy is transferred to the protons efficiently.

The net magnetization rotates away from the *z*-direction, which is known as longitudinal magnetization, to *x*-*y* direction, which is known as transverse magnetization, when energy is absorbed by the RF pulse.

The corresponding axis for rotating coordinate axis (x, y, z) is defined as (x', y', z) since the turning is around the z-direction.

2.2.2.3. Relaxation and Free Induction Decay

We move the protons into a higher energy state when we rotate the net magnetization 90º into the x-y plane because the protons absorb energy from the RF pulse. But they want to align with the main magnetic field which means they prefer to be in a low energy state and they do so by releasing the absorbed energy in the shape of warmth and RF waves. The net magnetization rotates back to align itself with the z-direction.

After relaxation, the nuclei return to their equilibrium positions, which is fully align with z-direction, of the magnetization when the pulse stops, and the signal decays. Frequencies from all the target nuclei are in this exponentially decaying signal. It is picked up by the detection coil as an oscillating voltage which is generated using the magnetic moments by precessing or relaxing back to equilibrium. The signal can not be recorded since the frequency is very high. Therefore, at first, an interferogram of low frequency is produced by mixing the signal with a lower frequency signal. Then, the Free Induction Decay (FID) is obtained by digitizing the interferogram. A frequency domain spectrum is obtained by applying Fourier Transformation (FT) to the FID. The relaxation process can be divided into two parts: T1 (longitudinal) relaxation and T2 (transverse) relaxation.

Longitudinal magnetization becomes zero when RF pulse is applied. After the RF excitation pulse stops, the longitudinal magnetization will begin to re-grow along the z-axis, while emitting a radio-frequency wave. This is called as T1 or longitudinal relaxation since it describes what happens in the z-direction and also called as spin-lattice relaxation since the energy is released to the surrounding tissue (or lattice). The rate at which protons release their energy (relaxation) is different for each tissue therefore MRI has good contrast resolution. Tightly bound protons will release their energy much quicker to their surroundings than protons, which are bound loosely. For example, one ^{1}H atom may be bound very tight, such as in fat tissue, while the other has a much looser bond, such as in water.

There is not a magnetization at $t = 0$ in z-direction for T1 relaxation. But after the RF pulse stops the longitudinal magnetization starts. T1 is defined as the time constant which takes for the longitudinal magnetization to reach sixty-three percent of the original magnetization, if we assume a 90º RF pulse is applied. If an image is obtained when the relaxation curves are separated for different tissues then T1-weighted contrast will be maximized.

The influence of flip angle on T1 weighted images is shown in Figure 2.5. Contrast between the liver and spleen and the liver and the intra-hepatic vasculature increases with increasing flip angle and is optimum at a flip angle of 85º.

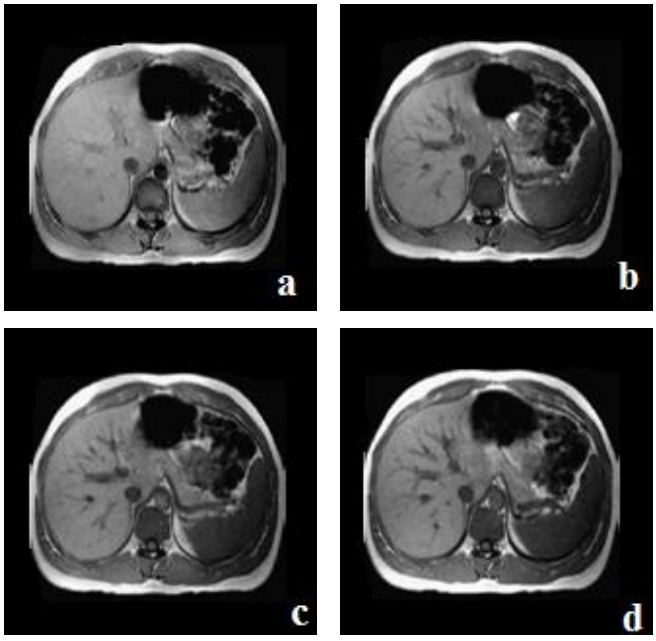

Figure 2.5. T1 image with 25º flip angle (a), with 45º flip angle (b), with 65º flip angle (c), with 85º flip angle (d) (Source: Robinson and Ward 2006).

T1 and T2 relaxation are two independent processes. T1 relaxation describes what happens in the z-direction, while T2 relaxation, which is much faster, describes what happens in the x-y plane. Transverse magnetization will be maximized and the longitudinal magnetization will be zero after application of a 90° RF pulse. The protons begin their precession with the same phase that means protons become in-phase during the RF pulse. When the pulse stops then the protons are in-phase for a time but begin to de-phase since as we know that each proton can be thought of as a tiny bar magnet with a north and a south pole and two poles of the same sign repel each other. The situation will occur that one vector is slowed down while the other vector might speed up

because the magnetic fields of each vector are influenced by one another. The vectors will rotate at different speeds and therefore they are not able to point into the same direction anymore so they will start to de-phase. The de-phasing can be caused by magnetic field inhomogeneities, chemical shift effects or spin to spin interactions. The signals from these de-phasing protons begin to cancel out and so the MR signal decreases. T2 characterizes the rate of de-phasing for the protons associated with that tissue. The process of getting from an in-phase situation to an out-of-phase situation is called as T2 relaxation, if the de-phasing effect is only due to the spin to spin interaction.

T2 relaxation is a time constant that all spins are in-phase at $t = 0$ but immediately start to de-phase. T2 is defined as the time which takes for the spins to de-phase to 37% of the original value. The de-phasing rate is different for each tissue, for example fat tissue will de-phase quickly but water will de-phase slower. Although the gyromagnetic ratio is a constant, there is no homogeneity in the magnetic field across the imaging volume due to hardware limitations so different magnetic field strengths will do precession at different Larmor frequencies. If an image is obtained when the relaxation curves are widely separated then T2-weighted contrast will be maximized.

The time constant for FID signal is received in absence of any magnetic field should be T2 relaxation time, but the signal decays very fast so the constant is a T2* relaxation time instead of T2. T2* relaxation means the de-phasing is caused by not only spin to spin interaction. The fast decay effect is due to the de-phasing of the proton magnetic moments in the transverse plane just after the 90° RF pulse. The de-phasing is explained by the spatial in-homogeneities of the B_0 field, which leads several precession of the frequency among magnetic moments.

2.2.2.4. Inversion Recovery Imaging

An NMR spectrum can be recorded by using an inversion recovery pulse sequence. First, a 180^o pulse is applied in this sequence. This causes rotation of the net magnetization down to the -z axis. The magnetization returns toward the equilibrium position of it along the +z axis after spin-lattice relaxation. After delivery of the 180° RF pulse, there is not any signal since there is not any vector component of the

magnetization in the transverse plane. Instead, the inverted longitudinal magnetization vector moves through the transverse plane to return to its original orientation. The 90° RF pulse of the SE sequence is applied, which rotates the longitudinal magnetization into the *xy* plane, after some relaxation has occurred. The time between the 180° RF and the 90° RF pulse is the inversion time, TI. The 90^{o} RF pulse is applied in this example after application of the 180^{o} RF pulse. The magnetization rotates about the *z* axis once it is present in the *xy* plane. Then it dephases giving a FID. Therefore, the RF pulses of an inversion recovery sequence, which uses a spin-echo sequence to detect the magnetization, are 180-90-180.

The inversion time, TI, can be changed to manipulate image contrast. With a short inversion time and delivery of the 90° RF excitation pulse sequence after the 180° RF inversion pulse, all the negative longitudinal magnetization is flipped into the transverse plane. To generate a weaker signal, less longitudinal magnetization is tilted into the transverse plane with a longer interval. However, if the inversion time is long enough, which is able to allow full relaxation, then the signal becomes stronger again.

The advantage of the inversion recovery sequence is very strong contrastness between tissues since it has different T1 relaxation times and it can suppress different tissues such as fat or fluid. However, the main disadvantage is less efficient in time than other RF pulse sequences due to the additional inversion pulse.

SPIR provides images without fat signals. SPIR is an inversion technique for fat suppression. The method consists of a standard imaging sequence preceded by a spectrally-selective inversion pulse, in which the precession frequency approach fat rather than water proton, eliminate the fat signal. SPIR technique employs an initial inverting pulse that is made frequency selective and only inverts fat magnetization. Note that SPIR is not a pulse sequence but merely an additional module that can be applied prior to other pulse sequences.

2.2.2.5. Principles of MR Imaging and Hardware

A general structure of MRI hardware is shown in Figure 2.6.

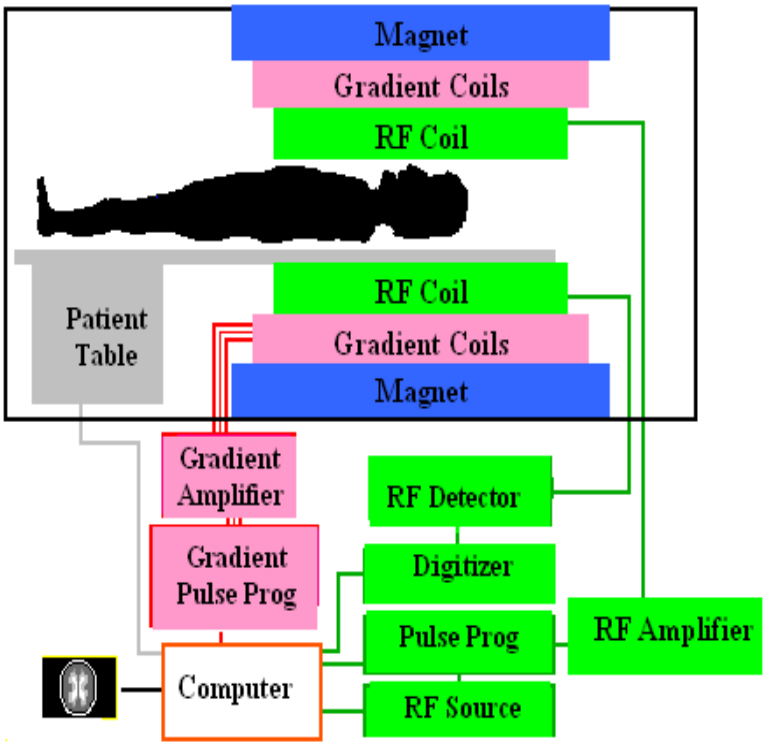

Figure 2.6. MRI Hardware

(Source: Hornak 2012)

The gradient coils are a set of wires in the magnet, which are used to create additional magnetic fields, superimposed on the main magnetic field B_0. We assume that a human head contains only two small distinct regions, where there is spin density. If each of the regions of spin is to experience a unique magnetic field then it will be possible to image their positions. This is accomplished by a gradient in the magnetic field. A variation in the magnetic field according to position is called as a magnetic field gradient. If a variation is with respect to one direction then it is a one-dimensional magnetic field gradient. If a variation is with respect to two directions then it is a two-dimensional gradient. A one-dimensional linear magnetic field gradient is the most useful gradient type in MRI. This magnetic field gradient in the x direction, in a magnetic field (B_0), indicates that the magnetic field is increasing along the x-axis. Therefore, if a gradient is applied along the x-direction then the precession frequency of the protons will be dependent on their position during the x-direction, which is used to distinguish protons with different x coordinates. The symbols for a magnetic field gradient in the x, y, and z axis can be identified as G_x, G_y, and G_z. The frequency encoding is performed by application of the G_x gradient of the signal (Katscher and Börnert 2007).

The spins shed their excess energy, which are acquired from the 90º Radio Frequency (RF) pulse, in the shape of radio frequency waves during the relaxation processes. An image is produced by picking up these waves before they disappear into space. This can be done with a receive coil or a transmit coil.

Slice selection in an MRI dataset corresponds to the selection of spins in a plane through the object. A slice selection is performed by using a magnetic field gradient (G_z) along the *z*-axis as,

$$B_0 = B_{0m} + G_z.z \tag{2.1}$$

Protons, which belong to a slice perpendicular to the *z*-direction, can be selected to excite by an excitation pulse after selection of the exact frequency that corresponds to the Larmor frequency of the slice protons. The spatial width value of the slice, which depends on the frequency distribution and also the frequency width of the excitation, is obtained by the FT. A sinc pulse in the time domain will provide a rectangular shape in the frequency domain so a rectangular slice is obtained with an infinite sinc pulse.

2.2.3. Ultrasound (Sonography)

Ultrasound imaging, which is known as sonography or ultrasound scanning, involves exposing region of the human body to high frequency sound waves in order to look at organs and to produce images of the organs. The frequency of the sound pressure is approximately greater than 20 kHz. Unlike X-ray examinations, ionizing radiation is not used in ultrasounds since they are captured in real-time and can show the structure of organs in the body. Movement of the organs and blood flowing through blood vessels can also be shown. Physicians can diagnose and treat several medical conditions by using ultrasounds, which are non-invasive medical tests. Ultrasound is relatively cheaper and portable than CT and MR.

2.3. The Role of MRI in Liver Imaging

The development and widespread use of MRI for liver disease has been relatively slow when we compare MR applications in the central nervous system and musculoskeletal. One important reason is that the liver requires a large field of view because of its large size so the available spatial resolution is less than the smaller fields

which are used for brain and joint imaging. Also, there is a more significant difficulty in the development of liver MRI that is motion artifact. Although it is possible to overcome this major handicap now by using breath-hold sequences, cardiac gating, respiratory and other motion suppression techniques, to obtain high quality in image acquisition needs an unflagging attention to details of techniques. The most important reason of the slow incorporation of MRI for liver imaging can be identified as the relatively available high level of accuracy with sonography and computed tomography (CT) that are both less costly and more widely available (Hagspiel et al.1995, Huppertz et al.2005, Lencioni et al.2005, Ward et al.2003).

Contrast and temporal resolution are the important differences between sonography, CT and MRI. It is possible to visualize a rapid physiological change which means flow in blood vessels and tissue perfusion in the liver by improved temporal resolution. The main advantages of MRI over sonography and CT are based on its better contrast resolution due to several factors. One of them is that, MRI can demonstrate several different tissue characteristics, so that acquisition sequences can be chosen to enhance or isolate the features, which are most likely to discriminate individual pathologies. However, sonography represents tissue interfaces and CT records X-ray attenuation. Another factor for the advantage of MRI is that conventional MRI gadolinium agents are similar to contrast agents, which are used in CT and sonography and have an extracellular or intravascular distribution. However, intracellular contrast agents are also used in MRI gadolinium agents. Also, the uniqueness of MRI in offering the possibility of modifying the signal characteristics of tissue in vivo, for example by frequency-selective fat suppression or water excitation techniques, can be identified as an another major reason for its superior contrast resolution than others (Hawighorst et al.1999, Ward and Robinson 2001, Burrel 2003, Kwak et al.2004).

Quality of liver MRI has been improved by technical developments such as gradients that are more powerful, more sensitive receiver coils, fundamental changes in pulse sequence design and faster switching properties of gradient amplifiers, which allow acquisition of high-resolution images of the entire liver volume within a single breath-hold. The improved temporal resolution allows a more detailed analysis of perfusion characteristics by using conventional extracellular fluid contrast agents. Also the correlation between abnormal anatomy and abnormal physiology in the liver parenchyma can be obtained by the creation of new tissue-specific contrast media (Ward et al.2003, Semelka et al.1999, Seneterre et al.1996, Ichikawa 2004).

Although obtaining a good image requires consideration of the clinical question for each patient, choosing appropriate techniques, contrast agents and meticulous attention to detail in the acquisition and interpretation of the images, it is identified in the literature that liver MRI are more sensitive than multi-slice CT to detect small metastases, especially from colorectal cancer (Hagspiel et al.1995, Huppertz et al.2005, Lencioni et al.2005, Ward et al.2003, Semelka et al.1999, Seneterre et al.1996, Kondo et al.2000, Muller et al.1999, Poeckler et al.1999, Ward et al.2005) and more specific to characterize various benign pathologies presenting as focal abnormalities in the liver (Poeckler et al.1999, Ward et al.2005, Ward and Robinson 2001, Hawighorst et al.1999). Also liver MRI is the most effective technique to detect and characterize hepatocellular cancer early in cirrhotic patients (Burrel et al.2003, Kwak et al.2004, Ichikawa 2004).

2.4. Image Processing Methods

Image processing methods are applied for different reasons. For example, medical image processing is generally used to obtain detailed information or an important information from images for surgeries, planning treatments or other clinical operations.

There are several image processing methods (Gonzalez and Woods 1992). However, only some of them that have been used in this thesis project are explained in this section.

2.4.1 Filtering

Filtering operations can be performed in the spatial domain with pixel values or in the frequency domain with frequency spectrum after the application of 2D FT (Gonzalez and Woods 1992). Convolution operation is performed by using a filter mask (i.e. a kernel) and an image. The filtered image is obtained by combining the kernel with each pixel block, which has equal size with the kernel. The kernel size is important since it gives the size information that will be used for each effect. The chosen kernel size is generally an odd number such as 3x3 or 5x5 since there is a central pixel, which is the only pixel that changes its value during the convolution process, in the center of the block. The filter function and the frequency spectrum of the image is obtained by FT

is multiplied for frequency domain filtering. The filtered image is produced in spatial domain by taking the inverse FT of the result spectrum.

2.4.1.1. Low-pass Filtering

High frequency components like noise are removed by applying a low-pass filtering. Details or edges are eliminated according to the chosen low-pass fitler type. Therefore, low-pass filters can be used to enhance homogeneous parts or to preserve large structures in an image. Homogeneous parts are generally inner sides of tissues or parenchyma of organs in human abdominal images.

Low-pass filters cause blurring due to unclear borders (edges) when we apply hem to remove noise from images. Anisotropic diffusion is a solution to reduce noise without removing details or edges from images. If the diffusion coefficients are selected as constant values then the anisotropic diffusion is the same with Gaussian blurring. If the diffusion coefficients are selected as an edge seeking function then the obtained equation performs the diffusion in homogeneous regions and prohibit the diffusion across strong edges. Therefore, edges are preserved while noise are removing (Perona and Malik 1987).

2.4.1.2. High-pass Filtering

Details in an image can be extracted or enhanced by using high-pass filtering since edges need high frequencies (Gonzalez and Woods 1992). However, enhancing detail information may cause noise. Therefore, high-pass fitler parameters are selected according to applications carefully.

Laplacian filters, Laplacian of Gaussian (LoG) filters such as Mexican hat and Gradient filters such as Sobel, Prewitt can be used as a high-pass fitler. Laplacian filters are based on second order derivatives over neighborhoods of the pixel and gives null values for minimum and maximum of gradients. They are sensitive to noise. High frequency components can be enhanced and the noise sensitivity can be decreased by adding the original image to the result of the fitler. LoG filtering is performed by smoothing the image with a Gaussian filter and then enhancing edges with a Laplacian

fitler. Gradient filters are first order derivatives and gives a vector in spatial domain where the largest changes correspond to the largest values.

2.4.1.3. Morphological Filtering

Morphological filtering can be performed only in the spatial domain since shapes of the objects in an image is used with a structuring element of the filter. It is not possible to represent shape information in frequency domain. Morphological filtering is a convolution process by using the original image and the kernel that is obtained by defining the shape of the structuring element as a kernel.

This is a binary image processing and there are four morphological operations that are erosion, dilation, opening and closing. Erosion filter shrinks objects and open gaps (holes) in images. Dilation filter expands objects and close gaps (holes). Opening is the combined filter that is obtained by combining erosion followed by dilation filter. Closing filter is similar to opening filter but it is obtained by combining dilation filtering followed by erosion.

2.4.2. Image Segmentation

Segmentation is performed to partition an image into multiple parts. The aim of this process is to simplify or/and change the representation of the digital image into something that is easier to analyze and more meaningful. Some examples for biomedical image segmentation applications can be given as examination of anatomical structure, computer-guided surgery, planning of treatment, diagnosis, measurement of tissue volumes to locate tumors and other pathologies.

Manual segmentation is error prone, very time consuming because of the high number of slices and tedious. It is performed by an expert using a device that is generally a mouse and a software program for labeling edge pixels. Therefore, it depends on the skills and experience of the expert that means manual segmentation method is a subjective process and not reproducible. Therefore, computer-aided medical image analysis is indispensible.

There is not any general solution for image segmentation problems. Therefore, many different fully automatic and semi-automatic image segmentation techniques have been proposed for different images.

In practice, segmentation algorithms usually require knowledge and experience of radiologists to adjust segmentation parameters to get optimal performance. Mostly computerized systems run in an interactive or semi-automatic manner because of the complexity of medical image segmentation (Levinski et al.2009), which means that the radiologists initiate the segmentation, interrupt it when necessary, and finally stop the algorithm. Generally, initial information such as an initial seed point or an initial boundary is inserted to the process for initialization by the radiologists in these methods. Active contour and region growing methods are mostly known semi-automatic techniques. In active contour method, a cost function obtained by the initial boundary is minimized. In region growing method, connections of pixels are checked by starting from initial information according to a criterion.

The methods in fully automatic segmentation approaches are applied without any user intervention by using several parameters. However, the values of these parameters can not be identified in a strict bound because of the variations in anatomy and also characteristics of images.

An image segmentation technique can be in the group of semi-automatic or fully automatic segmentation methods according to its implementation way. Segmentation techniques can be categorized as thresholding based, clustering based, atlas based, model based, Artifical Neural Network (ANN) or PDE based approaches.

Thresholding is a simple method that determines an intensity value, which is the threshold value, and then separates pixels, which have upper, between or lower threshold values. However, thresholding is not useful for organ segmentation due to several reasons such as intensity inhomogeneity, noise or adjacent organs with similar intensity.

Clustering method uses an iterative algorithm. Parameters of a cost function of the current partition are computed and then used to minimize this function. K-means (Coleman and Andrews 1979) is the commonly known clustering method. In the K-means method, mean intensities are calculated iteratively for each class and then the image is segmented by classifying pixels into the classes according to the closest mean values (Jain and Dubes 1988). Initial centers and the number of classes are given as prior information to the algorithm.

In atlas based segmentation approaches, an atlas is used as the reference and one-to-one transformation is applied to do a mapping with a pre-segmented atlas image and the image that we want to find the rquired segment (Maintz and Viergever 1998).

Several model based segmentation methods have been proposed. The assumption of the model based approaches is that the structures of organs have a repetitive form of geometry. Therefore, a probabilistic model is searched to explain the variation of the shape of the organ and this model is used as prior for segmentation of the image. This process involves three steps. One of them is registration of the training images to a common pose. Another step is probabilistic representation for variations of the registered example images. The last step is statistical inference by using the model and the image.

ANNs have also been used for image segmentation. ANNs simulate biological learning by applying elementary computations. Learning process is performed by the adaptation of weights that are assigned to the connections between these elements. ANNs can be used both for classification and clustering (Hall et al. 1992). In the case of classification, training data is used to determine the weights of ANN at first. Next, new data is segmented with adjusted weights. Spatial information can be incorporated into its classification procedures by using several interconnections in a neural network. In the case of clustering, ANNs are used in an unsupervised approach as a clustering technique and also for deformable models (Vilarino et al.1998).

PDE based segmentation methods are based on active contours. The central idea for image segmentation using PDE is evolution of an initial contour towards the lowest potential of an identified cost function so that the definition of the cost function reflects the process to be addressed. Curve propagation can be performed by parametric or geometric active contour (i.e. level set) methods.

The most important difficulty in MR image segmentation is the intensity inhomogeneity (Condon et al.1989, Simmons et al.1994). Therefore, the segmentation methods that are based on the intensity values by assuming that intensities in a tissue class are constant over an image are not successfull. The difficulties for organ segmentation from CT images are generally due to the artifacts. The artifacts are caused by low attenuation adjacent to bones or patient motion such as beam-hardening artifacts or streak artifacts (Slone et al. 2000). Ultrasound imaging is usually used for motion estimation instead of image segmentation due to the real-time acquisation. High levels of speckles cause limited segmentation from ultrasound images (Mojsilovic et al.1997).

2.5. K-Means Method

The K-means method (Anderberg 1973) is commonly known as a deterministic approach. It is an unsupervised clustering method, which is used in various applications (Tsagaan et al 2001, Fahim et al 2006, Yijun and Guirong 2009, AbdulNazeer and Sebastian 2009, Juang and Wu 2010, Yang et al 2010). K-means minimizes the sum of distances from each data item that measures the distance value from each data item to its cluster center. Computation of cluster centers is performed for each cluster after assigning all data items to their closest centers repeatedly. Mainly known distances are squared Euclidean distance, Hamming distance and cosine dissimilarity. Generally, squared Euclidean distance is used as the required distance measure for K-means algorithm. The sum of squared error function is used as the criterion function to be optimized in a Euclidean K-means method (Duda and Hart 1973). Therefore, the goal of this method is to minimize the summation:

$$J = \sum_{j=1}^{k} \sum_{i=1}^{n} \left\| x_i^{(j)} - c_j \right\|^2 \tag{2.2}$$

Here, the distance between the cluster center c_j and a gray level value $x_i^{(j)}$ is given with $\left\| x_i^{(j)} - c_j \right\|^2$ for *n* data points. Cluster centers are recalculated at each iteration.

2.6. Artifical Neural Networks

Artificial Neural Network (ANN), which is mostly known neural network, is inspired by functional properties and also structural aspects of biological neural networks. It is a computational or mathematical model. A biological neural network is composed of groups of biologically connected neurons, each of which are connected to many other neurons. These connections are called synapses and they are formed from axons to dendrites. ANNs have been applied to several areas such as speech recognition, pattern classification, clustering and adaptive control. In case of classification, the weights of ANN are determined by using training datasets, and then adjusted weight values are used to segment new data. Spatial information can be integrated into its classification algorithms because of the several interconnections that are used in a neural network.

2.6.1. Learning (Haykin 1999)

The possibility of learning has attracted main interest in ANNs. The learning process for ANN can be defined as adjustment of the free parameters of an ANN based on some measure and the main aim is to improve the performance of ANN for a better fitting to its field of application. These are supervised learning and unsupervised learning.

A set of example pairs, in other words training data, are used to adjust the values of free parameters of the network in supervised learning, which is also known as learning with a teacher. This adjustment is carried out iteratively and done both under the influence of the training data and an error signal which is defined as the difference between the desired response and the actual response of the network. The network performance can be evaluated with unseen data after this adjustment process (i.e. training process). In unsupervised learning, there is not any labeled example of the function to be learned by the function, the idea is to minimize a chosen cost function, which is any function of the input data, by adjusting free parameters.

Single layer and MLPs are used for supervised learning. When we recursively apply these approaches then they are known as stochastic approximation.

There are several training algorithms for neural networks such as expectation maximization, evolutionary computation methods, statistical estimation methods (i.e. back propagation by gradient descent) and non-parametric methods.

2.6.2. Single Layer Perceptrons

The perceptron, which is built using a single neuron (node) with adjustable synaptic weights and also bias, is limited for classification with only two hypotheses and is the simplest form of ANN. The classification can be formed by expanding the output layer of the perceptron to include more than one neuron. If the data is linearly separable then the perceptron algorithm converges after several iterations that means the perceptron works properly (Rosenblatt 1958). The learning process is a supervised learning that is achieved by backpropagation process and a generalization form of the least mean squares method in the linear perceptron. For learning in the perceptron, each data is processed, the connection weights are updated and the expected result is compared to the amount of error in the output (Haykin 1999).

2.6.3. MLP

A MLP is a modification form of the linear perceptron algorithm, which uses three or more layers of nodes with nonlinear activation functions. MLP is more powerful than the perceptron method since it can distinguish non-linearly separated data. A MLP consists of a set of source nodes that constitute an input layer, an output layer and hidden layers that can be one or more. The input signal propagates through the multilayer perceptrons that are a generalization network of the single layer perceptrons. The training of MLPs is performed by using the error back-propagation algorithm (generally known as back-propagation) that depends on the error correction learning rule. The back propagation algorithm has two main passes: One of them is a forward pass with fixed synaptic weights. This pass consists of application of an input vector to the sensory nodes and propagation of its effect through the network. The other one is a backward pass where the synaptic weights are adjusted according to an error-correction rule. The error signal is produced by subtracting the actual response of the network from a desired response. The backward propagated signal through the network is this error signal (Haykin 1999).

2.7. GMM

Finite mixture models (McLachlan and Peel 2000) are used for clustering. GMMs are generally used as a powerful probabilistic model based clustering (Jain et al. 2000, Titterington et al.1985, Fraley and Raftery 2002, McLachlan and Basford 1988). The GMM is an unsupervised classifier since the underlying probability density functions of the observed datasets are estimated during the training of the classifier. It is called as unsupervised classifier because the training samples of the classifier are not labeled in order to show their categories. The application of this model for pixel labeling is based on the assumption that the gray level value of each pixel in the observed image is a sample from a finite mixture distribution.

The probability density function in GMM can be defined as a weighted sum of Gaussians. If we denote the voxel intensity vectors, which are the feature vectors, for N voxels as x_i (i=1, 2, ……, N) then the probability distribution of the kth class can be represented as $p_k\left(x|\Theta_k\right)$, which depends on Θ_k parameters. This distribution can be

modeled by a Gaussian distribution with mean vector μ_k and covariance matrix $\sum_k$. Then,

$$p_k(x \mid \Theta_k) = p_k(x \mid \mu_k, \sum_k) = \frac{1}{\sqrt{\det(2\pi \sum_k)}} e^{-(x-\mu_k)T \sum_k^{-1}(x-\mu_k)/2} \tag{2.3}$$

In the GMM, the assumption is that the features are independent, identically distributed and also the number of classes is known. Therefore, if we know the mean, covariance and prior probability values then it is possible to define a multivariate Gaussian probability density function. Because, the probability distribution of each voxel can be represented as a mixture of probability distributions with α_k coefficients, which can be taken as prior probabilities, we can write that;

$$p(x \mid \Theta) = \sum_{k=1}^{K} \alpha_k p_k(x \mid \Theta_k) \tag{2.4}$$

Then the probability for each class can be represented by Bayes rule as;

$$p(k \mid x_i, \Theta^t) = \frac{\alpha_k^t p_k(x_i \mid \Theta_k^t)}{p(x_i \mid \Theta^t)} = \frac{\alpha_k^t p_k(x_i \mid \Theta_k^t)}{\sum_{j=1}^{K} \alpha_j^t p_j(x_i \mid \Theta_j^t)} \tag{2.5}$$

The conditional probability densities for each class are a sum of multivariate Gaussian probability density functions.

2.7.1. GMM vs. K-means

The GMM based segmentation with EM algorithm has an advantage over other methods since the correlation of gray values can be potentially accounted by the covariance structure. Therefore, the probabilistic technique is more flexible than K-means that is a heuristic method, which uses distance values of gray levels and lacks of a statistical foundation. In other words, the GMMs are soft than K-means since each data item has either 0% or 100% membership to its closest cluster in K-means. However, in GMM, each data x_n belongs to cluster Θ_k with $p(\Theta_k \mid x_n)$ and each data contributes to some extent. K-means is a limited version of GMM with equal weight and equal spherical covariance, $\sum_k = \sigma^2 I$. K-means algorithm can not adapt to any cluster shape.

Its cluster modeling capability is limited to spherical clusters with similar number of data points. In the GMM, each mixture component is viewed as clusters of arbitrary ellipsoidal shapes. Therefore, the decision in K-means clustering algorithm is hard due to the assigning each data item to a single cluster. The decision in GMM clustering algorithm is soft due to having a posterior probability for each data item, which presents that each data item has a probability to belong to each cluster. However, the drawback of EM algorithm is the sensitivity of it to the chosen initial values. The result of GMM method depends on the number of chosen components. We have chosen a constant kernel number in the implementation for the abdominal organ segmentation from SPIR datasets. The parameter values of the GMM are recalculated iteratively by starting from initial parameters until convergence. Accuracy of the GMM based segmentation technique depends on similarity between the probabilistic model and image intensity distributions.

2.7.2 Parameter Estimation Using EM Algorithm

The problem of parameter estimation in an incomplete dataset is regarded as an incomplete data problem because both class labels and the parameters are unknown and also they are interdependent.

The estimation of the GMM parameters, which are $(\mu_k, \sum_k)$ and the prior probability of having a Gaussian for each class, is commonly calculated by using Maximum Likelihood Estimation (MLE). However, finding the probability distribution parameters for N data points with MLE by the formula (2.7) sometimes gives useless singular estimates if all parameters are unknown (Duda and Hart 1973, Everitt and Hand 1981) and this expression is a nonlinear function of parameters Θ so direct maximization is not possible.

$$l(X \mid \Theta) = \log p(X \mid \Theta) = \log \prod_{i=1}^{N} p(x_i \mid \Theta) = \sum_{i=1}^{N} \log(\sum_{k=1}^{K} \alpha_k p_k(x_i \mid \Theta_k)) \tag{2.6}$$

$$\Theta_{ML}^{*} = \arg\max_{\Theta} l(X \mid \Theta) \tag{2.7}$$

The equation in (2.6) contains the log of sum so finding parameters is a difficult task because of the summation in the mixture of Gaussian equation that can't take the log of a sum. This case is also true for the maximum a posteriori (MAP) estimation

$$\Theta^*_{MAP} = \arg\max_{\Theta}(l(X \mid \Theta) + \log p(\Theta)) \tag{2.8}$$

where $p(\Theta)$ is the prior. However, if we know which data contribute to which Gaussian component, then the problem can be a lot easier since we can rewrite the equation so that the summation goes away. Therefore, an ideal approach for this estimation is to use EM algorithm (McLachlan and Peel 2000, Dempster et al. 1977, Leemput et al. 1999). The EM method finds the local maximum of the log-likelihood by considering X as an incomplete data. For Gaussian mixtures, the missing variables are a set of *N* labels $Z = \{z^1, ...z^N\}$ associated to the samples. Each label is a binary vector $z^i = [z_1^{(n)}, ...z_K^{(n)}]$ where *K* is the number of components, $z_p^{(n)} = 0$ and $z_m^{(n)} = 1$ for $p \neq m$ means that sample x_n has been produced by the *m*th kernel. If the complete set of data $Y = \{X, Z\}$ then the log-likelihood of this set is given as;

$$\log p(X, Z \mid \Theta) = \sum_{n=1}^{N}\sum_{k=1}^{K} z_k^n \log[\alpha_k p(x_{\ n} \mid \Theta_k)] \tag{2.9}$$

A sequence of estimates, $\{\Theta^*(t), t = 1, 2....\}$, is produced using expectation and maximization steps until a converge criterion is met.

- **E-Step:** Estimates the expected value according to the given visible data *X* and the current parameters of the estimation $\Theta^*(t)$. The expectation $W \equiv E[Z \mid X, \Theta^*(t)]$ can be calculated easily pluging into $\log p(X, Z \mid \Theta)$ which is linear with respect to the hidden Z. This process is represented as a Q-function;

$$Q(\Theta, \Theta^*(t)) \equiv E[\log p(X, Z \mid \Theta) \mid X, \Theta^*(t)] = \log p(X, W \mid \Theta) \tag{2.10}$$

The elements of Z are binary so their conditional expectations can be written as,

$$E[z_k^{(n)} \mid X, \Theta^*(t)] = \Pr[z_k^{(n)} = 1 \mid x_n, \Theta^*(t)] = \frac{\alpha_k^*(t)\, p(x_n \mid \Theta_k^*(t))}{\sum_{j=1}^{K} \alpha_j^*(t)\, p(x_n \mid \Theta_k^*(t))} \tag{2.11}$$

where (2.11) is a posteriori probability and it is possible to write the x_n generation using the kernel *k* is;

$$p(k \mid x_n) = \frac{\alpha_k p(x_n \mid k)}{\sum_{j=1}^{K} \alpha_j p(x_n \mid j)} \tag{2.12}$$

where $p(x_n \mid k)$ and $p(x_n \mid j)$ are the Gaussian densities for kernel k (with Θ_k parameter) and j (with Θ_j parameter)

- **M-Step:** Estimates the new parameters $\Theta^*(t+1)$ for the MAP estimation as;

$$\Theta^*(t+1) = \arg\max_{\Theta}(Q(\Theta, \Theta^*(t)) + \log p(\Theta)) \tag{2.13}$$

or for the ML criterion as;

$$\Theta^*(t+1) = \arg\max_{\Theta} Q(\Theta, \Theta^*(t)) \tag{2.14}$$

Therefore, the main idea of the EM algorithm is to estimate the hidden data using the current estimated values and the given visible data, and use it to form the complete dataset so that new parameters can be estimated by maximizing the expectation of the complete data log likelihood. This iterative process finds the parameters at the *(t+1)*th iteration as;

$$\alpha_k^{t+1} = \frac{1}{N} \sum_{i=1}^{N} p(k \mid x_i, \Theta^t) \tag{2.15}$$

$$\mu_k^{t+1} = \frac{\sum_{i=1}^{N} x_i p(k \mid x_i, \Theta^t)}{\sum_{i=1}^{N} p(k \mid x_i, \Theta^t)} \tag{2.16}$$

$$\sum_k^{t+1} = \frac{\sum_{i=1}^{N} p(k \mid x_i, \Theta^t)(x_i - \mu_k^{t+1})(x_i - \mu_k^{t+1})^T}{\sum_{i=1}^{N} p(k \mid x_i, \Theta^t)} \tag{2.17}$$

We used the EM method for parameter estimation, which classifies each pixel into the class with the largest probability distribution using maximum likelihood, for identification of the GMM parameters.

2.7.3. Initialization of the EM algorithm

Initialization of the EM algorithm is important step because we are unlikely to guess correctly for the first time. However, based on our initial estimation of

parameters, we can make a better estimation at pairing data with components. The initial clusters of the EM algorithm are found using K-means for our datasets. Because there is not any common initialization method that works well for all kind of images, the way is to try different approaches and then to choose the best solution with the value that has the highest log likelihood (for an overview about the EM initialization see (Figueiredo and Jain 2002, Maitra 2009).

2.8. Active Contours

Active contour techniques are widely used for image segmentation. Several reviews about active contour methods have been published (Chakraborty and Duncan 1999, Frangi 2001,Xu et al.2000). The reason for the extensive research on active contours is that they can generate closed curves by using images and achieve sub-pixel accuracy. Also, they provide robustness for spurious edges by incorporating smoothness constraints.

Active contour model based approaches are categorized as parametric (explicit) active contours, which are formulated by using parameterized contours in a Lagrangian framework, and geometric (implicit) active contours, which are formulated by using the zero level set of a signed distance function in an Eulerian framework.

2.8.1. Parametric Active Contours

Early active contour based models are formulated by using parametric active contours, $C(s,t):[0,1]\times[0,\infty)\to R^2$ and $C(s,t)=[x(s,t),y(s,t)]$ where s is arclength and a spatial parameter in [0, 1], which parameterizes points in the curve, t is a temporal variable in $[0,\infty)$ (Kass et al 1987). Mathematically, a parametric active contour is defined as a time-varying curve. The formulation of the dynamics of the curve is written as,

$$C_t = F_{\text{internal}} + F_{\text{external}} \tag{2.18}$$

In (2.18), C_t is the partial derivative of C with respect to t, i.e. $\frac{\partial C(s,t)}{\partial t}$. The term F_{internal} represents internal forces and F_{external} represents external forces. The contour

stops when the net effect of these forces reaches to zero. The internal force consists of the sum of rigid elastic forces that are written as,

$$F_{rigid} = \left[\beta(s,t)C_{ss}(s,t)\right]_{ss} \tag{2.19}$$

$$F_{elastic} = \left[\alpha(s,t)C_{s}(s,t)\right]_{s} \tag{2.19}$$

where $\alpha(s,t)$ and $\beta(s,t)$ are coefficients. $\alpha(s,t)$ controls the tension (elasticity) while $\beta(s,t)$ controls the rigidity (stiffness) of the contour. Generally, in practice, $\alpha(s,t)$ is a positive constant, $\beta(s,t)$ is zero. The external force is designed to move active contours towards the desired object boundaries to be segmented. Different type of external forces can be seen in (Cohen L. D. 1991, Cohen and Cohen 1993, Kass et al. 1987, Ronfard R. 1994, Xu et al 2000, Xu and Prince 1998, Zhu and Yuille 1996).

The deformation of the active contour is performed to minimize energy functional for image segmentation. Because, the energy functional takes the minimum value when the active contours are smooth and reside on image boundaries. The energy equation is defined with the internal energy, which is obtained by the internal forces, and the external energy, which is obtained by the external forces, as

$$E = \int_0^1 \tfrac{1}{2}\left(\alpha\left|C_s(s)\right|^2 + \beta\left|C_{ss}(s)\right|^2\right)ds + \int_0^1 E_{ext}(C(s))ds \tag{2.20}$$

There are several major drawbacks of the snake method such as dependency of the parameterization of the initial contour or not capable of handling topological changes. Because this method can only controls the smoothness and attraction of the contour to the desired boundaries. Also, the magnitude of the external forces become smaller very quickly while evolving from the image boundaries which causes small capture range of snakes. Therefore, several parametric active contour approaches have been proposed (Amini et al 1990, Cohen and Cohen 1993, Xu and Prince 1998a, McInerney and Terzopoulos 2000, Ronfard 1994, Zhu and Yuille 1996, Giraldi 2000, Xu and Prince 1998b, Ostlad and Tonp 1996, Fenster and Kender 2001, Delingette and Montagnat 2001, Williams and Shah 1992) For example, the methods in (Ronfard 1994, Zhu and Yuille 1996, Xu and Prince 1998a, Cohen and Cohen 1993) use different external forces which are edge-based or region based to handle topological changes. Shape based prior information is used in (Ostlad and Tonp 1996, Fenster and Kender 2001) for contour evolution and to avoid spurious edges.

2.8.2. Geometric Active Contours (Level Set)

The original geometric active contour approach, which was proposed in two independent studies (Caselles et al 1993, Malladi et al 1995), uses both image data and geometric information of the evolving contour for image segmentation. The active contour methods in this category are based on the LSM (Osher and Sethian 1988) and the theory of curve evolution (Kimia et al 1990). The relationship between parametric and geometric active contours and also the corresponding level set equations of parametric active contours can be read in (Xu et al 2000). In geometric active contour models, curve evolves by using geometric measures which does not depend on curve's parameterization.

According to the curve evolution theory, the deformation of the curve is written by a PDE. The importance of PDEs has been increased in segmentation area since the first implementation of the LSMs as image segmentation at the beginning of the 1990's. The main reason for this is that a segmentation problem can be transformed into a PDE framework. Also, PDEs can use regularizers with these segmentation models. Another reason is that finite difference methods can be used to solve PDEs. Also, PDEs can be extended from 2-D to higher dimensions. In addition to these advantages, the solutions from the PDEs are fast and they are able to perform an image segmentation operation interactively.

The curve evolution theory expresses the following PDE for the deformation of the contour as,

$$\frac{\partial C(s,t)}{\partial t} = F(\kappa)\vec{N} \tag{2.21}$$

that evolves the contour $C(s,t)$ by the time t in the normal vector direction N with the speed function $F(\kappa)$, which depends on the curvature of the contour. Here, the normal vector N is the inward oriented.

The speed function contains a constant and a curvature dependent component that is written as,

$$F(\kappa) = F_0 + F_1\kappa \tag{2.22}$$

Therefore, if the curvature is high then the evolution of the contour is fast, if the curvature is low then the evolution is slow. The contour curvature keeps the evolving

contour to be smooth similar to the internal energy term in the parametric active contour method.

2.8.2.1. Main Idea of LSMs

The PDE given in (2.21) can be converted to another PDE that is level set evolution equation. For this purpose, the active contour is embedded into a time dependent LSF as the zero level set. Therefore, the main idea behind the LSM is to represent an active contour $C(s,t)$ as the zero level set of a smooth function ϕ, which is a higher dimensional and called as the LSF, and to evolve this contour to the edges of the desired objects. With this representation, the evolution of the curve is formulated by a time dependent Hamilton-Jacobi equation of the LSF.

The evolving contour, which is embeded as the zero level set of the function $\phi(x,y,t)$ is written as,

$$\phi\big(C(s,t),t\big)=0 \tag{2.23}$$

The level set technique is applied iteratively in an *n* dimensional space by using an active contour in an *n+1* dimensional space. LSFs are signed distance functions and defined as the closest distance between each point (x,y) and the zero level set. The value of the distance is positive if the points are inside the contour and it is negative if the points are outside (Osher and Sethian 1988). To use different distance metrics, such as Euclidean or chessboard distance, affects the level sets for image segmentation (Sandeep et al 2011).

The following motion equation is obtained, if we differentiate equation (2.23) with respect to *t* as,

$$\frac{\partial\phi}{\partial t}+\nabla\phi\frac{\partial C}{\partial t}=0 \tag{2.24}$$

Then, the level set equation is written as follows by using the equation given in (2.21)

$$\frac{\partial\phi}{\partial t}+\nabla\phi\cdot F(\kappa)\vec{N}=0 \tag{2.25}$$

The normal vector to the interface is the normal vector to the zero level set. Therefore, we have

$$\vec{N} = \frac{\nabla \phi}{\|\nabla \phi\|} \tag{2.26}$$

Then we obtain the level set equation as

$$\frac{\partial \phi}{\partial t} + F(\kappa)\|\nabla \phi\| = 0 \tag{2.27}$$

A stopping term,

$$g\left(|\nabla I|\right) = \frac{1}{1+\left|\nabla\left(G_\sigma * I(x,y)\right)\right|} \tag{2.28}$$

is used to incorporate the image data with the level set equation (Caselles et al., 1993, Malladi et al., 1995) and multiplied with the speed function *F(κ).* Here, $G_\sigma * I(x,y)$ is a convolution of the image *I(x,y),* where we are searching the contour of an object, with a Gaussian filter G_σ for smoothness. Therefore, the curve evolves in smooth regions when the value of the stopping term is close to one and the evolution stops when this term is close to zero.

The LSM uses the solution of a Hamilton-Jacobi equation of the higher dimensional smooth LSF ϕ for the contour evolution. An important advantage to use the Eulerian Hamilton-Jacobi equation is that the given LSF always remains as a function as long as the speed function is smooth (Osher and Sethian 1988). Another advantage of the level set approach is that the geometric properties of the contour can be obtained by using a level set of the surface ϕ. For example, we can derive an expression for the curvature in terms of ϕ as,

$$\kappa = \nabla \cdot \frac{\nabla \phi}{\|\nabla \phi\|} = \frac{\phi_{xx}\phi_y^2 - 2\phi_{xy}\phi_x\phi_y + \phi_{yy}\phi_x^2}{\left(\phi_x^2 + \phi_y^2\right)^{\frac{3}{2}}} = div\left(\frac{\nabla \phi}{\|\nabla \phi\|}\right) \tag{2.29}$$

Because, the arc-length parameterization and the curve derivatives according to it are geometric, intrinsic and also invariant to Euclidean transformations (Kimmel 2003). The value of the function ϕ does not change. Therefore, $\frac{\partial^n \phi}{\partial s^n} = 0$. Then, the following equations can be written for $n = 2$.

$$\begin{aligned}\phi_{ss}(x,y) &= \frac{\partial}{\partial s}(\phi_x x_s + \phi_y y_s) \\ &= \phi_{xx}x_s^2 + 2\phi_{xy}x_s y_s + \phi_{yy}y_s^2 + \phi_x x_{ss} + \phi_y y_{ss}\end{aligned}$$

$$= \phi_{xx} x_s^2 + 2\phi_{xy} x_s y_s + \phi_{yy} y_s^2 + \langle \nabla\phi, C_{ss} \rangle$$

(Recall that $\vec{N} = \{-y_s, x_s\} = \left\{ -\frac{\phi_x}{\sqrt{\phi_x^2+\phi_y^2}}, \frac{\phi_y}{\sqrt{\phi_x^2+\phi_y^2}} \right\} = \frac{\nabla\phi}{|\nabla\phi|}$ and $C_{ss} = \kappa\vec{N} = \left\{ \kappa \frac{\phi_x}{\sqrt{\phi_x^2+\phi_y^2}}, \kappa \frac{\phi_y}{\sqrt{\phi_x^2+\phi_y^2}} \right\}$)

$$0 = \frac{\phi_{xx}\phi_y^2 - 2\phi_x\phi_y\phi_{xy} + \phi_{yy}\phi_x^2}{|\nabla\phi|^2} + \langle \nabla\phi, C_{ss} \rangle$$

$$0 = \frac{\phi_{xx}\phi_y^2 - 2\phi_x\phi_y\phi_{xy} + \phi_{yy}\phi_x^2}{|\nabla\phi|^2} + |\nabla\phi|\kappa$$

$$\kappa = -div\left(\frac{\nabla\phi}{|\nabla\phi|} \right) \tag{2.30}$$

Also, following of contour evolution in three dimensional spaces is similar to following in two dimensional spaces because propagating surfaces are easily obtained by extending the arrays and gradients operators.

LSFs are signed distance functions which define the closest distance between each point *(x,y)* and the zero level set. In other words, signed distance functions are adopted to represent LSFs for accuracy and stability of LSMs. Generally, the sign of the distance is taken as positive if the points are inside the zero level contour and negative if they are outside. The speed function *F* depends on the LSF ϕ and image data for image segmentation. The advantage which is presented with this approach is that active contours represented by LSF can merge or break during evolution and handle topological changes. Also, the LSF remains a whole function on the fixed Cartesian grid that provides efficient computations.

2.8.2.2. Re-initialization of LSMs

There is a contradiction between the theory of the LSM and its implementation (Gomes and Faugeras 2000). Because, keeping the LSF as a signed distance function during the evolution is required for numerical stability of the curve evolution. However, the evolution equation written as in the form of (2.27) using a speed function *F* does not have a term to keep the LSF as a signed distance function. In theory of the LSM, solutions of this kind of Hamilton-Jacobi equations are not signed distance functions (Barles et al 1993). In practice, the LSF usually develops shocks and becomes very sharp or flat shape near the zero level set during evolution. The irregularities of the LSF

lead to inaccurate computations that destroy numerical stability of the evolution (Sethian 1999). A common numerical solution for this problem is to re-initialize (re-shape) the degraded LSF to a signed distance function either periodically or after stopping the evolution intentionally. Therefore, the re-initialization process to obtain the regularity of the LSF is a disagreement between the implementation and the theory of the LSF (Gomes and Faugeras 2000).

The re-initialization is still a serious problem since it is not known how to re-initialize and when it should be applied to maintain the stability of the evolution (Gomes and Faugeras 2000). A commonly used re-initialization method is to solve the equation defined as,

$$\frac{\partial \phi}{\partial t} = sign(\phi_0)\left(1 - \left|\nabla \phi\right|\right) \tag{2.31}$$

In (2.31), ϕ_0 is the function to be re-initialized. The term $sign(\phi_0)$ is the sign function which has an important property that the gradient value of a distance function is equal to a unit vector, $\left|\nabla \phi_0 = 1\right|$. The evolution of the LSF with speed *F* causes to lose this property. The LSF is re-initialized to restore this property. This re-initialization is widely used (Peng et al 1999, Sussman and Fatemi 1999).

Another re-initialization method (Sussman et al 1994) iteratively solves a re-initialization equation. However, this method is not successful if the LSF is far away from a signed distance function. The proposed method in (Peng et al 1999) identifies this problem and uses a new signed distance function. However, this method shifts the interface to a degree (Osher and Fedkiw 2002). The proposed method in (Russo and Smereka 2000) to preserve the interface as stationary and to localize it correctly uses an upwind discretization. However, none of these mentioned methods for re-initialization may move the zero level set incorrectly to an unexpected position and cause undesirable results (Osher and Fedkiw 2002, Sethian 1999, Peng et al 1999). Therefore, elimination of re-initialization is preferred. VLSMs have been proposed to avoid costly re-initialization process.

2.8.2.3. VLSMs

VLSMs can be converted to PDE based LSMs (Zhao et al 1996). VLSMs are more useful to incorporate shape or region based information and to get more robust

results. For example, the popular Chan-Vese formulation (Chan and Vese 2001) adds region based information into their energy functional that is proposed for image *I(x,y)* in domain Ω as,

$$E(C,c_1,c_2)=\lambda_1\int_{outside(C)}\left|I(x,y)-c_1\right|^2dxdy+\lambda_2\int_{inside(C)}\left|I(x,y)-c_2\right|^2dxdy \\ +\mu Length(C) \tag{2.32}$$

where c_1 and c_2 are constants that represent average intensities inside and outside the contour. λ_1, λ_2 and μ are positive weighting parameters. The problem in (2.32) is that the integration limits and the integral are not known. Therefore, a LSF is used to overcome this problem. Since, it is possible to represent the unknown curve *C* as the zero level set of function ϕ. For this purpose, assume $\Omega\to R$ such that

$$\begin{aligned} C&=\partial\Omega_1=\left\{(x,y)\in\Omega\,|\,\phi(x,y)=0\right\}\\ inside(C)&=\Omega_1=\left\{(x,y)\in\Omega\,|\,\phi(x,y)>0\right\}\\ outside(C)&=\Omega_2=\left\{(x,y)\in\Omega\,|\,\phi(x,y)<0\right\}\end{aligned} \tag{2.33}$$

Also, the Heaviside function and the Dirac delta is defined as

$$H(x)=\begin{cases}1, \text{ if } x\ge 0\\ 0, \text{ if } x<0\end{cases} \qquad \text{and} \qquad H'(x)=\delta(x) \tag{2.34}$$

Then, the equation (2.32) is written as,

$$E(\phi,c_1,c_2)=\lambda_1\int_\Omega\left|I(x,y)-c_1\right|^2H(\phi(x,y))dxdy+\lambda_2\int_\Omega\left|I(x,y)-c_2\right|^2(1-H(\phi(x,y)))dxdy \\ +\mu\int_\Omega\left|\nabla H(\phi(x,y))\right|dxdy \tag{2.35}$$

The segmented image after obtaining the LSF ϕ is given as,

$$u=c_1H(\phi)+c_2(1-H(\phi)) \tag{2.36}$$

The regularized *H* and δ functions are used to find the unknown LSF ϕ due to un-differentiability of *H* at the origin. The regularized terms are;

$$H_\varepsilon(x)=\frac{1}{2}\left(1+\frac{2}{\pi}\arctan\left(\frac{x}{\varepsilon}\right)\right), \qquad \delta_\varepsilon(x)=H'_\varepsilon(x)=\frac{\varepsilon}{\pi\left(\varepsilon^2+x^2\right)'} \tag{2.37}$$

Here, $H_\varepsilon\to H$ when $\varepsilon\to 0$. We can write the regularized energy function as,

$$E_\varepsilon(\phi, c_1, c_2) = \mu\int_\Omega \delta_\varepsilon(\phi(x,y))|\nabla\phi|dxdy + \lambda_1\int_\Omega |I(x,y)-c_1|^2 H_\varepsilon(\phi(x,y))dxdy + \lambda_2\int_\Omega |I(x,y)-c_2|^2 (1-H_\varepsilon(\phi(x,y)))dxdy \tag{2.38}$$

Then, the Euler-Lagrange equation for the ϕ function is found by the minimization of the energy functional E (2.38) that can be solved by the following evolution equation (Evans 1998) that

$$\frac{\partial\phi}{\partial t} = -\frac{\partial E}{\partial\phi} \tag{2.39}$$

The obtained equation for the unknown ϕ function is,

$$\begin{cases} \delta_\varepsilon(\phi)\left[\mu\nabla\left(\frac{\nabla\phi}{|\nabla\phi|}\right) - \lambda_1(I(x,y)-c_1)^2 + \lambda_2(I(x,y)-c_2)^2\right] = 0, & \text{in } \Omega \\ \frac{\delta_\varepsilon(\phi)}{|\nabla\phi|}\frac{\partial\phi}{\partial\vec{N}} = 0, & \text{on } \partial\Omega \end{cases} \tag{2.40}$$

Here $\frac{\partial\phi}{\partial\vec{N}}$ is the normal derivative of the LSF ϕ at boundary, $\vec{N}$ is the unit normal vector. The piecewise segmented image by using the computed ϕ function is,

$$u(x,y) = H_\varepsilon(\phi(x,y))c_1 + (1-H_\varepsilon(\phi(x,y)))c_2 \tag{2.41}$$

The terms c_1 and c_2 are found by minimizing E given in (2.32). This minimization is performed by keeping $\phi(x,y)$ as fixed and computing the derivative with respect to c_1 and c_2 . If $\int_\Omega H(\phi(x,y))dxdy > 0$, which means that the curve has an interior region in Ω, then we obtain that

$$c_1(\phi(x,y)) = \frac{\int_\Omega I(x,y)H(\phi(x,y))dxdy}{\int_\Omega H(\phi(x,y))dxdy} \tag{2.42}$$

If $\int_\Omega (1-H(\phi(x,y)))dxdy > 0,$ which means that the curve has an exterior region in Ω, then we obtain that

$$c_2(\phi(x,y)) = \frac{\int_\Omega I(x,y)(1-H(\phi(x,y)))dxdy}{\int_\Omega (1-H(\phi(x,y)))dxdy} \tag{2.43}$$

The stopping process in this method does not depend on image gradients. The stopping term depends on the result of the Mumford-Shah segmentation method (Mumford D. and J. Shah 1989). This model can detect objects whose edges are not defined by gradient or whose edges are very smooth due to the lack of an edge indication function. This model is not successful to segment images which have inhomogen intensities.

There are many variational level set based segmentation models in the literature (Rada and Chen 2012, Zhang et al 2012, Liu et al 2012, Yuan and He 2012).

CHAPTER 3

APPLIED APPROACHES FOR LIVER SEGMENTATION FROM MR IMAGES

3.1. Data Sets

In this study, upper abdominal MRI data sets have been used which were obtained from ten different patients using a 1.5 Tesla MR imaging device (Gyroscan Intera, Philips, ACS-NT, Best, The Netherlands) located in Dokuz Eylül University (İzmir, TURKEY) Radiology Department. The examined 16 bit DICOM images are fat suppressed T2-weighted (TR/TE, 1600/70 ms; flip angle, 90°; slice thickness, 8 mm) SPIR images (0.63 pixels per mm and the pixel size is 1.58x1.58 mm) in the axial plane with a resolution of 256x256.

The reason to choose T2 weighted SPIR images is its capability of better visualization of liver vessels. The segmented liver images will be used to label hepatic and portal veins and then to obtain Couinaud segments as an extension of this work. Therefore, the aim is to obtain segmented liver images from SPIR data sets.

3.2. Liver Segmentation by GMM

Model based classification that is based on parametric and finite mixture of distributions is a technique to estimate group membership for each data. A standard methodology of a model based clustering method is estimation of the finite mixture models that corresponds to each number of clusters by using the EM algorithm. The clustering is performed by assigning observed data to the cluster that is most likely belong to *a posteriori*, conditionally on the selected model and its estimated parameters.

In the model based clustering literature, the finite GMM classifier, which assumes that the data originates from a weighted sum of many Gaussian sources, is most commonly used in different fields such as pattern recognition (Sefidpour and Bouguila 2012, Jian and Vemuri 2011, Zhi Gao Zeng et al. 2011, McNicholas and

Murphy 2008, 2010), music (Marques and Moreno 1999, Christophe Charbuillet et al 2011) or text-independent speaker recognition (Reynolds, D. and Rose, R. 1995).

To our knowledge, the automatic GMM based clustering algorithm that we have proposed has not been applied for liver segmentation until now. Therefore, we have tested the probabilistic approach on our data sets to extract liver image.

In our implementation, the first step for liver segmentation with GMM is to select a slice in which the border of the liver is very clear in the dataset. It is usually the mid-slice of the datasets, which comes just after the first disappearance of the right kidney since the liver boundaries do not overlap with the other organ boundaries such as the heart and the right kidney. The selected slice is used as the initial slice to be segmented (Figure 3.1).

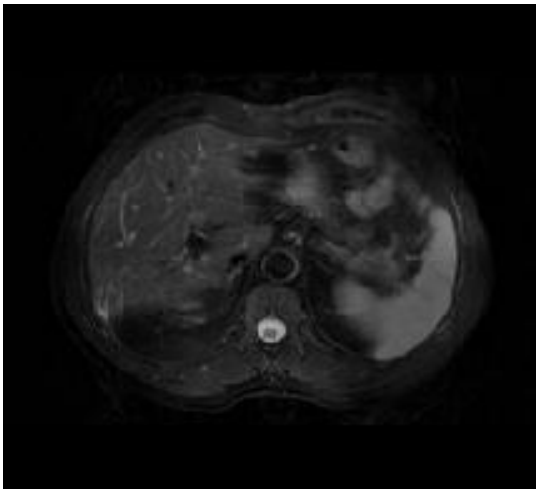

Figure 3.1. Initial slice

The second step is to use the spine location as a landmark to find the liver location in the selected initial slice since the liver is in the ribs and located in the left hand side of the selected slice. The spine will be in the bright cluster after the initial slice is clustered into three clusters (Figure 3.2.a) by using GMM with EM (Dempster et al.1977). Anatomical information is used to find spine position. Spine is located inside the ribs and in the middle from the bottom side of the abdominal image. Therefore, from left to the right, and from top to the bottom, the first non-zero values are found. Then, a rectangular frame is obtained by using these values (Figure 3.2.b). The point, where the first non-zero value from bottom, helps to find the row of the spine. The middle point of this row is used to draw another frame through the spine (Figure 3.2.c). At the right side of the spine, a seed region that includes some part of the liver is selected after the

detection of the spine location. Finally, image reconstruction (Vincent 1993) is performed to obtain the liver by using the selected seed image on the liver as a marker and the clustered image as a mask (Figure 3.2.a). The segmented initial liver image is obtained after morphological filling and closing operations (Figure 3.2.d).

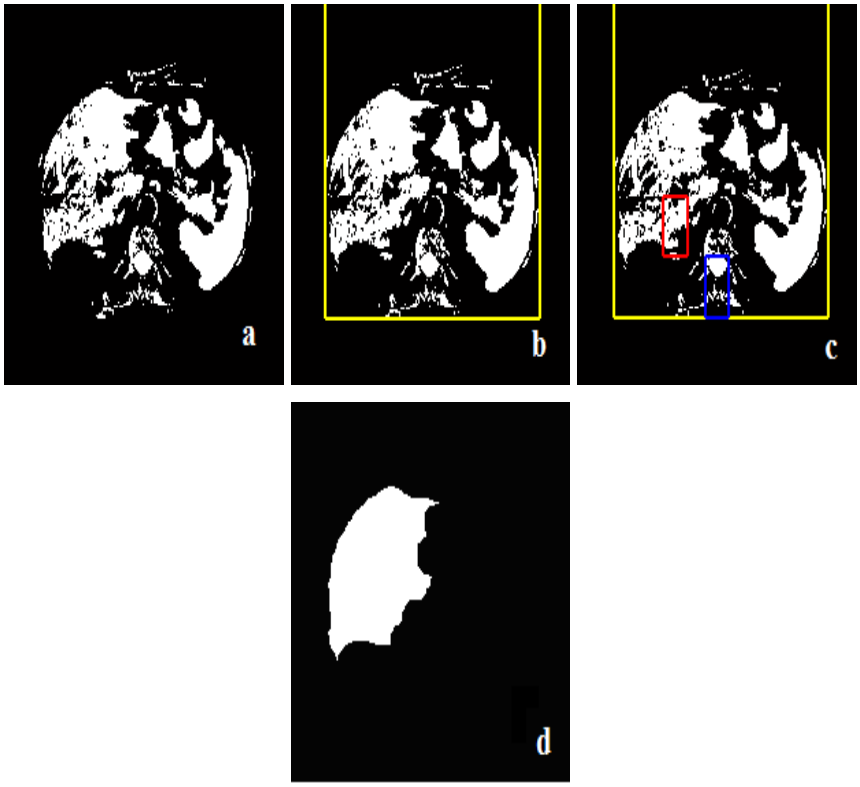

Figure 3.2. Clustered image (a); Rectangular frame around the image (b); Spine in the blue frame and the selected seed region in the red frame (c); Reconstructed liver after filling and closing operations (d)

Figure 3.3.a shows the segmented grayscale initial liver image to use as a reference image for the first succeeding (Figure 3.3.b) and preceding slice (Figure 3.3.c).

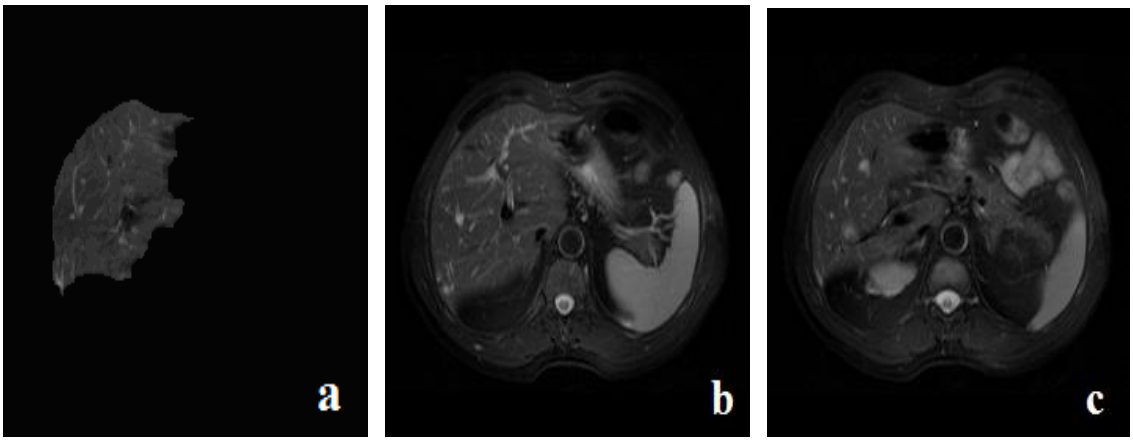

Figure 3.3. Initial liver image (a); The next slice to be processed (b); The previous slice to be processed (c)

The succeeding slices of the initial liver slice are clustered into three clusters, which are background, dark gray tissues (skin), bright gray tissues (organs). Spleen disappears and heart seems darker while kidneys appear in each preceding slice of the initial liver slice. This leads to changing of gray level distribution and an additional cluster, which shows the brightest regions, is required. Therefore, preceding slices are clustered into four clusters. The tissues of the liver are in the second and third cluster in the preceding and succeeding slices.

The skeleton (Figure 3.4.a) of the segmented initial liver image (Figure 3.3.a) is used as marker for both the next (Figure 3.3.b) and previous slice (Figure 3.3.c). The required masks for each slice to be segmented are their clusters that include liver tissues in the GMM (Figure 3.4.b). Image reconstruction process is applied with the binary mask and marker images to obtain the reconstructed liver image. Then the segmented grayscale liver image is obtained (Figure 3.4.c). The marker image for each previous slice is the skeleton image of the segmented previous liver. The marker image for each succeeding slice is the skeleton of the next liver (Figure 3.4.d). All remaining slices in the dataset are segmented iteratively by starting from the initial liver image to the end of the data set and from the initial liver image to the beginning of the data set. Because when borders are unclear between the spleen and liver or when we have atypical shaped liver, the radiologist examine the other slices, which comes just after or before where the borders are more visible, to decide liver border. The result of the GMM based method for the first succeeding slice of the initial liver image in Figure 3.4.c shows that the probabilistic approach is not successful to segment liver organ from SPIR data sets.

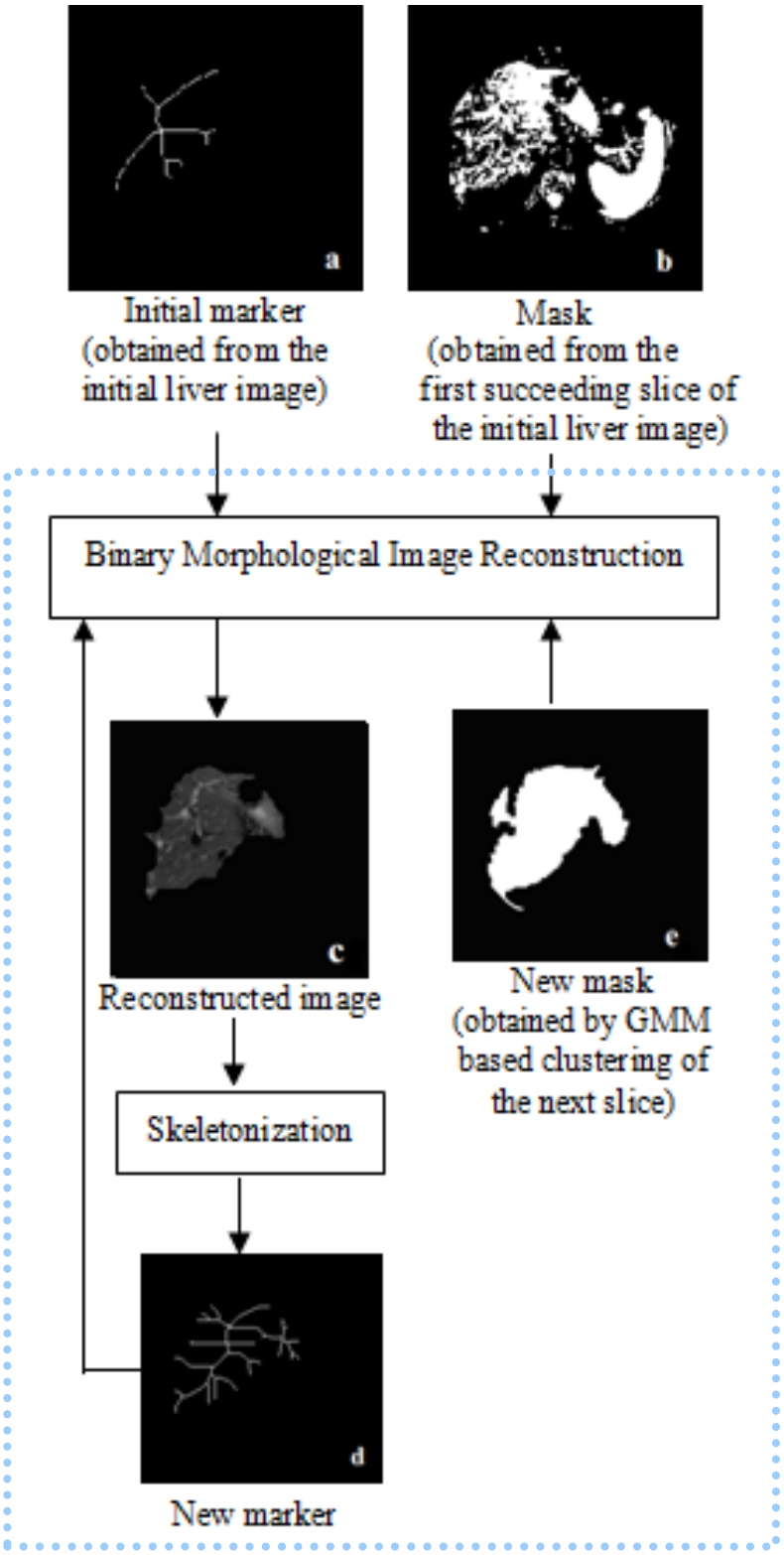

Figure 3.4. Skeleton of the initial liver image (Figure 3.3.a) to use as an initial marker (a); The result of GMM based clustering of the next slice (Figure 3.3.b) to use as a mask (b); Reconstructed grayscale liver image by using the mask and marker images (c); The skeleton image as a new marker (d) for the next slice; The next clustered image (e)

3.3. Liver Segmentation by K-means

K-means method explained in Section 2.5 is a widely used unsupervised clustering technique. There are many extensions of this method. However, they have generally application specific and have different drawbacks. For example, the proposed method to find the initial centers in (AbdulNazeer and Sebastian 2009) is computationally expensive. The extensions of K-means method in (Eschrich et al. 2003, Kaufman and Peter 2005, Fahim et al. 2006) are very sensitive to the initial starting points and also they do not promise to produce the unique clustering results. Because, in (Eschrich et al. 2003), data reduction by replacing group examples with their centers has been used before clustering them in order to speed up fuzzy c-means and K-means. K-medoid clusters have been represented in (Kaufman and Peter 2005) by using the median value of the data instead of the mean. In (Fahim et al. 2006), the required computational time is reduced by the assignment of the data elements to the most appropriate clusters with randomly selected initial centers.

When we search recently proposed methods that apply K-means for liver segmentation in the literature, we find several studies such as in (Selver et al. 2008, Liu et al. 2008), which use CT scans. For example, in (Selver et al. 2008), the original K-means method is used to segment liver organ from high contrast CT images. In (Liu et al. 2008), K-means is applied before support vector machine for segmentation by a binary classification method. However, MRI data sets are generally low contrast and have intensity inhomogeneity problem. Therefore, these approaches are not useful for MRIs.

There is only one proposed method (Chen et al. 2010) that applies K-means based liver segmentation approach by using MR images. The authors apply K-means method before implementation of Graph-Cut algorithm to identify liver pixels.

In this section, we have applied the same liver segmentation algorithm explained in Section 3.2. However, we have implemented the original K-means method (MacQueen 1967) instead of GMM clustering. In our application, Euclidean distance metric with batch update (Haykin 1999) has been applied in the K-means implementation. The gray values have been assigned to their closest cluster centers at once, and then re-computation has been performed to reassign the gray values to each

cluster centers at each iteration. The pseudo-code of the K-means method for the given set of data n $X = \{x_1, x_2, ...x_n\}$ and the given number of clusters k can be written as,

Step 1. Choose k data randomly as initial centers from the data set X

Step 2. Repeat

Find the cluster that has the closest center for each x_i

Assign each x_i to the cluster that has the closest center

Compute new centers for each cluster

Until convergence criteria is met

Figure 3.5.d shows an example result obtained by using the deterministic K-means clustering technique instead of GMM based clustering. Figure 3.5.a shows the segmented grayscale initial liver image to use as a reference image for the first succeeding slice (Figure 3.5.b). Figure 3.5.c and Figure 3.5.d is the reconstructed binary liver image and the grayscale liver image, which corresponds to the same slice shown in Figure 3.4.c in Section 3.2. It has been observed that the K-means based iterative method is not successful to segment liver organs from all SPIR slices.

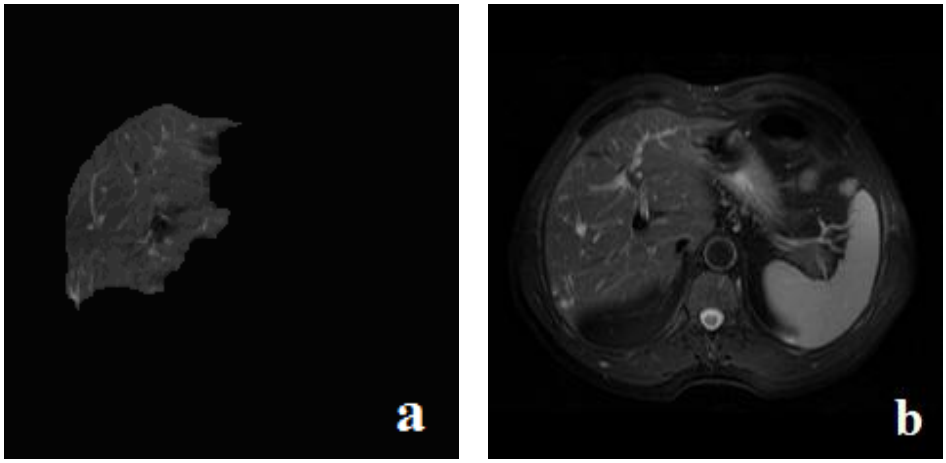

Figure 3.5. Initial liver image (a); The next slice to be processed (b); Reconstructed binary liver image (c); Grayscale segmented image (d)

(cont. on next page)

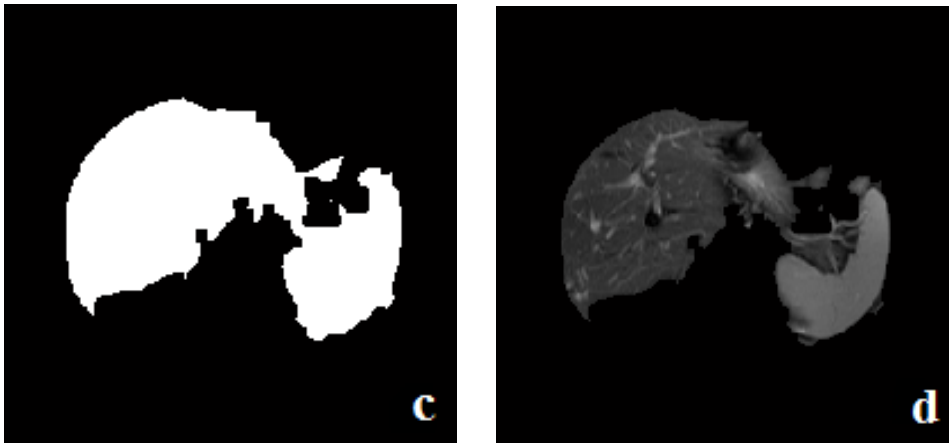

Figure 3.5. (cont.)

3.4. Liver Segmentation by MLP

Liver segmentation from SPIR data sets is performed by using neural networks, i.e. the MLP, in this section. Similar to the MLP based liver segmentation algorithm for CT images in (Selver et al. 2008), we have applied preprocessing steps to remove irrelevant organs (e.g., kidneys and spine) from our abdominal MR image datasets and used three features of the preprocessed images. However, unlike CT images, the ribs (Figure 3.6.a) do not seem on SPIR images. Therefore, there is not any process to remove ribs in our pre-processing stage. Also, unlike CT images, SPIR images show gallbladders as bright white organs (Figure 3.6.b) that affects the MLP based segmentation results. Therefore, we have segmented gallbladders in the preprocessing stage.

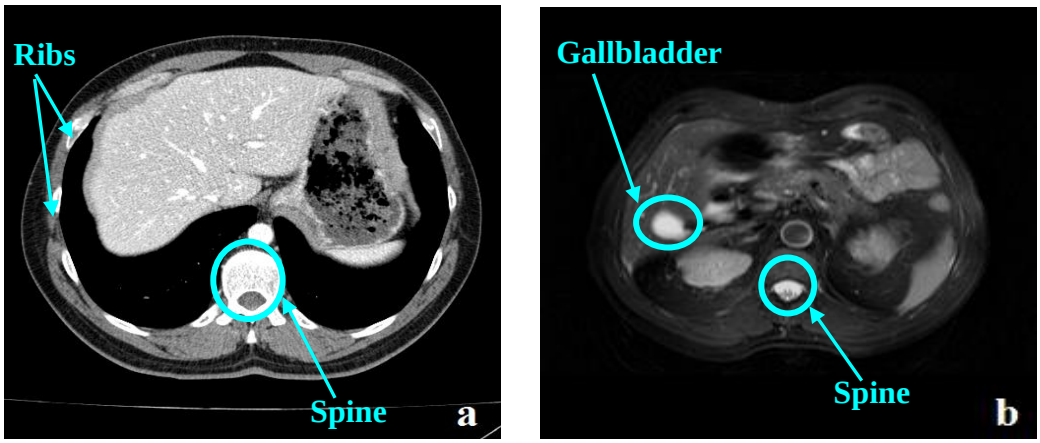

Figure 3.6. Example abdominal CT image that shows ribs and spine (a); Example abdominal SPIR image that shows gallbladder and spine (b)

The first step for liver segmentation with MLP is preprocessing. Preprocessing involves removing of irrelevant organs that are kidney, heart, spleen and gallbladder. Extraction of these irrelevant organs from SPIR data sets has been explained in Section 4.1.

An initial slice is selected after the pre-processing steps to obtain an initial liver and to use as the first reference image for the segmentation of the next and previous slice. The selected preprocessed initial slice (Figure 3.7.a), where the liver is the biggest relatively than the liver areas in other slices, is clustered by applying an optimal threshold with the Otsu's method (Otsu 1979), which gives a successful result only for the selected initial slice. The cluster, which has the liver organ (Figure 3.7.b), is selected from the three clusters that are background, dark regions (skin) and bright regions (liver) after the classification. Then, binary morphological operations are applied. The first operation is median filtering, which removes the small white spots from the background and black spots from the liver region (Figure 3.7.c). The next is erosion to break off the small connections (Figure 3.7.d) and connected component analysis to extract the biggest part in the image. Finally, dilation process is applied to restore the completely undeleted objects by erosion (Figure 3.7.e) gives the segmented initial liver image (Figure 3.7.f).

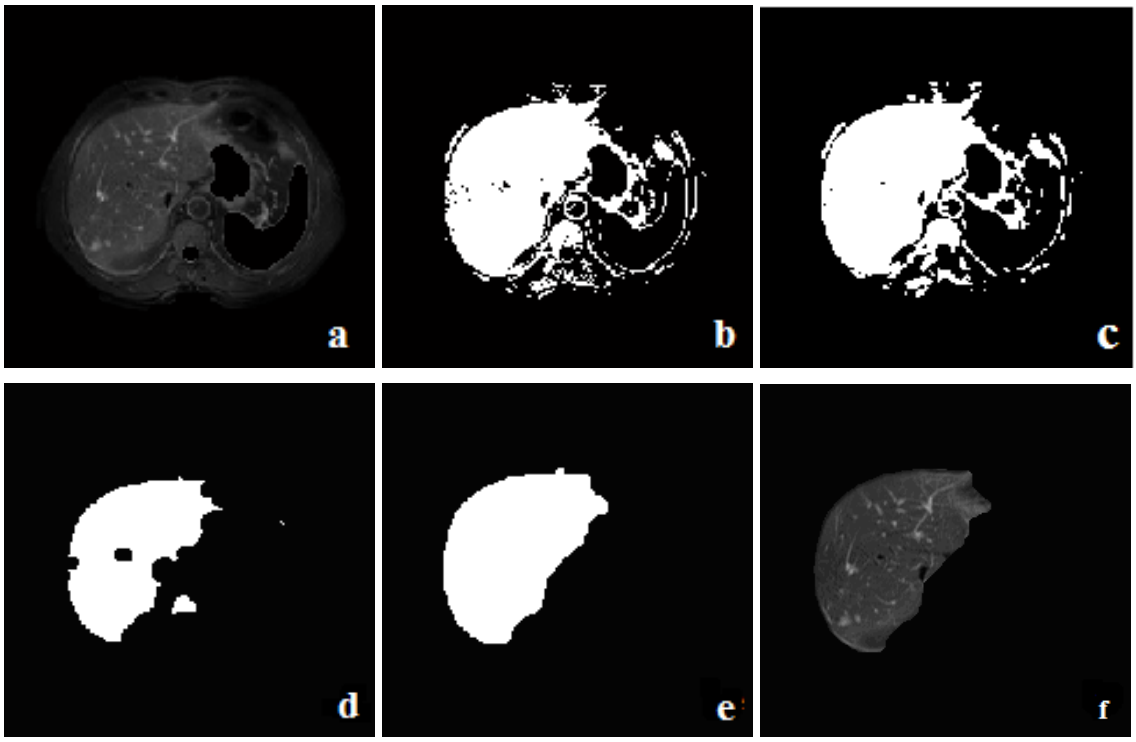

Figure 3.7. Segmentation of an initial image: Preprocessed (a); Clustered (b); Median filtered (c); Eroded (d); Dilation of the biggest part (e); Initial liver image (f)

The three features that are mean to represent the homogeneous regions, standard deviation to represent the edges and the distance transform to measure the separation of the pixels in the image to provide information about liver position are used. The standard deviation and mean value are computed by using the preprocessed initial image in the initial training step. The Euclidean distance transform feature is obtained using the same initial image after its clustering. We have preferred to use the probabilistic GMM based clustering instead of K-means clustering in this step. These three features are used as training data and the clustered initial liver image is used as the target output in the initial training step to obtain the initial weight values.

All slices are segmented iteratively after the initial training step by updating weights. The new current image that is the preprocessed next image to be segmented is used to calculate the new mean and standard deviation. The third feature, distance transform is computed using the previous segmented slice. These three features and the weights that are obtained from previous image are used for the image segmentation by applying MLP. The new weight values to use the next segmentation are computed by training the network. The three features are computed again for this training step with the result image and used as input. Also, the resulting image is used as the desired target image for this training. The segmentation procedure proceeds using the next image after the computation of the new weights. To use the previous weights for the next training step provides significantly less training time. Therefore, this iterative process increases the segmentation performance.

Figure 3.8 shows three example results obtained with this method. The MLP based liver segmentation method identified in this section gives the better result (Figure 3.8.a) than the result of the GMM based segmentation method (Figure 3.8.d) and the result of the K-means based segmentation method (Figure 3.5.b) for T2 weighted SPIR images.

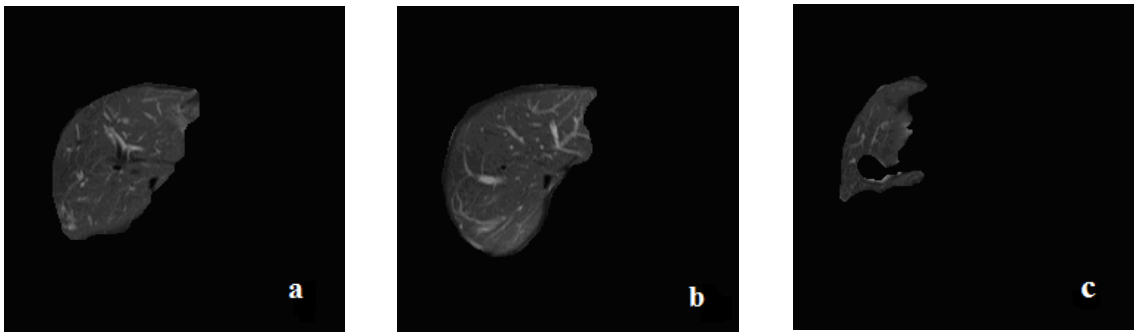

Figure 3.8. Example results of the MLP based liver segmentation method (a, b, c)

3.5. Liver Segmentation by LSMs

LSMs have been popular in the last fifteen years. Since, it is very flexible to adapt to many different problems and has the guarantee for the solutions that are exist in PDEs. Also, numeric methods have been developed extensively by using Hamilton-Jacobi equations to obtain stable numerical schemes and to handle shocks.

As explained in Section 2.8.2.1, the level set evolution equation is written by;

$$\frac{\partial \phi}{\partial t} + V(\kappa)|\nabla \phi| = 0 \tag{3.1}$$

Although the original LSM (3.1) does not contain any energy term, level set equations have been applied using an energy minimization term of the contour to handle topological changes and obtain accurate results in some improved LSMs (Wang et al. 2010, Rousson and Paragios 2002, Chan and Vese 2001, Paragios and Deriche 2002, Cohen and Kimmel 1997, Chen et al 2001, Leventon et al 2000, Caselles et al 1997, Wang et al 2004, Piovano et al 2007, Lankton et al 2008, An et al 2007, Li et al 2011). The energy minimization in LSMs is applied like an edge detection method. In these alternative approaches, an energy functional equation that will be minimized is defined on the LSF and an evolution PDE is obtained by using this energy functional instead of by an Eulerian equation as in classical LSMs (Caselles et al 1993, Caselles et al 1997, Malladi et al 1995, Osher and Fedkiw 2002). For example, minimization of the contour energy has been performed by optimizing a constraint that indicates the interior homogeneity degree of contour for the VLSM in (Wang et al 2004a). A constraint optimization method in (Cohen and Kimmel 1997) uses two selected points on the object boundary and computes the minimum global energy for a contour between these points. The supervised segmentation method in (Paragios and Deriche 2002) needs prior information for the object pattern to do energy minimization. Shape based prior information has been integrated to level set equations for accurate segmentation in (Leventon et al 2000, Chen et al 2001, Rousson and Paragios 2002). Only region based features have been used in (Chan and Vese 2001) by assuming the existence of only object and background in the image to construct the energy in order to minimize. However, the used global information in the proposed formulation is not accurate when there is intensity inhomogeneity in inside or outside the contour. Similarly, a piecewise constant model based LSM in (Vese and Chan 2002) and B-Spline based LSM in

(Bernard et al. 2009) can not handle intensity inhomogeneity problem. Local intensity information has been incorporated to the LSM as a solution for intensity inhomogeneity (Piovano et al 2007, Lankton et al 2008, An et al 2007). However, only mean values of local intensities do not enough for an efficient segmentation when there exists severe noise and intensity inhomogeneity. Therefore, both mean and variance values of local intensities, which are obtained by Gaussian distributions, have been used to deal with intensity inhomogeneity (Wang et al 2010). Although, this approach has not been tried for liver images, it gives accurate results for brain images but causes high computational cost.

In this section, we review different LSMs, which have been proposed recently, and present their implementation results for our abdominal MRI data sets.

3.5.1. LSM without PDE

Narrow banded LSMs (Chopp 1993, Peng et al 1999, Whitaker 1998, Goldenberg et al 2001) have been proposed to increase segmentation performance with reduced computation cost. In these methods, PDEs are solved only around the neighborhood of the zero level set instead of in the whole image to increase the evolution speed of the curve. A narrow banded LSM with a bandwidth of two pixels is proposed by Shi and Karl (Shi and Karl 2008). The authors propose the curve evolution by FTC algorithm that approximates the level set technique by using integer operations without PDEs to reduce the computation cost. The FTC algorithm is explained in detail in this section since we use it for the automatic liver segmentation method in Section 3.5.2.

There are two linked lists that are L_{in} and L_{out} to represent curve evolution in the FTC algorithm. The list L_{in} contains the grid points inside the contour. The list L_{out} contains the grid points outside the contour. The points that are inside L_{in} are known as interior points. The points that are outside L_{out} are known as exterior points. The LSF $\hat{\phi}$ is an integer array that contains the following values for each point *x*;

$$\hat{\phi}(x) = \begin{cases} 3, & \text{if } x \text{ is exterior point} \\ 1, & \text{if } x \in L_{out} \\ -1, & \text{if } x \in L_{in} \\ -3, & \text{if } x \text{ is interior point} \end{cases} \tag{3.2}$$

Curve evolution is achieved by a switching mechanism, which uses SwitchIn and SwitchOut functions. Figure 3.9 shows an example for outward evolution by one pixel at point *A* with the SwitchIn function. A neighbor of point *x* from exterior points is inserted into the L_{out} list after the outward evolution and redundant points are deleted from the L_{in} list. Similarly, an example for inward evolution with SwitchOut function by 1 pixel at point *B* is shown in Figure 3.9.

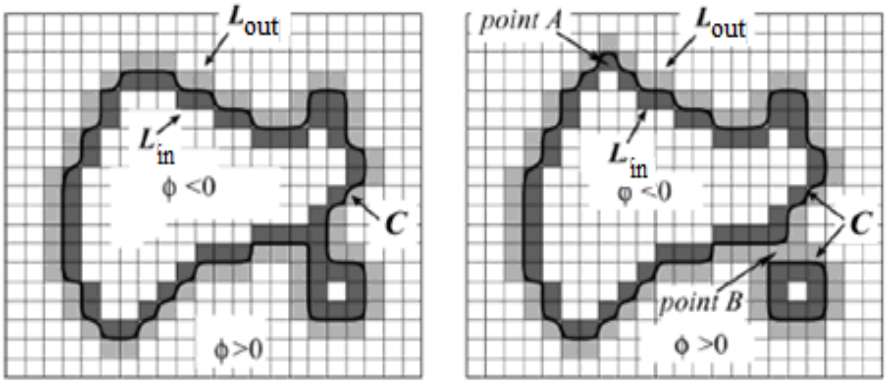

Figure 3.9. L_{in} and L_{out} are the lists that contain grid points and switching for evolution of the curve (Source: Shi and Karl 2008).

Two integer arrays are used for the speed functions that are $\hat{F}_d$ (data dependent speed) and $\hat{F}_{\text{int}}$ (regularization speed). If the curve evolution is inside (outside) then the sign of the speed functions is negative (positive). The first cycle of the FTC algorithm performs the curve evolution using the data dependent speed function $\hat{F}_d$. The second cycle of this algorithm performs the curve evolution using the smoothing speed $\hat{F}_{\text{int}}$ for smoothness regularization. The value of the data dependent speed function $\hat{F}_d$ is obtained by,

$$\hat{F}_d = k_l c - \left(\nabla k_l . \vec{N}\right) \tag{3.3}$$

where, $k_l(x, y)$ is the stopping term (2.28), *c* is a constant that receives 1 as default value. The sign of *c*, which gets value according to the balloon model (Cohen 1991), determine the direction of the evolution. The final value of this speed function $\hat{F}_d \in \{-1, 0, +1\}$ is obtained after thresholding of the computed value. The value of the smoothing speed function $\hat{F}_{\text{int}}$ is obtained by Gaussian filtering of the binary image that contains the value 1 for regions inside the contour and the value 0 for regions outside

the contour. The final value of this speed function $\hat{F}_{\text{int}} \in \{-1, 0, +1\}$ is obtained after thresholding of the result values in list L_{in} and L_{out}.

An example result of the FTC method is by using an original image (Figure 3.10.a) and an initial contour (Figure 3.10.b) is shown in Figure 3.10.c, which has a misclassified region (Figure 3.10.d).

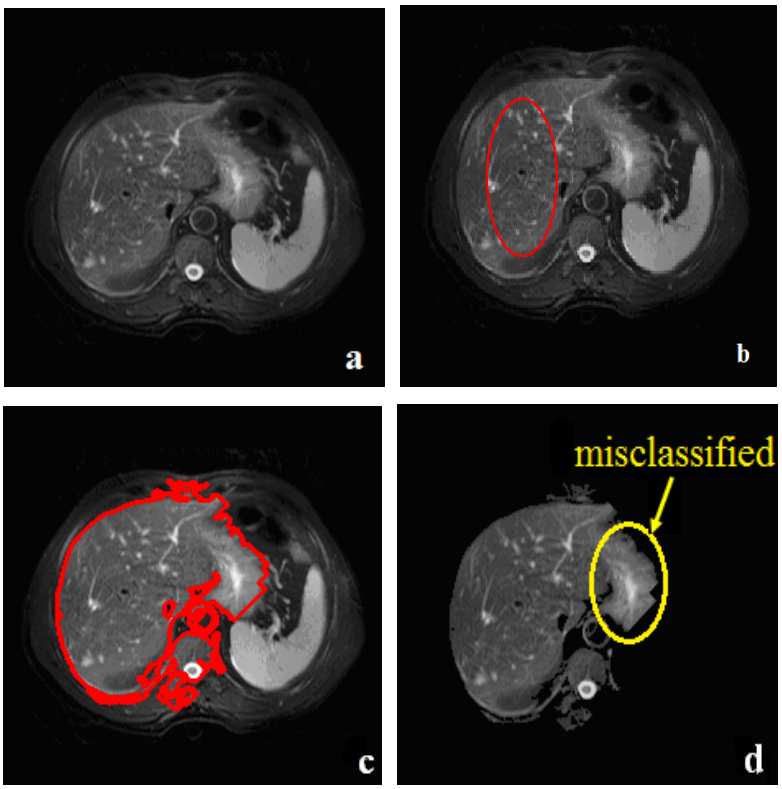

Figure 3.10. Original image (a); Initial contour (b); Result of the FTC method (c); Misclassified region (d)

3.5.2. Automatic Liver Segmentation without PDE

Initial contours can be propagated to outside or inside. The position of initial contours is a key challenge for level set based segmentation methods (Weeratunga and Kamath 2004). Each user can draw different initial contours at different locations and size. Also, to find the correct number of iteration for each initial contour is not easy. The segmentation results are not robust even the iteration numbers are given by users or a constant number of iteration is used due to different initial contours defined by users. Therefore, we need to apply level set approaches for liver segmentation automatically to overcome these drawbacks and obtain acceptable results from all slices in a dataset.

The liver shape in a slice is close to the liver shape of the preceding or succeeding slices with respect to other slices in the dataset. Therefore, the shape of an initial segmented liver image can be used as the initial contour for the next and previous slices. In (Goceri et al. 2012), we obtained the initial contour automatically for each slice by using this relation between sequential slices in a dataset and used the FTC algorithm without any user interaction for liver segmentation. However, we observed that the segmentation results are not robust. Therefore, we have applied the FTC algorithm after the pre-processing steps, which have been explained in Section 4.1, to increase segmentation performance.

The first step of this automatic segmentation algorithm is to obtain an initial liver image (Figure 3.7.f). Then, the shape of the initial liver image is used as the initial contour for liver segmentation from the first preceding and succeeding slices. Finally, binary morphological post-processing steps, which are erosion to remove weakly connected objects, connected component analysis to get the biggest part and dilation to restore the completely undeleted objects by erosion, are applied. All remaining slices are segmented iteratively with the same number of iteration, which is a very small number. We have used only ten iterations for each slice since the initial contour is very close to the desired liver edges. Therefore, the required time for the segmentation of each slice is reduced and better segmentation results are obtained automatically from all slices in the dataset. Example experimental images are shown in Figure 3.11 with two consecutive slices. The pre-processed image given in Figure 3.11.a is used for the automatic level set based segmentation with the initial contours (shapes of the previously segmented liver image) shown in Figure 3.11.b and the image given in Figure 3.11.c is obtained. The segmented liver image after post-processing is presented in Figure 3.11.d. Similarly, Figure 3.11.e shows the next pre-processed image to be segmented with the initial contour given in Figure 3.11.f. The applied automatic level set based segmentation result is shown in Figure 3.11.g and the image after post-processing is given in Figure 3.11.h.

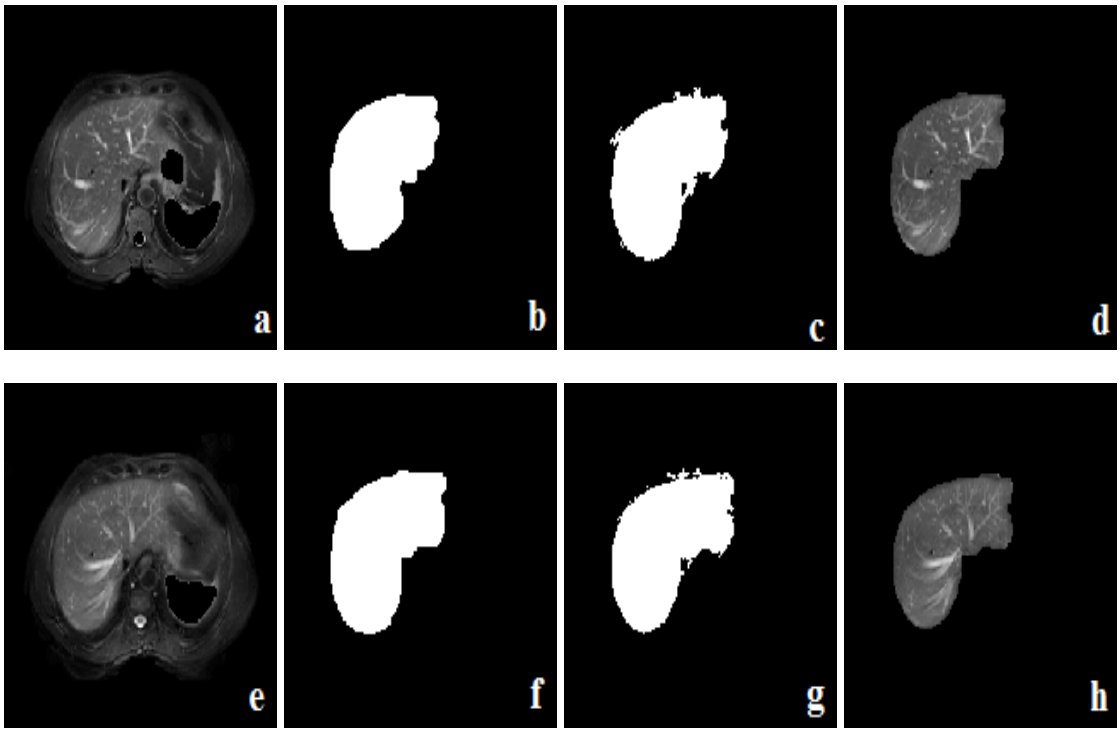

Figure 3.11. Pre-processed images (a, e); Shapes of the previous liver images to use as initial contours (b, f); Results of the automatic segmentation with the FTC algorithm (c, g); Segmented liver images after post-processing (d, h)

3.5.3. LSM with SPF Function

The implemented approach in this section uses an edge based active contour that is Distance Regularized Level Set Evolution (DRLSE) method (Li et al. 2010) to solve re-initialization problem of active contour evolution. Selective Binary and Gaussian Filtering Regularized Level Set (SBGFRLS) (Zhang et al.2010) method can control the active contour evolution and stop it effectively when an image has homogen intensity values. However, abdominal SPIR data sets have inhomogen intensities. Also, liver may have blurred or weak edges. Therefore, the functions those give average values of the intensities inside active contour and outside, which are defined with Local Binary Fitting (LBF) method (Li et al. 2007), are used to obtain a new SPF (Xu and Yezzi 2000) function.

The related works to the implemented level set approach in this section, which are DRLSE, LBF and SBGFRLS, are explained in the following sections. After these explanations, the DRLSE with SPF function based method is presented.

3.5.3.1. DRLSE Method

The advantage of DRLSE method is to eliminate the need of re-initialization. To explain this method, let us assume that the active contour is $C = \{(x, y) \in \Omega \mid \phi(x, y) = 0\}$, where $\phi(x, y) = 0$ is the zero LSF, $\Omega \subset \Re$ and the image $I : \Omega \to \Re$ is defined on Ω.

The energy function with a LSF is written as

$$E(\phi) = \mu R_p(\phi) + E_{ext}(\phi), \quad \mu \geq 0 \tag{3.4}$$

where μ is a constant and $E_{ext}(\phi)$ is the external energy. This energy function gets a minimum value when the zero level set is positioned at object boundaries for image segmentation. The external energy to be minimized is written as

$$E_{ext}(\phi) = \lambda L_g(\phi) + \alpha A_g(\phi), \quad \alpha \in \Re, \ \lambda > 0 \tag{3.5}$$

where λ, α are coefficients and g is the edge indicator function, which is written as,

$$g(|\nabla I|) = \frac{1}{1 + |\nabla G_\sigma * I|^2} \tag{3.6}$$

by using Gaussian kernel, $G_\sigma(x, y) = \sigma^{-1/2} e^{-|x^2+y^2|/4\sigma}$, with the standard deviation σ. The term $L_g(\phi)$ in (3.5) is the length of the active contour and expressed as

$$L_g(\phi) = \int_\Omega g\delta(\phi)|\nabla\phi| dxdy \tag{3.7}$$

Here δ(.) is the Dirac delta function. The term $A_g(\phi)$ is the area in the active contour and computed with the Heaviside function *H(.)* as

$$A_g(\phi) = \int_\Omega gH(-\phi)dxdy \tag{3.8}$$

The term $R_p(\phi)$ in (3.4) is the regularization term written as

$$R_p(\phi) = \int_\Omega p(|\nabla\phi|)dxdy \tag{3.9}$$

with a potential function (energy density) $p : [0, \infty) \to \Re$

Generally, the potential function is chosen as $p(s) = s^2$ for the term R_p, which forces that $|\nabla\phi| = 0$. Therefore, the regularization term has a good smoothing effect. However, the regularization term causes the LSF to be flattened and finally to disappear of the zero level contour.

In fact, the goal to use the regularization term is both to smooth the LSF and to maintain the signed distance property $|\nabla\phi|=1$ in order to perform accurate calculation of the curve evolution. To achieve this goal, *p(s)* with a minimum point $s=1$, can be used as a potential function so that the R_p is minimized when $|\nabla\phi|=1$. Therefore, *p(s)* should have a minimum value for $s=0$. The regularization term R_p is also called as distance regularization term due to its role for maintaining the signed distance property of the LSF.

It has been observed that the obtained level set evolution equation to minimize energy function has an undesirable effect on the LSF ϕ. To solve this problem, the potential function *p(s)* should be chosen so that the LSF satisfies $|\nabla\phi|=1$ for only in a vicinity of the zero level set and $|\nabla\phi|=0$ for locations that are far away from the zero level set. Therefore, *p(s)* must have two minimum points that are at $s=1$ and $s=0$. The potential function is written as,

$$p(s)=\begin{cases}\dfrac{1}{(2\pi)^2}\left(1-\cos(2\pi s)\right), & if \;\; s\le 1\\ \dfrac{1}{2}\left(s-1\right)^2, & if \;\; s\ge 1\end{cases} \tag{3.10}$$

As it is known, to obtain a minimum value of a function, a steady state solution of the gradient flow equation of this function can be found. The gradient flow equation of the energy function *E(ϕ)* is written as,

$$\frac{\partial\phi}{\partial t}=-\frac{\partial E}{\partial\phi} \tag{3.11}$$

where $\frac{\partial E}{\partial\phi}$ is the Gateaux derivative of the energy function *E(ϕ)*. This is an evolution equation of a time dependent LSF *ϕ(x,y,t)* with a spatial variable *x* and *y*. The evolution direction of *ϕ(x,y,t)* is opposite of the Gateaux derivative (i.e. $-\frac{\partial E}{\partial\phi}$), which is the direction of the steepest descent of the function *E(ϕ)*. Therefore, the gradient flow is known as gradient descent flow or steepest descent flow.

The Gateaux derivative for the regularization term $R_p(\phi)$ is written as,

$$\frac{\partial R_p}{\partial \phi} = -div\left(\frac{p'\left(|\nabla \phi|\right)}{|\nabla \phi|} \nabla \phi \right) \tag{3.12}$$

By using the equation (3.4), and the linearity of Gateaux derivative, we can write that

$$\frac{\partial E}{\partial t} = \mu \frac{\partial R_p}{\partial \phi} + \frac{\partial E_{ext}}{\partial \phi} \tag{3.13}$$

Therefore, we can write the following gradient flow equation of the energy function *E(ϕ)* by using (3.11) as,

$$\frac{\partial \phi}{\partial t} = -\mu \frac{\partial R_p}{\partial \phi} - \frac{\partial E_{ext}}{\partial \phi} \tag{3.14}$$

The equation in (3.12) can be written as follows by using (3.14);

$$\frac{\partial \phi}{\partial t} = \mu div\left(d_p\left(|\nabla \phi|\right) \nabla \phi \right) - \frac{\partial E_{ext}}{\partial \phi} \tag{3.15}$$

The equation in (3.15) is the level set evolution equation that has been derived from the equation (3.5). The derivative of the external energy function $\frac{\partial E_{ext}}{\partial \phi}$ is computed and written in (3.15). Then the following DRLSE equation is obtained;

$$\frac{\partial \phi}{\partial t} = \mu div\left(\frac{p'\left(|\nabla \phi|\right)}{|\nabla \phi|} \nabla \phi \right) + \lambda \delta_\varepsilon(\phi) div\left(g \frac{\nabla \phi}{|\nabla \phi|} \right) + \alpha g \delta_\varepsilon(\phi) \tag{3.16}$$

Figure 3.12 shows an example original image (Figure 3.12.a, e, i), an initial contour (Figure 3.12.b, f, j), the result obtained at the minimum value of the energy function (Figure 3.12.c, g, k) and also the result obtained at the maximum iteration number, which has been chosen as 950 to avoid over segmentation problem on other slices with kidneys (Figure 3.12.d, h, l). This method can not stop the curve evolution since the traditional edge stopping function that is based on only the gradient of the image is not efficient when intensities are inhomogen. Therefore, this method usually causes under/over segmentation problems when we apply it for liver segmentation from SPIR data sets.

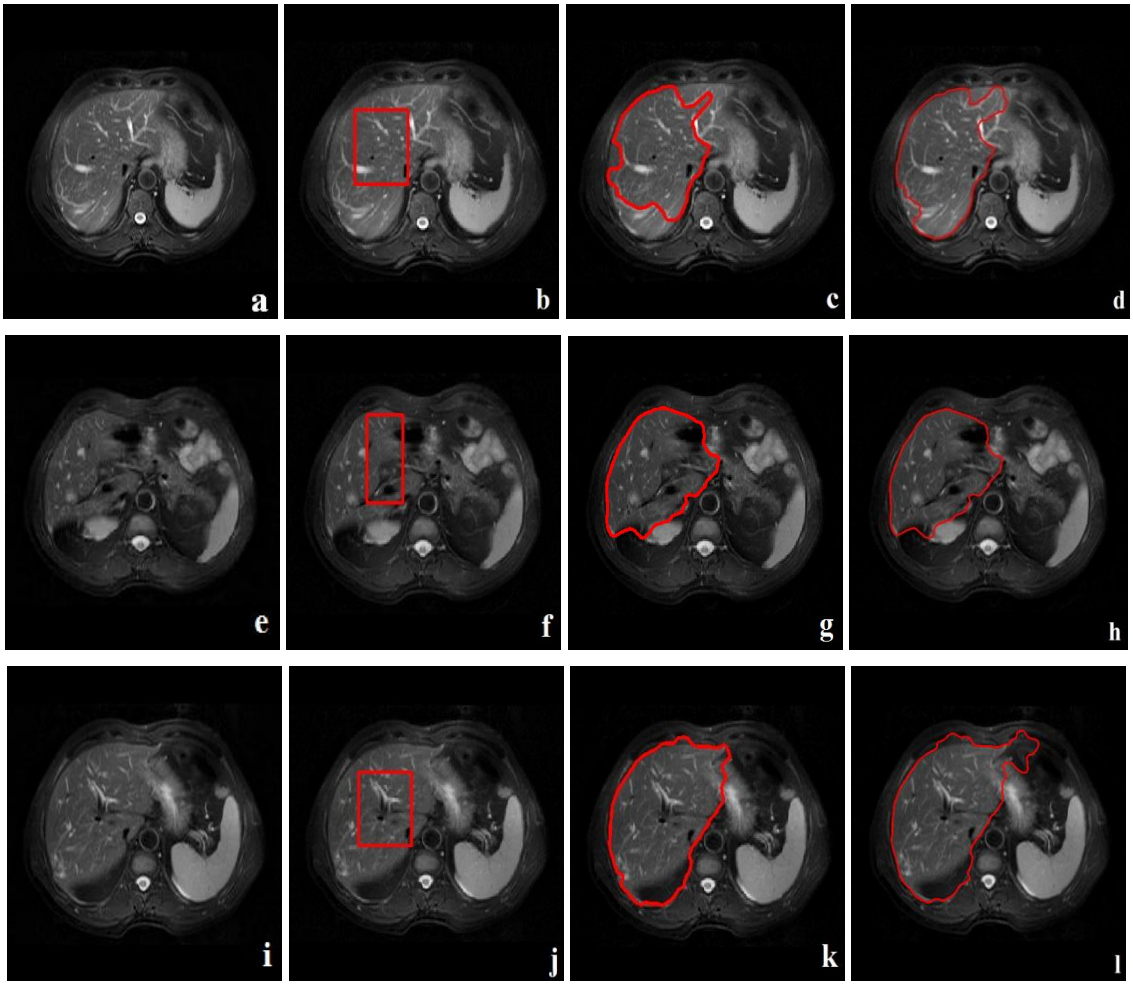

Figure 3.12. Original images (a, e, i); Initial contours (b, f, j); Segmented images at minimum energy levels (c, g, k); Segmented images at maximum number of iterations (d, h, l)

3.5.3.2. SBGFRLS Method

The SBGFRLS method uses the advantages of an edge based method (Caselles et al. 1997), which is very popular and known as Geodesic Active Contour (GAC) model, and a region based method (Chan and Vese 2001) called as C-V model. The advantage of the GAC model is its local segmentation property. Because it can segment the object if the initial closed curve surrounds its boundary. If the initial curve is set one inside of the object then detection of the interior contour is not possible with this model. Therefore, the initial contour has to be stated properly. The advantage of the C-V model is its insensitivity to positions of the initial contour.

The following energy functional is minimized in GAC method

$$E^{GAC}(C) = \int_0^1 g\left(\left|\nabla I(C(q))\right|\right)\left|C'(q)\right| dq \tag{3.17}$$

where $C(q):[0,1] \to R^2$ is a parametric curve in Ω, which is a bounded subset of R^2 and g is the edge stopping function as given in (3.6). The following Euler-Lagrange equation of (3.17) by using calculation of variation (Aubert and Kornprobst 2002) is obtained as

$$C_t = g\left(\left|\nabla I\right|\right)\left(\kappa + \alpha\right)\vec{N} - \left(\nabla g \cdot \vec{N}\right)\vec{N} \tag{3.18}$$

where κ is the curvature term, $\vec{N}$ is the inward normal vector and α is a constant velocity. Then, the level set evolution equation that corresponds to (3.18) is obtained as,

$$\frac{\partial \phi}{\partial t} = g\left|\nabla \phi\right|\left(div\left(\frac{\nabla \phi}{\left|\nabla \phi\right|}\right) + \alpha \right) + \nabla g \cdot \nabla \phi \tag{3.19}$$

The drawback of the GAC method is its sensitivity to initial contour position. The GAC approach, which uses traditional edge stopping function that is not efficient at weak edges, is not robust to noise.

The C-V method that is the most popular region based model, which has been explained in Section 2.8.2.3, is unsuccessful when images have in-homogeny intensity values.

The SBGFRLS method uses region based SPF function obtained by global statistical knowledge of the image. The SPF function can control the direction of the active contour evolution and defined as;

$$SPF = \frac{I(\mathrm{x}) - \left(C_1 + C_2\right)/2}{\max\left(\left|I(\mathrm{x}) - \left(C_1 + C_2\right)/2\right|\right)} \tag{3.20}$$

where $\mathrm{x} \in \Omega$ and the SPF function has values in range [-1,1]. In (3.20), C_1 and C_2 are constant average intensity values outside and inside the active contour respectively. These two constants are obtained by minimizing the C-V model as identified in (2.42) and (2.43), which can be written by;

$$C_1 = \frac{\int_\Omega I(\mathrm{x}) H_\varepsilon(\phi) d\mathrm{x}}{\int_\Omega H_\varepsilon(\phi) d\mathrm{x}} \qquad C_2 = \frac{\int_\Omega I(\mathrm{x})\left(1 - H_\varepsilon(\phi)\right) d\mathrm{x}}{\int_\Omega \left(1 - H_\varepsilon(\phi)\right) d\mathrm{x}} \tag{3.21}$$

where H_ε is Heaviside function and generally defined as;

$$H_\varepsilon(x) = (1/2)\left[1 + (2/\pi)(\arctan(x/\varepsilon))\right] \tag{3.22}$$

The level set equation of the SBGFRLS method is obtained by substituting the SPF function given in equation (3.20) for the edge stopping function in (3.19) as,

$$\frac{\partial \phi}{\partial t} = SPF(I(\mathrm{x})) \cdot \left(div\left(\frac{\nabla \phi}{|\nabla \phi|} \right) + \alpha \right) |\nabla \phi| + \nabla SPF(I(\mathrm{x})) \cdot \nabla \phi \qquad (3.23)$$

In equation (3.20), the SPF function is computed by using the statistical knowledge obtained from the whole image. However, the intensity values in MRIs are not homogeny. Therefore, the SBGFRLS method is not successful for MRI datasets in order to find the object boundaries due to the intensity inhomogeneity problem.

Figure 3.13 shows example images obtained from the SBGFRLS method at maximum number of iteration (950) and minimum energy level (Figure 3.13.a, b, c) by using the same original images given in Figure 3.12.a,e,i and initial contour given in Figure 3.12.b,f,j. It was observed that the active contour evolution stops before it reaches the maximum number of iteration because of the effect of SPF function. However, over/under segmentation occurs on some slices as in the DRLSE method.

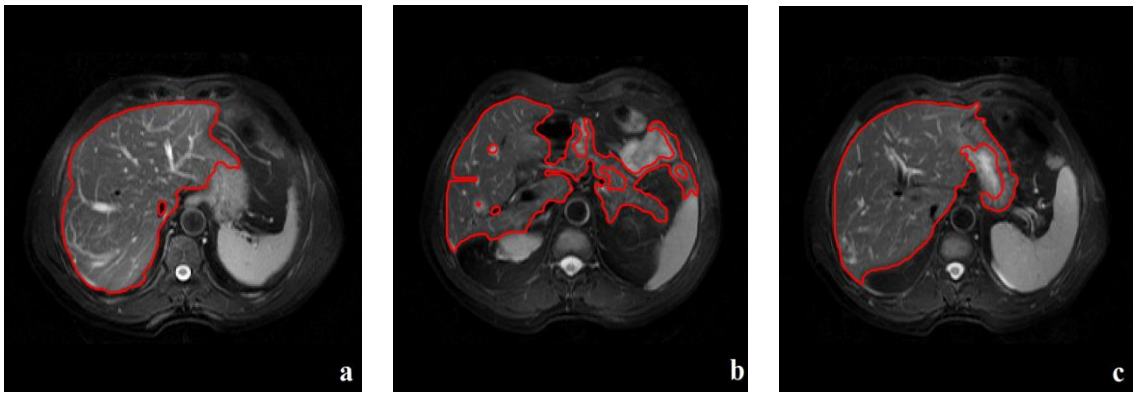

Figure 3.13. An example of segmented image with SBGFRLS method at maximum number of iteration and minimum energy level (a, b, c)

3.5.3.3. LBF Method

The following energy function is defined in this method with the active contour C for each point x in the image domain Ω as,

$$\begin{aligned} E_{\mathrm{x}}^{LBF}(C, f_1, f_2) = \lambda_1 \int_{in(C)} K_\sigma(\mathrm{x}-y) |I(y) - f_1(\mathrm{x})|^2 \, dy \\ + \lambda_2 \int_{out(C)} K_\sigma(\mathrm{x}-y) |I(y) - f_2(\mathrm{x})|^2 \, dy \end{aligned} \qquad (3.24)$$

where λ_1, λ_2 are positive coefficients, $f_1(\mathrm{x}), f_2(\mathrm{x})$ are functions that are used to fit intensity values near the point x. *K* is a Gaussian kernel function with a positive variance $(\sigma > 0)$. The values of $f_1(\mathrm{x})$ and $f_2(\mathrm{x})$, which vary with each point x, used to fit intensity values near each x. This is provided by the Gaussian function $K_\sigma(\mathrm{x}-y)$ that gets larger values at *y*, which is near the point x. The function *K* decreases when the point *y* goes away from the point x. Object boundaries are found by minimizing the equation (3.24) for all points *x* on the image domain Ω. This is performed with the minimization of the integral of E_{x}^{LBF} for each point x in Ω. Therefore, the following energy function is used;

$$E(C, f_1(\mathrm{x}), f_2(\mathrm{x})) = \int E_{\mathrm{x}}^{LBF}(C, f_1(\mathrm{x}), f_2(\mathrm{x}))d\mathrm{x} + \nu|C| \tag{3.25}$$

Level set formulation of the energy function in (3.24) is,

$$\begin{aligned} E_{\mathrm{x}}^{LBF}(\phi, f_1(\mathrm{x}), f_2(\mathrm{x})) = {} & \lambda_1 \int K_\sigma(\mathrm{x}-y)\left|I(y) - f_1(\mathrm{x})\right|^2 H(\phi(y))dy \\ & + \lambda_2 \int K_\sigma(\mathrm{x}-y)\left|I(y) - f_2(\mathrm{x})\right|^2 \left(1 - H(\phi(y))\right)dy \end{aligned} \tag{3.26}$$

Here, *H* is the Heaviside function. Then, the level set equation of the energy *E* is equation (3.25) is written as,

$$\begin{aligned} E_{\mathrm{x}}^{LBF}(\phi, f_1, f_2) &= \int_\Omega E_{\mathrm{x}}^{LBF}(\phi, f_1(\mathrm{x}), f_2(\mathrm{x}))d\mathrm{x} \\ &= \lambda_1 \int \left[\int K_\sigma(\mathrm{x}-y)\left|I(y) - f_1(\mathrm{x})\right|^2 H(\phi(y))dy \right] d\mathrm{x} \\ &\quad + \lambda_2 \int \left[\int K_\sigma(\mathrm{x}-y)\left|I(y) - f_2(\mathrm{x})\right|^2 \left(1 - H(\phi(y))\right)dy \right] d\mathrm{x} \end{aligned} \tag{3.27}$$

To keep the LSF as a signed distance function, the following regularization term,

$$P(\phi) = \int_\Omega \tfrac{1}{2}\left(\left|\nabla\phi(\mathrm{x})\right| - 1\right)^2 d\mathrm{x} \tag{3.28}$$

and also the length of the active contour, which is written as,

$$L(\phi) = \int_\Omega \delta(\phi(\mathrm{x}))\left|\nabla\phi(\mathrm{x})\right| d\mathrm{x} \tag{3.29}$$

are added to the level set equation given in (3.27). Therefore, the energy functional becomes

$$E(\phi, f_1, f_2) = E^{LBF}(\phi, f_1, f_2) + \mu P(\phi) + \nu L(\phi) \tag{3.30}$$

where, v and μ are positive coefficients. The gradient descent flow after minimization of the energy functional (3.30) by keeping f_1 and f_2 as fixed is obtained as,

$$\frac{\partial \phi}{\partial t} = -\delta_\varepsilon(\phi)\left(\lambda_1 \int_\Omega K_\sigma(y-\mathrm{x})\left|I(\mathrm{x})-f_1(y)\right|^2 dy - \lambda_2 \int_\Omega K_\sigma(y-\mathrm{x})\left|I(\mathrm{x})-f_2(y)\right|^2 dy\right) + v\delta_\varepsilon(\phi) div\left(\frac{\nabla\phi}{|\nabla\phi|}\right) + \mu\left(\Delta\phi - div\left(\frac{\nabla\phi}{|\nabla\phi|}\right)\right) \tag{3.31}$$

where λ_1 and λ_2 are positive constant values, $K_\sigma(u)$ is a Gaussian kernel function that decreases and approaches to zero with the scaling parameter σ. The Dirac delta function $\delta_\varepsilon(\phi)$ can be obtained by,

$$\delta_\varepsilon(\phi) = H'_\varepsilon(x) = \frac{1}{\pi}\frac{\varepsilon}{\varepsilon^2 + x^2} \tag{3.32}$$

were ε is chosen as 1. The functions in (3.31), f_1 and f_2, which give weighted averages of the intensities inside and outside the active contour, are defined as,

$$f_1(\mathrm{x}) = \frac{K_\sigma(\mathrm{x}) * \left[H_\varepsilon(\phi) I(\mathrm{x})\right]}{K_\sigma(\mathrm{x}) * H_\varepsilon(\phi)} \qquad f_2(\mathrm{x}) = \frac{K_\sigma(\mathrm{x}) * \left[\left(1-H_\varepsilon(\phi)\right) I(\mathrm{x})\right]}{K_\sigma(\mathrm{x}) * \left(1-H_\varepsilon(\phi)\right)} \tag{3.33}$$

In (3.31), the first and second term, which are data fitting and arc length term, are responsible for evolving of the active contour to the desired edges of the object. The third term is responsible for regularization of the LSF. The regularization term can be written as;

$$\Delta\phi - div\left(\frac{\nabla\phi}{|\nabla\phi|}\right) = div\left(\left(1-(1/|\nabla\phi|)\right)\nabla\phi\right) \tag{3.34}$$

that shows the diffusion rate $\left(1-(1/|\nabla\phi|)\right)$. When $|\nabla\phi| > 1$, the value of the rate is positive and the effect of the diffusion rate term is the usual diffusion, (which means that by making ϕ more even, we reduce the value of the gradient $|\nabla\phi|$) . The value of the gradient $|\nabla\phi|$ increases when the term has reverse effect. Stable evolution and accurate computation is achieved by the diffusion rate. The value of LSF ϕ grows to very large values on inside and outside of the zero level set. Therefore, the value of $\delta_\varepsilon(\phi)$ becomes arbitrarily small in the evolution equation (3.31). As the result of this, the motion of the active contour becomes slower and even it can be stopped before it

reaches boundaries. Also, the irregularities of the LSF cause the calculation to be inaccurate and inaccurate segmentation results.

The LBF method uses global and local information obtained from the image to solve intensity inhomogeneity problem. This method can give accurate segmentation results. However, it has very high computational cost because of the regularization and the punished term that corresponds to the second term. Also, when we change the location of the initial contour, we obtain different results. Therefore, this method is sensitive to the initialization, the coefficient of the length term (μ) and also the values of lambda parameters. The results shown in Figure 3.14 have been obtained with $\lambda_1 = 1,\ \lambda_2 = 2$ and by using the same original images given in Figure 3.12.a, Figure 3.12.e, Figure 3.12.i and initial contour given in Figure 3.12.b, Figure 3.12.f and Figure 3.12.j.

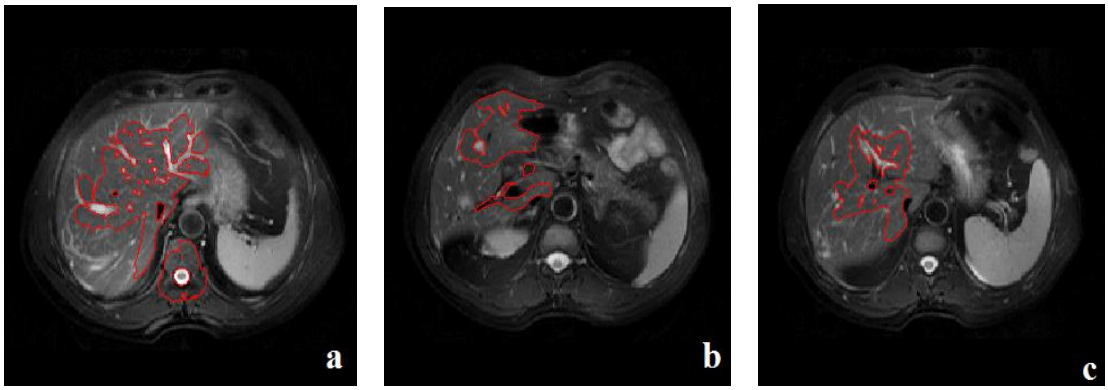

Figure 3.14. An example of segmented image with LBF method at maximum number of iteration and minimum energy level (a, b, c)

3.5.3.4. DRLSE and SPF Function Based LSM

Both local and global information should be used to obtain an accurate result of a liver segmentation method from SPIR images. Therefore, we have applied an edge based LSM by using the PDE (3.16) proposed in DRLSE, which includes a distance regularization term to solve the re-initialization problem, and a new SPF function (Xu and Yezzi 2000), to control the level set evolution by using the average values of the intensities both inside and outside of the active contour (Goceri et al 2012).

The re-initialization process is used to replace the degraded LSF with a signed distance function, which has the property that the gradient of the distance function is

equal to a unit vector. Because, the level set evolution causes irregularities and numerical errors which destroy this property and lead to unstable and incorrect evolution (Sethian 1999). The re-initialization is a serious problem since it is not clear how and when it should be applied to restore the degraded LSF as a signed distance function (Gomes and Faugeras 2000).

We have used the following SPF function to control the motion.

$$SPF(I(\mathrm{x})) = \frac{G_\sigma(\mathrm{x}) * I(\mathrm{x}) - (f_1 + f_2)/2}{\max\left(\left|G_\sigma(\mathrm{x}) * I(\mathrm{x}) - (f_1 + f_2)/2\right|\right)} \tag{3.35}$$

In (3.35), G_σ is the Gaussian kernel with a standard deviation σ. The functions f_1 and f_2 are weighted averages of the intensity values inside and outside the active contour respectively. These functions are given as defined in (Li et al 2007) by

$$f_1(\mathrm{x}) = \frac{G_\sigma(\mathrm{x}) * \left[H_\varepsilon(\phi) I(\mathrm{x})\right]}{G_\sigma(\mathrm{x}) * H_\varepsilon(\phi)} \qquad f_2(\mathrm{x}) = \frac{G_\sigma(\mathrm{x}) * \left[\left(1 - H_\varepsilon(\phi)\right) I(\mathrm{x})\right]}{G_\sigma(\mathrm{x}) * \left(1 - H_\varepsilon(\phi)\right)} \tag{3.36}$$

The PDE for the level set evolution is defined as

$$\frac{\partial \phi}{\partial t} = \mu div\left(\frac{p'\left(|\nabla\phi|\right)}{|\nabla\phi|}\nabla\phi\right) + \lambda\delta_\varepsilon(\phi) div\left(g\frac{\nabla\phi}{|\nabla\phi|}\right) + \alpha g \delta_\varepsilon(\phi) + SPF(I) \tag{3.37}$$

where g is the edge indcation function (3.6) and $p\left(|\nabla\phi|\right)$ is a potential function (3.10) that is used for the regularization term given by $R_p(\phi) = \int_\Omega p\left(|\nabla\phi|\right) d\mathrm{x}$ to obtain the general energy function (3.4) with the external energy term $E_{ext}(\phi)$.

It has been observed from experiments that accurate liver segmentation is not possible from all slices in a dataset with this method by using the same sigma parameter in the Gaussian function. Because abdominal SPIR images have low contrastness and also in-homogeny gray level values. Also, it is not clear how to chosen the sigma parameter.

Figure 3.15 shows example images obtained from DRLSE and SPF function based LSM by using the same initial contour and coefficients in the level set evolution equation (3.37) for each slice but with a different sigma parameter for the SPF function (3.35).

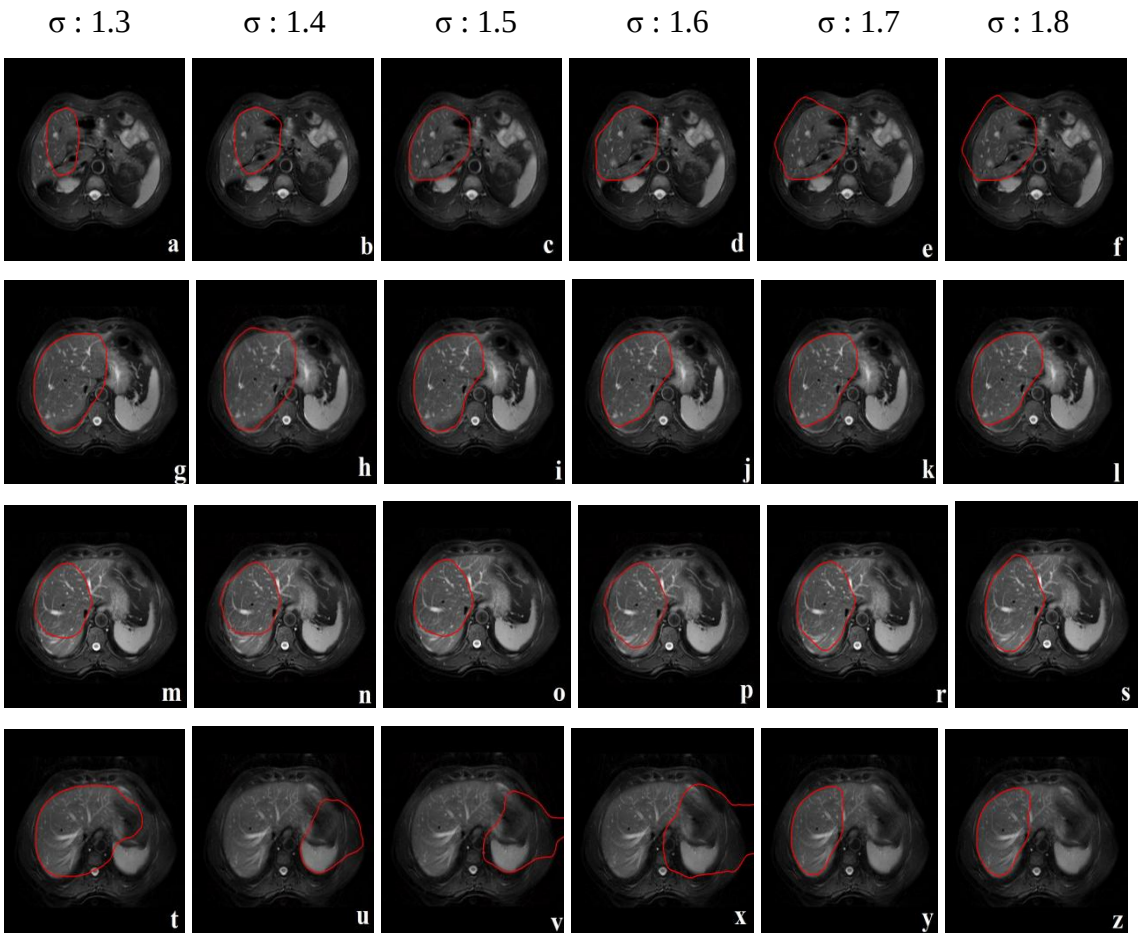

Figure 3.15. Example images obtained from the DRLSE and SPF function based method using the same initial contour and coefficients but with different sigma values

Another problem is related to the weight values for the length and area term in (3.37). To use constant weight values causes undesired results due to the vascular structure of liver and intensity inhomogenity. Therefore, we have proposed a LSM with a novel SPF function that is defined without Gaussian function. The proposed segmentation approach, which also uses adaptive weight values in energy function by computing geometric properties of the active contour, is presented in Chapter 4.

CHAPTER 4

PROPOSED VLSM FOR LIVER SEGMENTATION FROM MR IMAGES

There are two important difficulties of level set based image segmentation methods. One of them is that the evolution of the curve has to be stopped efficiently (without leakage or under segmentation) when it reaches to the desired boundaries. The other difficulty is due to the contradiction between the implementation and the theory of the LSM associated to the representation of LSFs by signed distance functions. Since LSMs do not implicitly preserve LSFs as signed distance functions in practice. Therefore, in conventional level set approaches, the LSF causes irregularities during evolution. These irregularities cause unstable evolution due to numerical errors.

The traditional solution to keep the LSF as a signed distance function is re-initialization. The degraded LSF is replaced with a signed distance function, which has the property that the gradient of the distance function is equal to a unit vector, in re-initialization process. However, re-initialization is a serious problem since it is not clear how and when it should be applied to restore the degraded LSF as a signed distance function (Gomes and Faugeras 2000).

Recently, VLSMs have been proposed (Li et al 2005, Xie X. 2010, Li et al. 2010) to regularize the LSF as a signed distance function and hence to avoid costly re-distancing (re-initialization) of the LSF. The main advantages of these methods are easier implementation and higher computational efficiency. The methods in (Bresson et al 2007, Chan et al 2006) combine the Chan-Vese model (Chan and Vese 2001) or the piecewise smoothing algorithm (Vese and Chan 2002) with variational model to avoid re-initialization. However, these methods in (Bresson et al 2007, Chan et al 2006) can only be used for LSFs which have a specific form. Another proposed VLSM (Li et al 2005) uses a penalty term which penalizes deviations of LSFs from signed distance functions. However, the penalty term leads the diffusion rate to be tend to infinity and causes undesirable effects, numerical errors in some circumstances. The function of the penalty term has been improved and the diffusion rate became a bounded constant in the DRLSE method to maintain the signed distance property (Li et al 2010). The distance

regularization term in this method is based on a potential function and forces the gradient magnitude of the LSF to one of its minimum points. The distance regularization eliminates the re-initialization process. However, this method uses constant coefficients and the traditional edge stopping function that is based on Gaussian filter to remove the effect of noise in the energy formulation. The Gaussian filter causes blurred edges while reducing the image noise. Also, this method is very sensitive to position, shape and size of the initial contour on SPIR images. Therefore, it has been observed as shown in Figure 3.12 and Figure 3.15 that this model causes unstable evolution and can not segment liver from SPIR datasets successfully.

In this chapter, we propose liver segmentation from SPIR images by using a novel VLSM. The advantages of the proposed approach are as follows.

Pre-processing is performed to suppress the intensity effect of irrelevant organs (i.e. heart, spleen, kidney and gallbladder) during the curve evolution process and increase liver segmentation performance.

The applied energy functional is composed of length and area of the closed curve. All VLSMs based on length and area terms use constant weight values for these terms. However, it is not clear how to choose the optimal constant value for different images in a dataset. Also, results of a segmentation method are sensitive to chosen weight parameters in VLSMs and different intensity gray levels of an image require different weight values. Therefore, we have computed these parameters automatically by using properties of the curve during the evolution for each slice.

The traditional edge stopping function, which is the absolute of the gradient of the convolved image with the Gaussian function, in LSMs is not robust and sensitive to noise. Therefore, it causes unstable evolution for liver segmentation from SPIR datasets. In our study, we propose to use an SPF function instead of the edge indicator function to overcome this problem. In our work, a novel SPF function, which is defined as partitioned according to the contrastness of the image, can control the direction of the motion and stops the curve evolution effectively.

Initial contours can be propagated to outside or inside. The position of initial contours is a key challenge for level set based segmentation methods (Weeratunga and Kamath 2004). Each user can draw different initial contours at different locations and size. Also, to find the correct number of iterations to stop the evolution for each initial contour is not easy. The segmentation results are not robust even optimal iteration numbers are given due to initial contours defined by users**.** Our proposed method by

using SPF function is not sensitive to the location, size and number of initial contour and stops the curve evolution efficiently at the minimum energy level even the iteration process does not reach the final iteration number.

The proposed approach in this chapter regularizes the LSF with Gaussian filtering after penalizing it to be binary (Zhang et al 2010). The re-initialization process both increases the segmentation performance and also it is computationally more efficient than applying the potential function (3.10) used in DRLSE method.

Also, the proposed method can be implemented with finite difference scheme.

The results of the proposed liver segmentation method have been evaluated according to sensitivity, specificity, accuracy and computational cost values.

The proposed approach for liver segmentation is presented in the following sections.

4.1. Preprocessing

The first step is preprocessing that removes kidney, spleen, heart and gallbladder from abdominal images by using anatomical information and morphological operations.

4.1.1. Kidney extraction

4.1.1.1. Literature Review for Kidney Segmentation

Kidney segmentation is a challenging task in MRI datasets because of the partial volume problem, intensity inhomogeneity, leakage of contrast agent to adjacent organs, high signal to noise rate, more artifacts and a low gradient response.

Figure 4.1 show example SPIR slices that include kidneys. The kidneys in Figure 4.1.a, in which the slice is generally the middle of the image sequence, are identified easily and seemed clearer so that the separation of them from other adjacent organs is easier. However, kidney detection and segmentation is difficult from the image shown in Figure 4.1.b due to the visualization difficulties caused by movements and breathing during the scanning. Also, the intensity similarities and unclear boundaries between the adjacent organs and kidneys make the kidney segmentation more difficult.

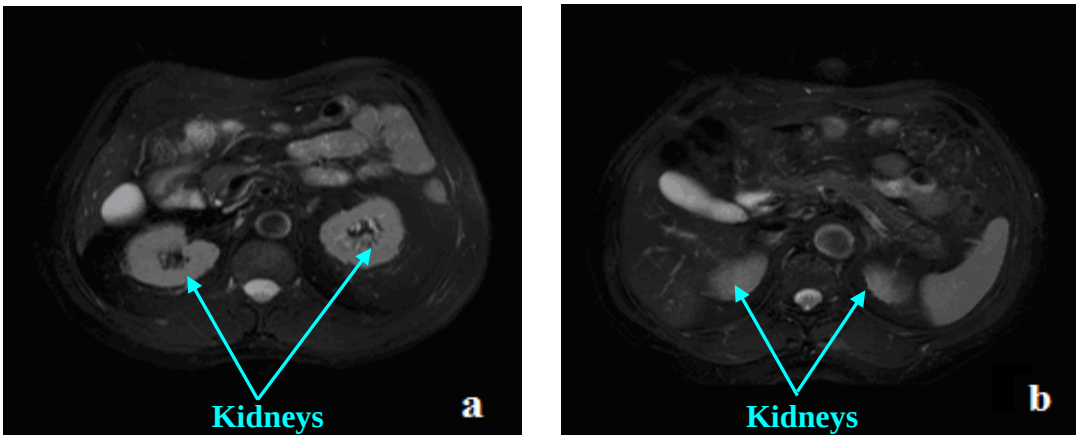

Figure 4.1. An example image where the border is very clear (a), and another image where the border between the right kidney and the liver is not clear (b)

In the literature, kidney segmentation methods using CT images can be classified into four main groups. The first group of kidney segmentation methods is knowledge based methods. M. Brown et al. have proposed to use parametric features of anatomical structures to guide labeling of regions on the image and kidney segmentation (Brown et al.2001). Kobashi and Shapiro have applied a knowledge based identification using the CT image properties and anatomical information in (Kobashi and Shapiro 1995). The second group of kidney segmentation methods is region growing based methods, which are mostly used by combining with other techniques. For example, Yang and Wang have proposed a connected component labeling by using intensity values to find estimated kidney location and to use a region growing method with mathematical morphology to extract kidneys (Yan and Wang 2010). D. T. Lim et al. have obtained the left and right kidney regions coarsely as ROIs, applied an adaptive region growing using initial seed points and a threshold value and then they have done region modification for accurate segmentation (Lin et al.2003). Pohle and Tönnies have proposed a region growing method that automatically optimizes the homogeneity criterion using the characteristics of the area to be segmented (Pohle and Toennies 2001a, 2001b, 2001c). Yan and Wang have developed another region growing method by estimating kidney position, using labeling algorithm and obtaining seeds with mathematical morphology to extract the kidney regions (Yan and Wang 2010). The third group is shape based approaches that are generally with active contours. M. Spiegel et al. have proposed a non-rigid registration based active shape model for

kidney segmentation (Spiegel et al. 2009). Huang et al have developed a shape based LSM by applying the Chen-Vese LSM with a connected component analysis to get separated components and then they have used the size feature to find the kidneys (Huang et al. 2009). Finally, the fourth group of methods for kidney segmentation is deformable model based approaches. Tsagaan and Shimizu have proposed a B-spline based deformable model by incorporating mean and variation of the organ into the objective function in order to fit the model (Tsagaan et al. 2001, 2002).

The methods proposed for kidney segmentation from CT images do not solve the intensity inhomogeneity problem that usually occurs in MRIs. When we search in the literature for kidney segmentation methods using MRIs, we see that a shape aided kidney extraction method by matching a co-focus elliptical model to a binary mask using optimization in the parametric space has been proposed in MR urography by Tang et al. (Tang et al.2009). H. Abdelmunim et al. have proposed another shape based approach (Abdelmunim et al.2008) on Dynamic Contrast Enhanced Magnetic Resonance Images (DCE-MRI). The authors obtain a mean shape model for kidneys by using extracted kidney shapes and perform registration of an intensity model, which is computed from test images, with the mean shape model. Although this approach seems successful, the accuracy of the result depends on the estimated model shapes by using the training datasets.

Gray level values of the liver that is the adjacent organ of the right kidney are very similar. This similarity and noises reduces the performance of the thresholding methods. Gradient based approaches are vulnerable for weak edges. The anatomical structures of the kidneys in different image slices are different and their shapes can vary for each patient. Therefore, the shape based kidney segmentation may not always be sufficient. Although the method in (Spiegel et al.2009) seems to be effective, the training of active shape models is required to model the expected shape. Therefore, the results obtained from this method depend on the training datasets.

4.1.1.2. Proposed Kidney Segmentation Method

In our work, we have performed kidney segmentation from abdominal SPIR images by a deterministic approach. We have used K-means clustering method and anatomical information to find kidney position. Kidney extraction has been applied to

slices that are from the first two-thirds (i.e. 2/3) of the dataset in our work. Because slices from the last one-third of the dataset do not include kidneys.

It has been observed that the kidney regions are always clustered together with the spine and the bright parts of other organs into the bright cluster when an image is clustered into three clusters (background, dark gray tissues and bright gray tissues) with the K-means clustering (Figure 4.2.a). Therefore, we have used prior anatomic knowledge to find kidney locations. Kidneys are inside the ribs and located in the bottom-left and bottom-right side of abdominal images. After the detection of the image boundaries, the horizontal and vertical axis lengths have been calculated and then the spine has been used as a landmark to find kidney positions (Figure 4.2.b). To identify the right kidney, a seed region, which includes some part of the kidney, has been selected at the right hand side of the spine after the detection of the spine position. Then, binary morphological image reconstruction has been applied by using the clustered image as the mask and the selected seed region as the marker (Figure 4.2.c). The output of this process gives us the segmented right kidney (Figure 4.2.d).

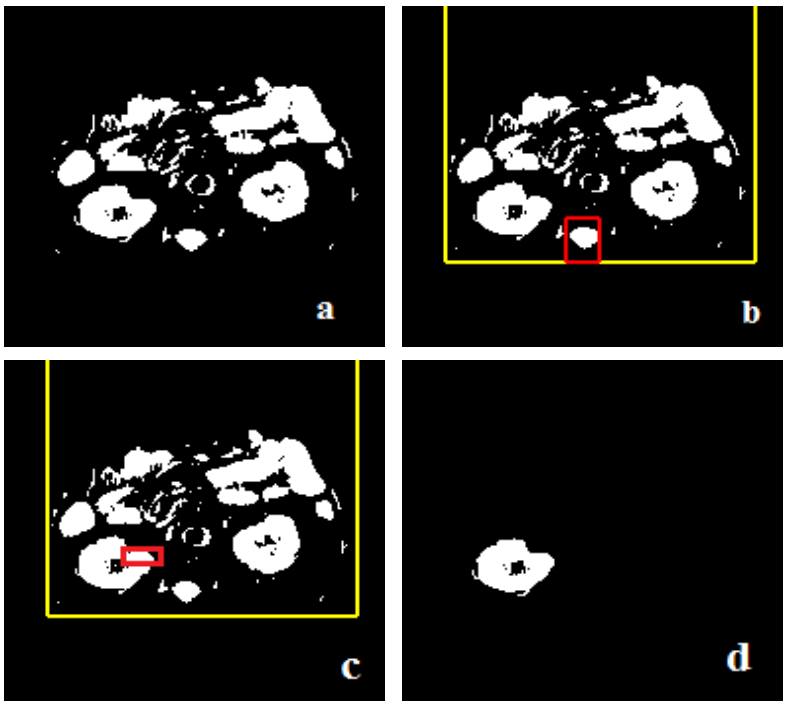

Figure 4.2. Clustered image (mask) of the original slice shown in Figure 4.1.a (a); Spine detection (b); Seed region (marker) in the red frame for image reconstruction (c); Segmented right kidney that is obtained after binary morphological image reconstruction (d)

The size of liver becomes smaller and it is positioned at the right side of the spine (at the top of the right kidney) while the kidneys appear in each succeeding slice in an MRI sequence. The right kidney is an adjacent organ to the liver and to find its location at the bottom-right side is easy. Therefore we have extracted it by using marker and mask images. However, segmentation of the left kidney with this way is difficult due to the spleen, which appears at the bottom-left side while kidneys disappear (Figure 4.1.b). Therefore, spleen segmentation has been applied before the extraction of the left kidney with the same algorithm.

4.1.2. Spleen Extraction

Spleen is located at the bottom-left side of abdominal images and in the third cluster when we clustered the original image into four clusters, which are background region, dark gray tissues, bright gray tissues and brightest tissues, with K-means algorithm.

Spleen segmentation has been performed similarly to the kidney segmentation algorithm by selecting a seed region on the spleen instead of the kidney in this case. The lines at the left and right hand side of the original image have been obtained after the first non-zero values are detected both from bottom to top and from left to right. The spine position has been found, which is in the middle of the distance between the lines at the left and right hand side (Figure 4.3.a, e, i and Figure 4.3.m). It is easy to find the spleen location from the image that shows bright gray tissues (Figure 4.3.b, f, j and Figure 4.3.n) after detection of the spine position. Another line, which is shown with red color in Figure 4.3.c, Figure 4.3.g, Figure 4.3.k and Figure 4.3.o, has been drawn at the middle of the vertical lines. A seed region that includes some part of the spleen has been selected by using the middle point of the red line at the left side of the spine. The seed region (pixels in the green rectangular frame in Figure 4.3.c, g, k and Figure 4.3.o) has been used as a marker image and the clustered image (Figure 4.3.b, f, j and Figure 4.3.n) has been used as a mask. Then, the segmented spleen image (Figure 4.3.d, h, l and Figure 4.3.p) has been obtained by applying binary morphological image reconstruction with the mask and marker images.

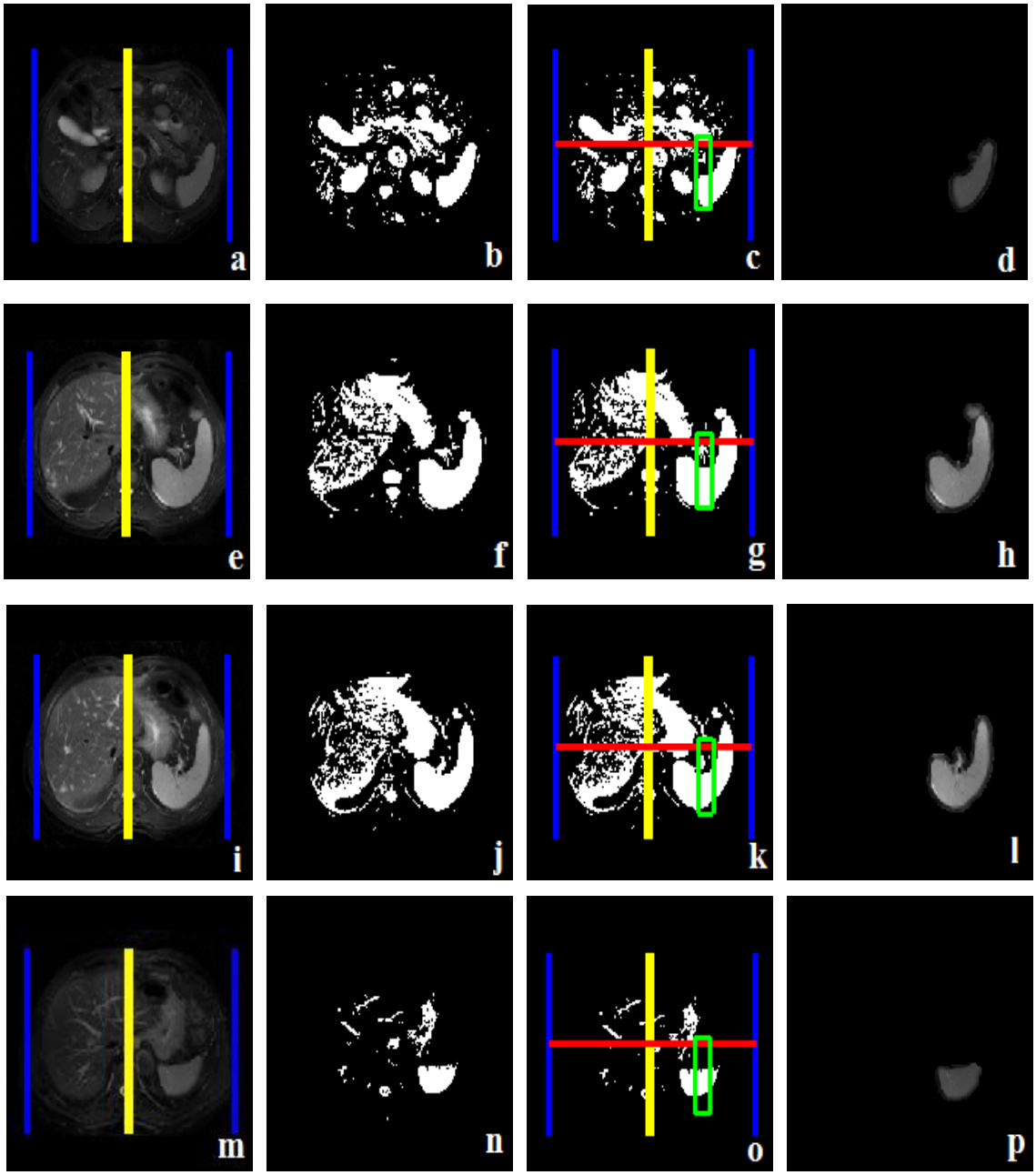

Figure 4.3. Spleen extraction: Boundaries of the image shown as blue lines and the middle of the distance between blue lines (shown as the yellow line) (a,e,i,m); Clustered image (b, f, j, n); Spleen detection (c,g, k, o); Segmented spleen images (d,h,l,p)

4.1.3. Heart Extraction

Heart is an adjacent organ to the liver and affects liver segmentation due to their gray level similarities and the weak edges between the liver and its adjacent organs.

Therefore, suppression of effects of the heart during curve evolution has been performed by removing this organ at the preprocessing stage.

Heart is always clustered in same cluster with spleen. Therefore, original image (Figure 4.4.a, f, k and Figure 4.4.p) is thresholded after spleen extraction by using the same threshold value that is obtained with the K-means clustering for spleen segmentation in the previous step. The clustered image (Figure 4.4.b, g, l and Figure 4.4.r) is used to detect heart location. Heart is positioned at the left hand side of the spine and up side of the spleen. A seed region has been selected by using the middle point of the red and yellow lines to the left side of the spine as shown in Figure 4.4.c, h, m and Figure 4.4.s. To obtain the necessary mask image, the original image after spleen extraction has been clustered into four clusters. The last cluster that includes heart is chosen and used as the mask image. Mask and marker images, which have been used to apply binary morphological image reconstruction, are shown in Figure 4.4.d, i, n and Figure 4.4.t for different slices. The images without heart and spleen are presented in Figure 4.4.e, j, o and Figure 4.4.u.

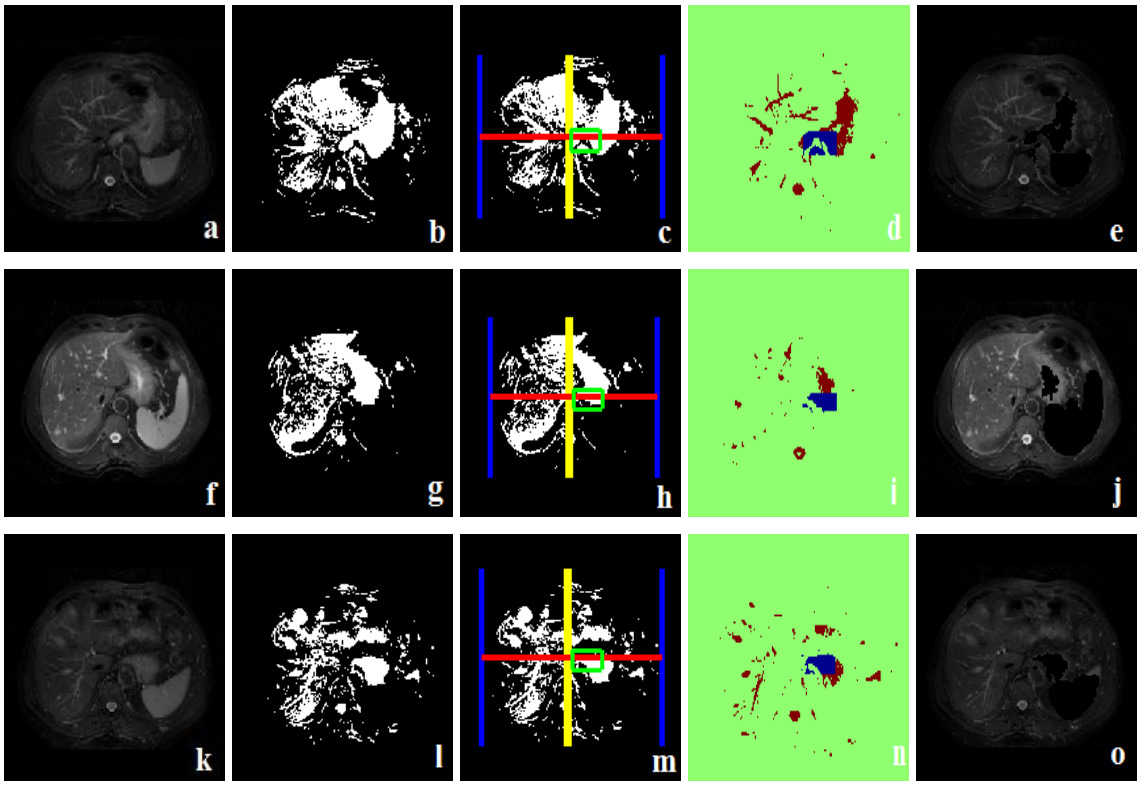

Figure 4.4. Original images (a, f, k, p); Clustered images without spleen (b, g, l, r); Heart detection (c, h, m, s); Marker (d, i, n, t); Image without heart and spleen (e, j, o, u)

(cont. on next page)

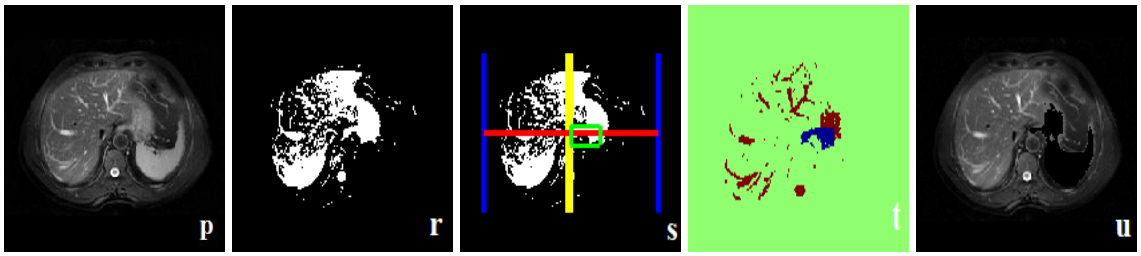

Figure 4.4. (cont.)

Figure 4.5 shows that if the heart does not exist in the original image then there will not be any pixel in the selected seed region. Therefore, the heart extraction will not be applied.

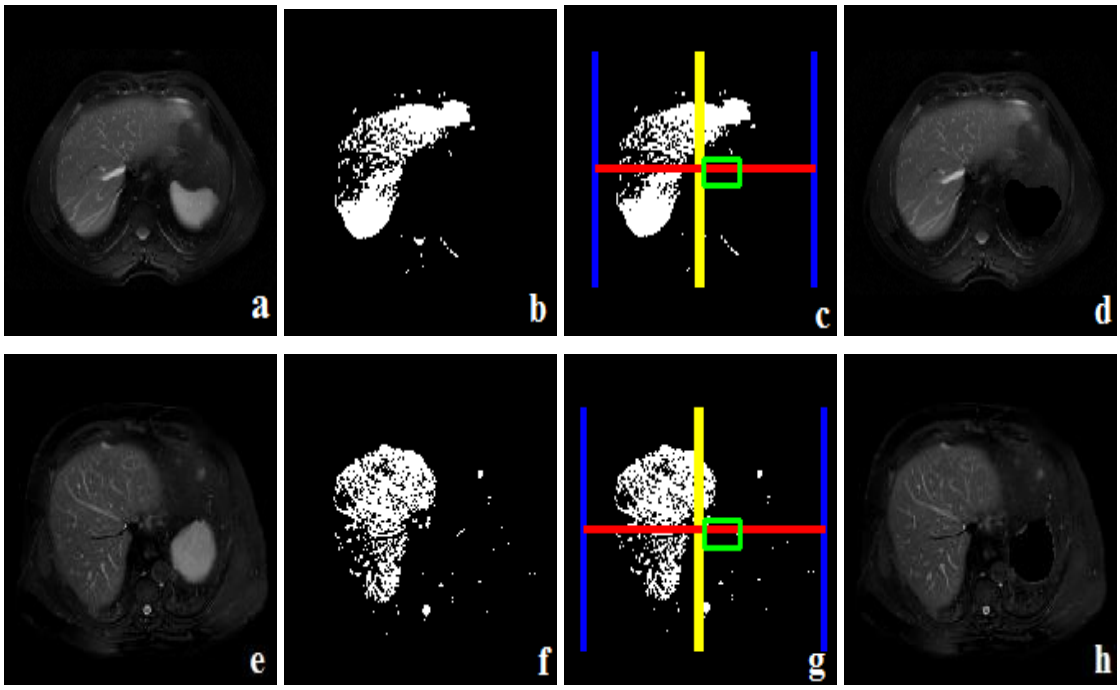

Figure 4.5. Original image (a, e); Clustered image without spleen (b, f); Heart detection (c, g); Preprocessed image (d, h)

4.1.4. Gallbladder Extraction

Gallbladders may have different shape, size and positions in a human body. They may not seem at each dataset. However, they are adjacent organs (Figure 4.6.a) to the liver and affect the liver segmentation, if they exist in an abdominal SPIR dataset. Therefore, gallbladders have been extracted in the preprocessing stage.

A gallbladder is in the brightest cluster that has been obtained at the spleen extraction step by K-means clustering. Therefore, the gallbladder has been extracted

from the image after kidney, heart and spleen extraction (Figure 4.6.b). Then, the preprocessed image (Figure 4.6.c) has been used for liver segmentation.

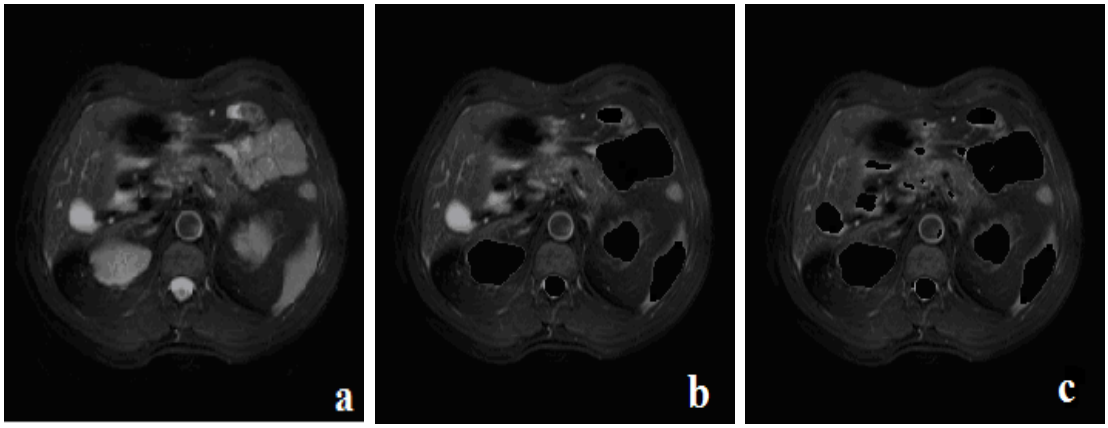

Figure 4.6. Original slice that includes the gallbladder (a); Image before the gallbladder extraction (b); Image without gallbladder, kidney, heart and spleen (c)

4.2. Liver Segmentation

4.2.1. Energy Formulation

We have used the following energy function that consists of the length, $L_g(\phi)$, and area, $A_g(\phi)$, terms with coefficients expressed as,

$$E(\phi) = \lambda L_g(\phi) + \alpha A_g(\phi) \tag{4.1}$$

In (4.1), λ and α are the weight values ($\alpha \in \Re$, $\lambda > 0$), g is the edge stopping function, which is going to be replaced by the proposed SPF function in Section 4.2.3. The length term $L_g(\phi)$ (3.7) is used to compute the length of the active contour and the area term $A_g(\phi)$ (3.8) is used to compute the area in the active contour.

4.2.2. Adaptive Weight Values

All VLSMs based on the length and area terms use constant weight values for these terms (Prakash et al. 2012, Yang et al. 2012, Li et al. 2010, Li et al. 2005). The weight values are chosen according to the experience of authors. However, each data set has different contrast ratios and livers are not properly shaped organs. Further, liver has a vascular

structure and non-uniform intensity values. Therefore, using constant weight values for each data set and even for each slice will not give acceptable results for liver segmentation from SPIR image datasets. However, choosing the optimal weight values for different images and slices according to the experiences are not an easy task. Therefore, in this work, we have proposed adaptive weight values for the length and area terms in the energy function (4.1).

4.2.2.1. Proposed Approach to Compute the Alpha Parameter

The coefficient α for the area term $A_g(\phi)$ increases or decreases the effect of this term in the energy functional. This affects velocity of the evolving curve. If the value of α is big then the motion of the curve is fast, which may cause over-segmentation. If the value of α is small then the motion of the curve is slow and even curve evolution may stop before arriving to desired liver boundaries in this case.

Curvature is an intrinsic property of curves and affects the velocity (Sethian 2001). The effects of the curvature have been investigated in (Mikula and Sevcovic 1999, Sethian 2001, Ning et al. 2006) and commonly it is known that sharp corners are developed during the curve evolution when curvature is zero. Construction of the normal vector at the sharp corner and continue the curve evolution is not clear since calculation of the derivative is not possible at the corner. Therefore, curve evolution with speed that depends on curvature has been applied in several works (McCoy 2009, Kong et al. 2009, Wu and Tai 2010, Joshi et al. 2012, Zhu et al. 2013).

A curve evolution, $C_t = \kappa \vec{N}$, under curvature (κ) flow along its normal direction ($\vec{N}$) is illustrated in Figure 4.7. Any simple smooth closed curve in R^2 that evolve by the curvature converges to a point in finite time (Grayson 1987). Minimum curvature allows the inward concave regions to grow outward, while suppressing the motion of the outward convex regions. Maximum curvature allows the outward regions to move inward while suppressing the motion of the inward concave regions (Malladi and Sethian 1996).

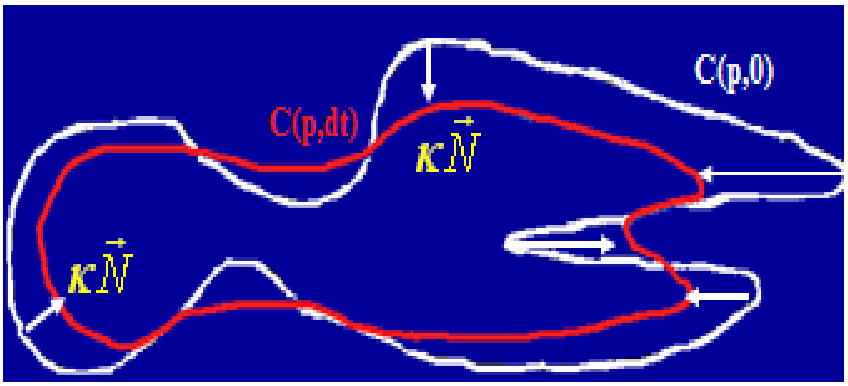

Figure 4.7. Curve evolution under curvature flow

Curve evolution can be inward or outward. The direction of the motion is determined by the sign of the alpha. We have defined the alpha parameter as summation of absolute values of minimum and maximum curvature terms to increase the speed of the motion at concave or convex regions. Therefore, the value of the alpha has been obtained automatically by using the equation written as,

$$\alpha = \left|\max(\kappa)\right| + \left|\min(\kappa)\right| \tag{4.2}$$

where κ is the curvature term, for each slice after each iteration. In our work, the LSF takes negative (positive) values inside (outside) the curve. Therefore, if the initial curve is located inside (outside) the liver then the sign of the alpha should be negative (positive).

4.2.2.2. Proposed Approach to Compute the Lambda Parameter

It has been observed that the proposed method is highly sensitive to α but it is not very sensitive to the chosen λ parameter for liver segmentation from abdominal SPIR data sets. However, to decide an optimal weight value without any idea about the range of it is not easy. Therefore, the value of λ, which is a positive coefficient of the length term $L(\phi)$ is calculated by

$$\lambda = \max\left(\frac{\partial L}{\partial \phi}\right)\sum\left(\frac{\partial L}{\partial \phi}\right) \tag{4.3}$$

in our implementation. Experiments on SPIR images show that the equation in (4.3) always gives efficient results for liver segmentation.

4.2.3. Proposed Edge Indicator with SPF Function

To use an edge indicator function provides level set evolution to stop at boundaries (Osher and Sethian 1988, Malladi et al 1995, Caselles et al 1997, Sapiro G. 2001, Li et al 2005, Li et al 2010). In these edge based LSMs, usually a positive, regular and decreasing edge stopping function is used. It is based on a convolution of an image with a Gaussian filter, such that $\lim_{t\to\infty} g(t) = 0$, which is given in (3.6). However, the traditional edge stopping function is never being zero for digital images since the discrete gradients are bounded. Therefore, active contour may pass through the boundaries and leakage problem may occur.

The traditional edge indicator function given in (3.6) uses the Gaussian kernel with σ. The LSF stops when the value of the edge indicator function approaches to zero. In other words, the contour will be halt where the gradient of the image is large enough for making $g \to 0$. However, we have observed that to use the traditional edge indicator function g is not appropriate for abdominal SPIR images (Figure 3.12). Since, the Gaussian filter can not preserve edge information while removing the noise effect. Therefore, it causes blurred image edges. To choose a small value of standard deviation may lead to sensitivity to noise. In this case, the curve evolution will not be stable. To choose a big value of standard deviation may cause boundary leakage problem, which results inaccurately segmented images. Therefore, determination of the optimal standard deviation is a dilemma for liver segmentation from SPIR datasets due to unclear boundaries and noise. This problem can be solved by using a different function instead of the traditional edge stopping function.

Many alternative solutions have been used in the literature instead of the traditional edge stopping function. For instance, the stopping term in C-V model (Chan and Vese 2001) is based on a result which is obtained from a segmentation method proposed by Mumford-Shah algorithm (Mumford and Shah 1989). This segmentation method uses intensity values from different region for energy minimization. Liu et al (Liu et al 2010) proposed an algorithm that uses the differences between estimated and actual probability densities of intensity values from different regions. We have observed that these methods are not successful for liver segmentation on SPIR images with low contrast and unclear boundaries. Some edge based LSMs proposed to use a balloon force to expand or shrink the active contour. However, to design the balloon force is not

easy since if the force is large then the contour passes over weak edges. The active contour might not pass through the narrow region of the object if the force is not large enough.

In our previous work, we have applied the DRLSE method with an SPF function to control the level set evolution (Goceri et al 2012). However, we have observed from the results (Figure 3.15) that this approach is still very sensitive to chosen sigma parameter of the Gaussian kernel used in (3.6). Therefore, in this work, we propose the following edge indicator instead of the conventional edge indication function in (3.6) by using a novel SPF function and its gradient to take into account edges for stable results as,

$$g = SPF(I(\mathrm{x})) + \nabla SPF(I(\mathrm{x})) \tag{4.4}$$

This approach with the adaptive weight values also solves the key challenge problem of edge based LSMs that is sensitivity to size, shape, location and number of the initial contour, which determines accuracy of segmentation results.

A partitioned and region based SPF function by using global information has been applied in this study. The proposed SPF function is defined according to the intensity values outside and inside the active contour as,

$$SPF(I(\mathrm{x})) = \begin{cases} \dfrac{I(\mathrm{x}) - (C_1 + C_2)/2}{\max\left(\left|I(\mathrm{x}) - (C_1 + C_2)/2\right|\right)}, & \text{if } \left(C_1 > 10 * C_2\right) \text{ or } \left(\max(I - avg) < 5 * avg\right) \\ \dfrac{I(\mathrm{x}) - \min(C_1, C_2)}{\max\left(\left|I(\mathrm{x}) - \min(C_1, C_2)\right|\right)}, & \text{else} \end{cases} \tag{4.5}$$

where C_1 and C_2 are average intensity values outside and inside the active contour respectively (3.21) and the term *avg* corresponds to $(C_1 + C_2)/2$. The SPF function means that if the average intensity value in the active contour is greater than ten times of the average intensity value of outside the contour (i.e. the average intensity values inside and outside the active contour are not close) or the difference between intensity values of each pixel and the mean intensity value of inside and outside average intensities is greater than the five times of the mean intensity value then select the first part otherwise, select the second part of its definition. Because, we always define the active contour inside the liver in our application. Therefore, if values of C_1 and C_2 are close when we use a preprocessed image then constrastness of the image is very low.

Then the difference between each pixel value and the minimum average intensity value is efficient for curve evolution. The proposed SPF based edge indication function gives effective results even at weak boundaries.

4.2.4. Initialization and Regularization of the LSF

Unlike traditional LSMs, which require initialization of LSF as a signed distance function that are computed by using a contour, the LSF in our implementation is initialized as a signed distance function. We initialize the LSF by using a region in the image. Initialization is performed with constant values that have opposite signs outside and inside the contour (Figure 4.8). Because, this kind of initial LSF becomes very close to a signed distance function with the distance between adjacent isocontours close to one (Li et al 2010, Li et al 2005).

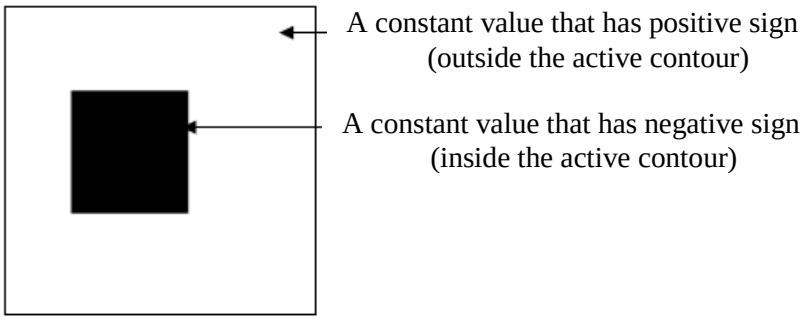

Figure 4.8. Initialization of the LSF

Therefore, if we assume that R_0 is a region in the image domain Ω, and ρ is a positive constant ($\rho > 0$) then the initial LSF is defined as,

$$\phi_0(x,y) = \begin{cases} -\rho, & \text{if } (x,y) \in R_0 \\ \rho, & \text{otherwise} \end{cases} \tag{4.6}$$

To prevent the LSF from being too flat or too steep near the zero level set, we have regularized the LSF by applying binarization (Figure 4.9.a) and Gaussian filtering, i.e. $\phi = \phi * G_\sigma$, (Figure 5.9.b) to the LSF after each iteration (Zhang et al 2010). Here, binarization refers to the assignment that if $\phi > 0$ then $\phi = 1$ otherwise, $\phi = -1$. Figure 4.9.b and Figure 4.9.c shows a regularized LSF.

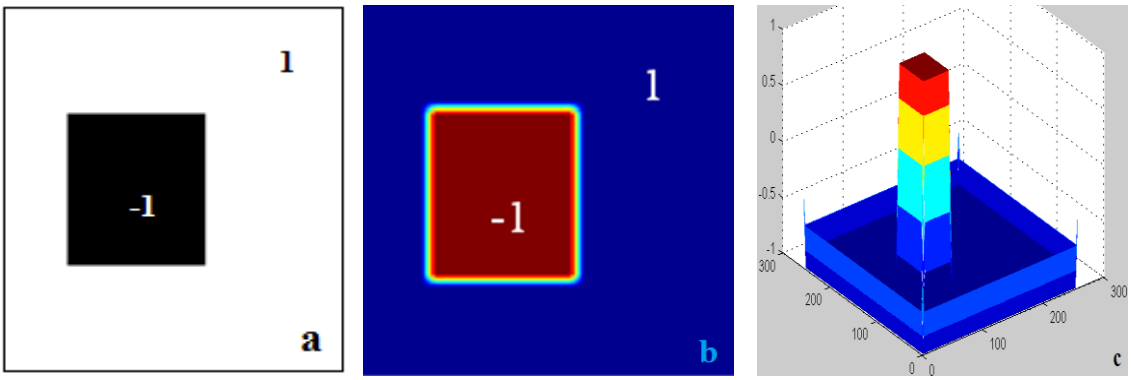

Figure 4.9. Binary LSF (a); LSF after Gaussian filtering operation (b); Different levels of the LSF (c)

Figure 4.10.a shows the updated LSF after the first iteration by using a pre-processed image. After binarization of the LSF (Figure 4.10.b), Gaussian filtering process gives the regularized LSF (Figure 4.10.c). Different levels of the LSF after the first iteration are shown in Figure 4.10.d.

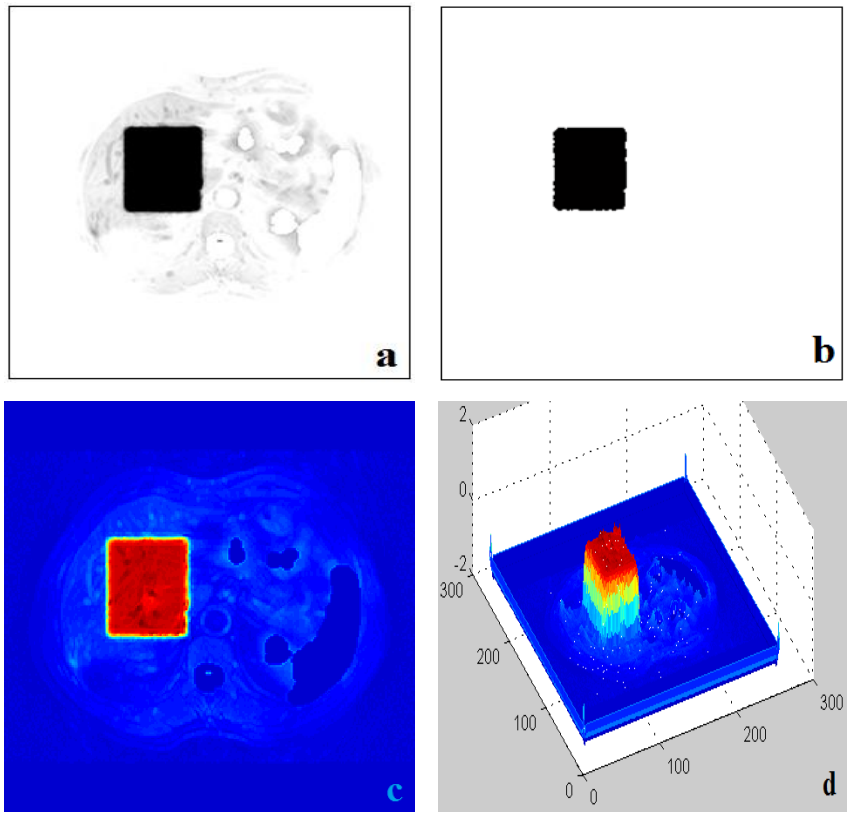

Figure 4.10. LSF after the first iteration (a) ; LSF after binarization (b); LSF after Gaussian filtering (c); Levels of the regularized LSF with different colours (d)

The curve evolution stops when the minimum energy value has been found. Figure 4.11.a and b shows the LSF that has reached the minimum energy on the image. Figure 4.11.c and d shows the LSF after the regularization steps.

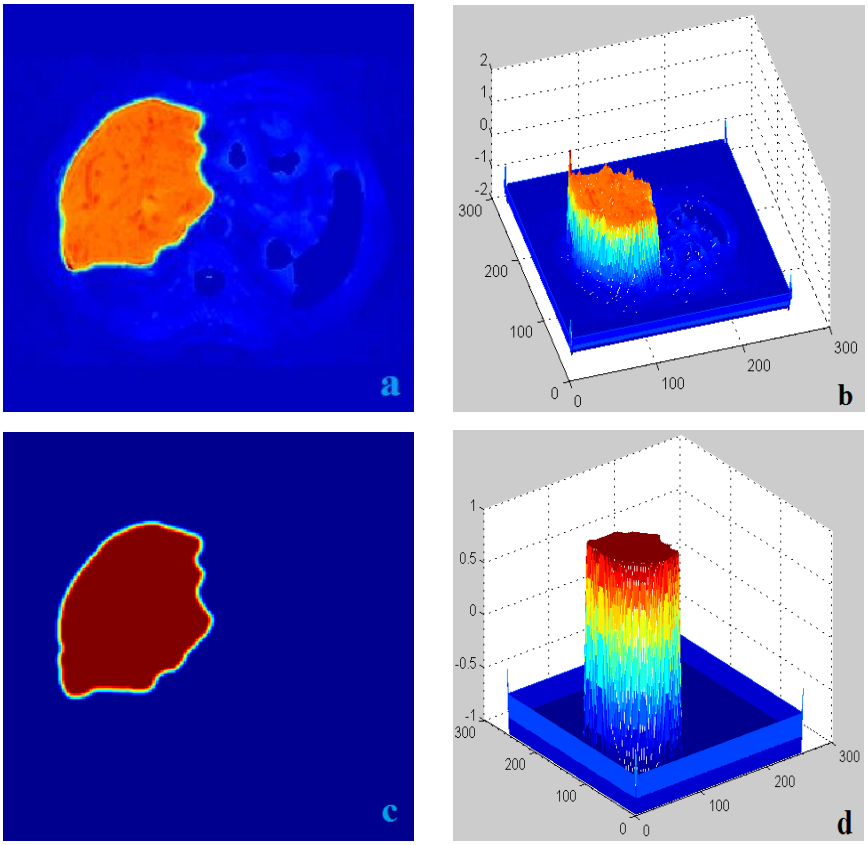

Figure 4.11. LSF at minimum energy (a); Different view of the LSF (b); LSF after regularization (c); Different view of the regularized LSF (d)

In our works, we have chosen the standard deviation parameter σ of the Gaussian function as 2. To obtain more smooth edges the value of the parameter can be increased. However, it should not be too small or too big to avoid sensitivity to noise or leakage problems. Also, we have truncated the Gaussian kernel to increase efficiency as a $M \times M$ mask and chosen the value of M as 5 for our datasets.

4.2.5. Gradient Descent Flow to Minimize Energy Function

As it is known, to obtain a minimum value of a function, a steady state solution of the gradient flow equation of this function can be found. The gradient flow equation

of the energy function is written as given in (4.11), which is an evolution equation of a time dependent LSF $\phi(x,y,t)$ with a spatial variable x and y. By substituting the area (3.8) and length (3.7) term to the energy function given in (4.1), we can write that

$$E(\phi) = \lambda \int_{\Omega} g\delta(\phi)\left|\nabla\phi\right| dxdy + \alpha \int_{\Omega} gH(-\phi)dxdy \tag{4.7}$$

The directional derivative of the equation in (4.7) is obtained as,

$$E'(\phi)\cdot h = \int_{\Omega}\left[-\lambda div(\tfrac{g\delta_{\varepsilon}(\phi)\nabla\phi}{|\nabla\phi|}) + \lambda g\delta'_{\varepsilon}(\phi)\left|\nabla\phi\right| - vg\delta_{\varepsilon}(\phi)\right]h \tag{4.8}$$

We can write from (4.8) after integration by parts that

$$E'(\phi)\cdot h = \int_{\Omega}\left[-\lambda div(\tfrac{g\delta_{\varepsilon}(\phi)\nabla\phi}{|\nabla\phi|}) + \lambda g\delta'_{\varepsilon}(\phi)\left|\nabla\phi\right| - vg\delta_{\varepsilon}(\phi)\right]h \tag{4.9}$$

Then, gradient of the energy function (4.7) is obtained as,

$$\nabla E(\phi) = -\lambda\delta_{\varepsilon}(\phi) div\left(g\frac{\nabla\phi}{\left|\nabla\phi\right|}\right) - \alpha g\delta_{\varepsilon}(\phi) \tag{4.10}$$

Therefore, the gradient flow of the energy formulation given in (4.1) is written as,

$$\frac{\partial\phi}{\partial t} = -\nabla E(\phi) = \lambda\delta_{\varepsilon}(\phi) div\left(g\frac{\nabla\phi}{\left|\nabla\phi\right|}\right) + \alpha g\delta_{\varepsilon}(\phi) \tag{4.11}$$

and the minimum value of the energy function (4.1) can be obtained by solving the equation given in (4.11).

4.2.6. Finite Difference Scheme

It is possible to implement the PDE (4.31) with a finite difference method by considering the 2-D case with a time dependent LSF $\phi(x,y,t)$. The spatial derivatives $\partial\phi/\partial x$, $\partial\phi/\partial y$ for this implementation are obtained by the central difference method (i.e. spatial derivatives are discretized by central difference method). We have chosen fixed steps as $\Delta x = \Delta y = 1$. Approximation of $\partial\phi/\partial t$ is performed by forward

difference schemes. The discrete form of the LSF can be represented with a temporal index k and spatial index (i,j) as $\phi_{i,j}^{k}$. Then the discretized LSF is written by using an approximation, $L\left(\phi_{i,j}^{k}\right)$, of the right hand side of the evolution equation. Therefore, we can write iteration process as

$$\phi_{i,j}^{k+1} = \phi_{i,j}^{k} + \Delta t L\left(\phi_{i,j}^{k}\right) \tag{4.12}$$

Figure 4.12 shows example images obtained by this method at maximum number of iterations (Figure 4.12.a and Figure 4.12.d) and at minimum level of the energy function (Figure 4.12.b and Figure 4.12.e). Also, the graphical representation of gradient of the energy function is presented in Figure 4.12.c and Figure 4.12.f.

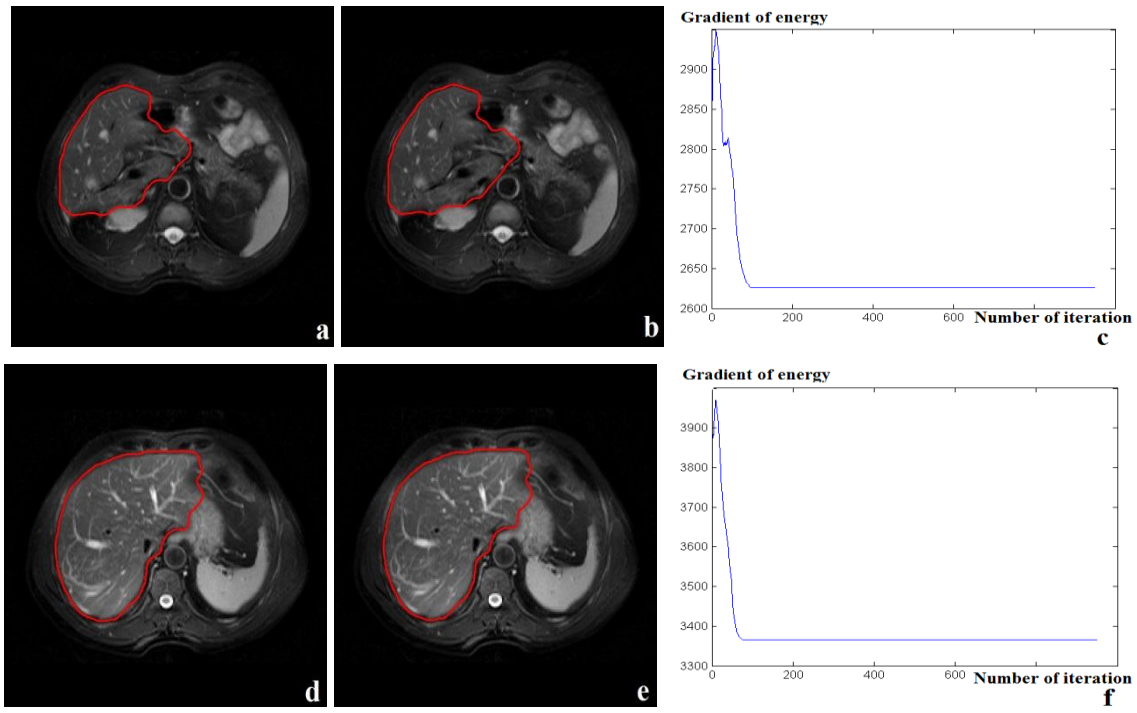

Figure 4.12. An example result of the automatic DRLSE and the new SPF function based LSM at maximum number of iterations (a, d) and at minimum level of the energy function (b, e); Graphical representation of the gradient of the energy function (c, f)

CHAPTER 5

EXPERIMENTAL RESULTS

This thesis involves seven different implementations for liver segmentation from SPIR scans. Experiments on original and preprocessed images showed that fitting the probability distribution of GMM to intensity histograms gives better results than the deterministic K-means method, which is affected by noise more than GMM. However, because of the similar gray level texture of the liver and adjacent organs such as spleen and heart, even though the used skeleton information from the previous slice, the results obtained from the GMM and K-means based segmentation methods are not correctly segmented liver images. It is not possible to obtain desired liver shapes from these results by applying the same post-processing operations for all slices.

The results of the supervised MLP based segmentation method without any pre-processing and post-processing step are not reasonable.

The integer operations based LSM (FTC method) is sensitive to user defined parameters that are iteration numbers and initial contours on each slice.

The method that uses DRLSE with an SPF function depends on chosen sigma parameters. Also, it is not possible to stop the evolution of the active contour at the desired liver boundaries by using the same sigma parameter for each dataset and even for each slice in a dataset (Figure 3.15).

The proposed LSM with a novel SPF function presents liver images that are always segmented more successfully than the GMM and K-means based method without applying any post-processing step. However, the results of the liver segmentation algorithm are not reasonable when we use original slices, which have kidneys and gallbladders. Therefore, we applied this method on pre-processed images. The proposed approach is always the fastest method and if the most accurate result is obtained from the FTC, MLP or DRLSE with SPF methods then the second most accurate result is obtained from the proposed method.

Figure 5.1 shows the results obtained by using the original slices given in Figure 5.1.a, 5.1.b and 5.1.c, in which kidneys do not seem, with the automatic GMM (Figure 5.1.d, 5.1.e and 5.1.f), automatic K-means (Figure 5.1.g, 5.1.h and 5.1.i), MLP (Figure

5.1.j, 5.1.k and 5.1.l), FTC method (Figure 5.1.m, 5.1.n and 5.1.o), FTC algorithm based automatic method (Figure 5.1.p, 5.1.r and 5.1.s), DRLSE with SPF function (Figure 5.1.t, 5.1.u and 5.1.v) and also the proposed liver segmentation method (Figure 5.1.x, 5.1.y and 5.1.z).

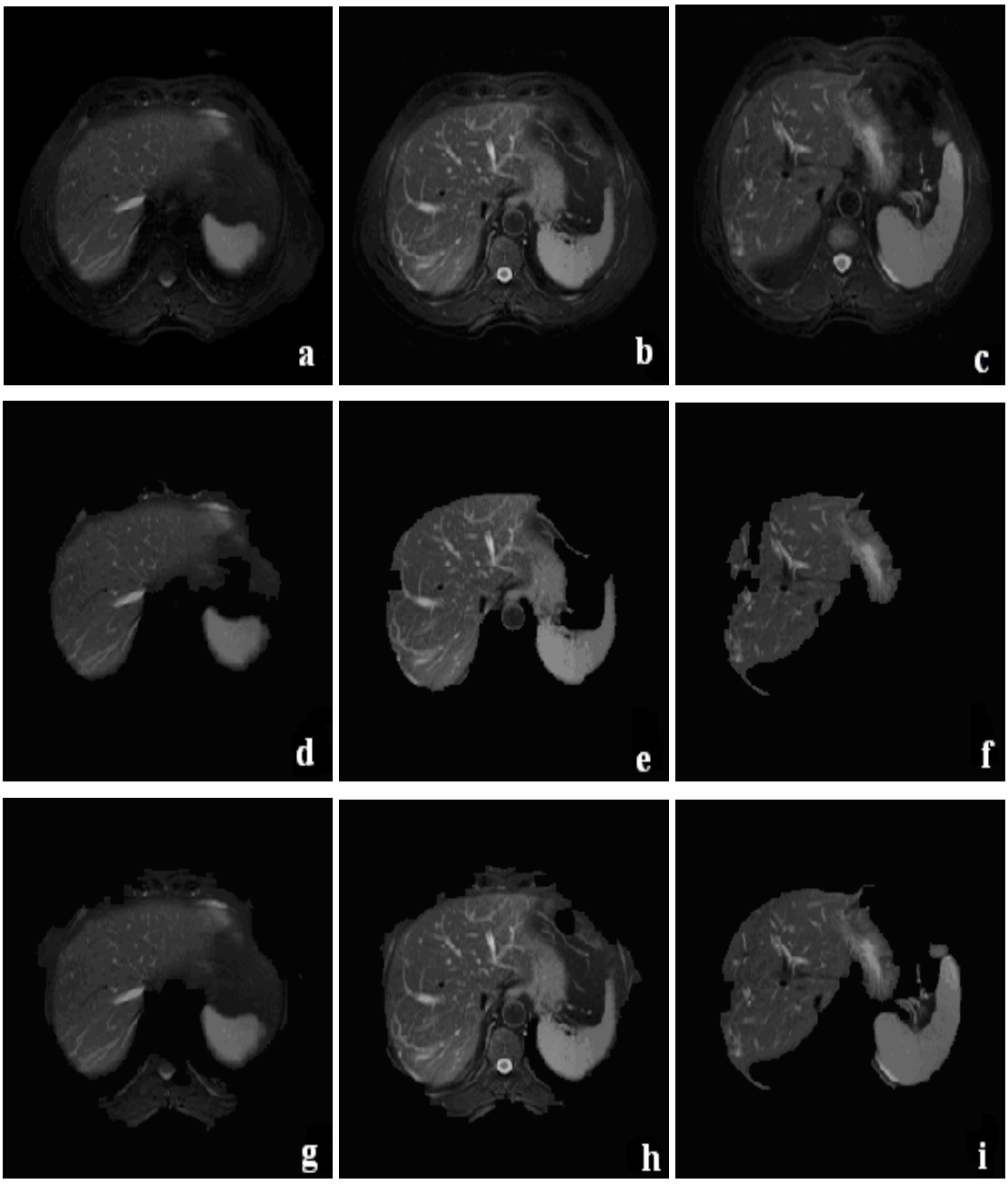

Figure 5.1. Original slices (a, b, c); Results of the automatic GMM (d, e, f); Automatic K-means (g, h, i); MLP (j, k, l); FTC method (m, n, o); Automatically applied FTC method (p, r, s); DRLSE with SPF function (t, u, v); The proposed liver segmentation method (x, y, z)

(cont. on next page)

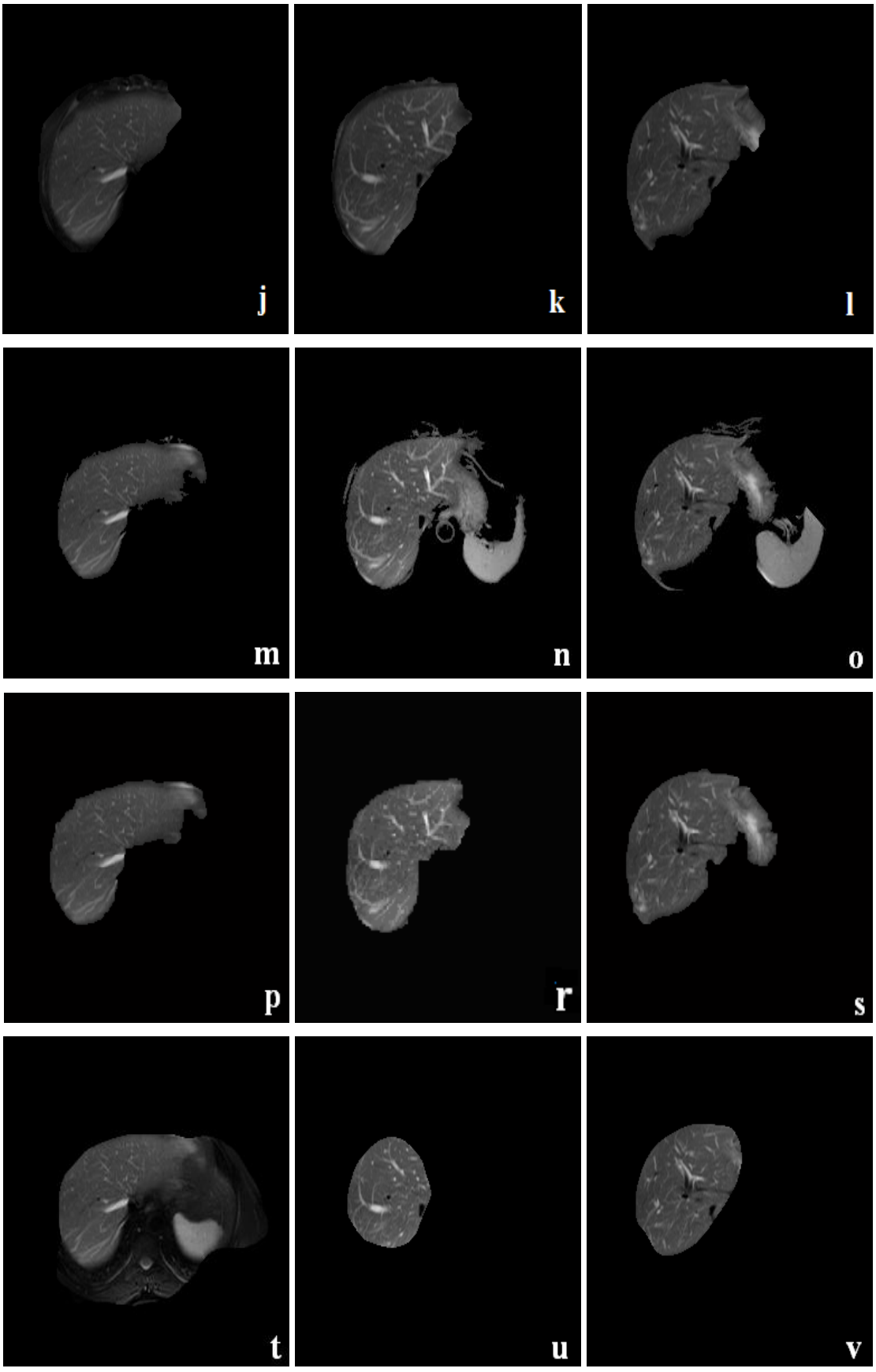

Figure 5.1. (cont.)

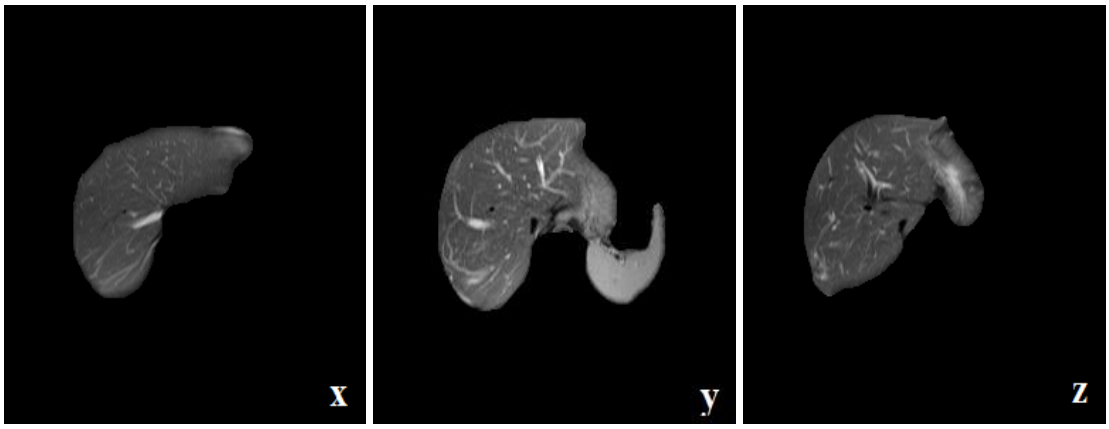

Figure 5.1. (cont.)

Figure 5.2.a, Figure 5.2.b and Figure 5.2.c show pre-processed images of the original slices shown in Figure 5.1.a, Figure 5.1.b and Figure 5.1.c. The liver segmentation results from these preprocessed images by using the automatic GMM (Figure 5.2.d, Figure 5.2.e and Figure 5.2.f), automatic K-means (Figure 5.2.g, Figure 5.2.h and Figure 5.2.i), MLP (Figure 5.2.j, Figure 5.2.k and Figure 5.2.l), FTC method (Figure 5.2.m, Figure 5.2.n and Figure 5.2.o), automatically applied FTC algorithm based method (Figure 5.2.p, Figure 5.2.r and Figure 5.2.s), DRLSE with SPF function (Figure 5.2.t, Figure 5.2.u and Figure 5.2.v) and also the proposed liver segmentation method (Figure 5.2.x, Figure 5.2.y and Figure 5.2.z) are shown in Figure 5.2. It is observed that the results are more efficient when we use pre-processed images instead of the original slices for liver segmentation.

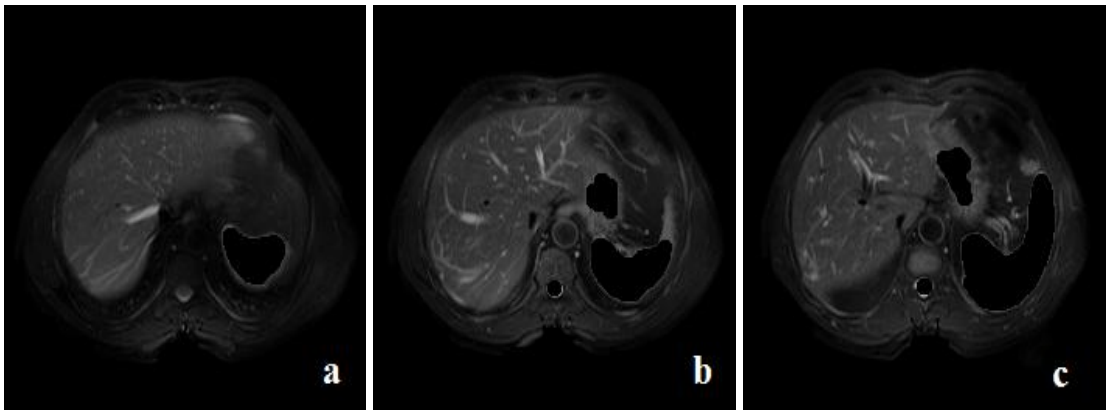

Figure 5.2. Pre-processed slices (a, b, c); Results of the automatic GMM (d, e, f); Automatic K-means (g, h, i); MLP (j, k, l); FTC method (m, n, o); Automatically applied FTC method (p, r, s); DRLSE with SPF function (t, u, v); The proposed liver segmentation method (x, y, z)

(cont. on next page)

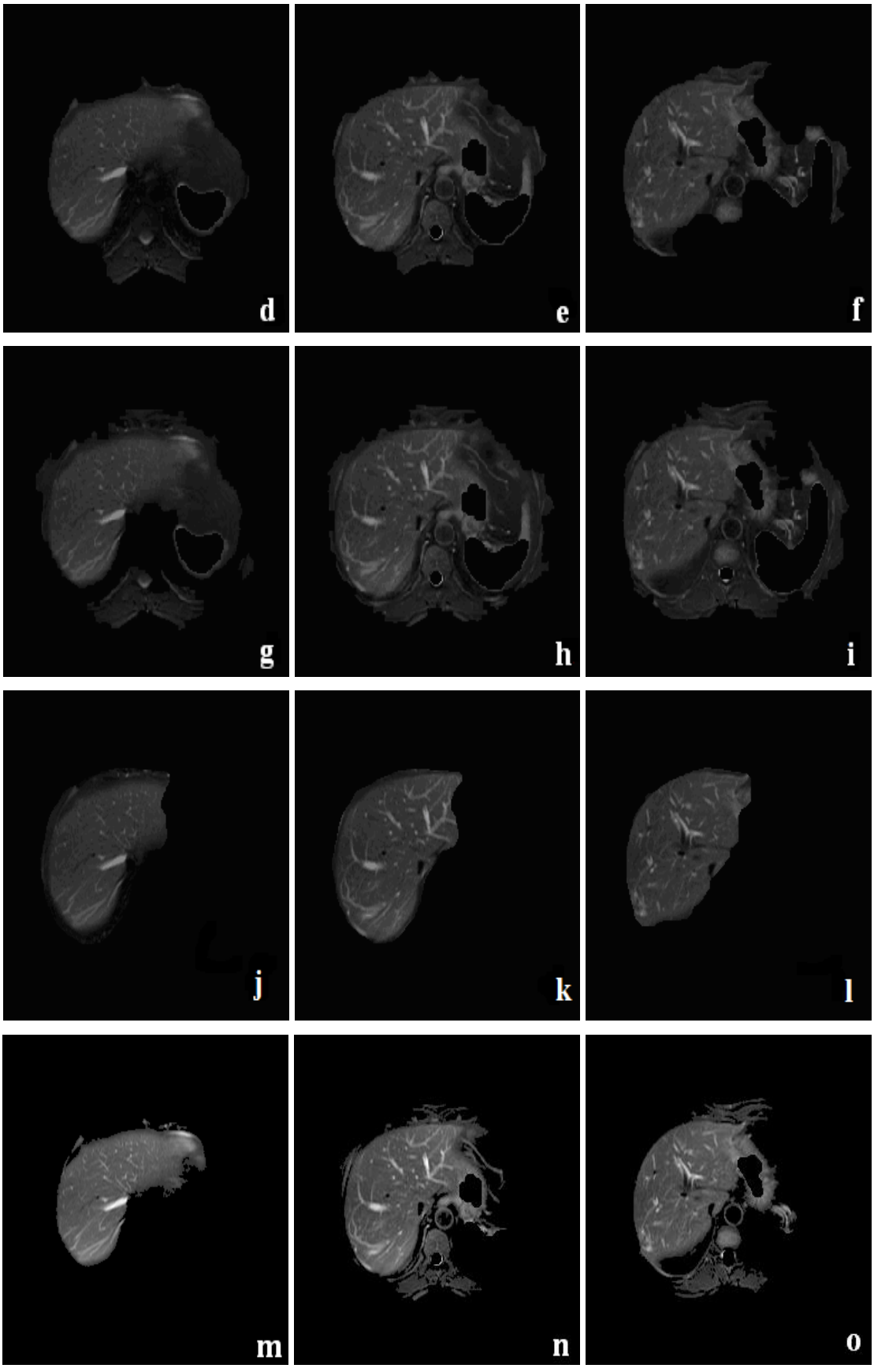

Figure 5.2. (cont.)

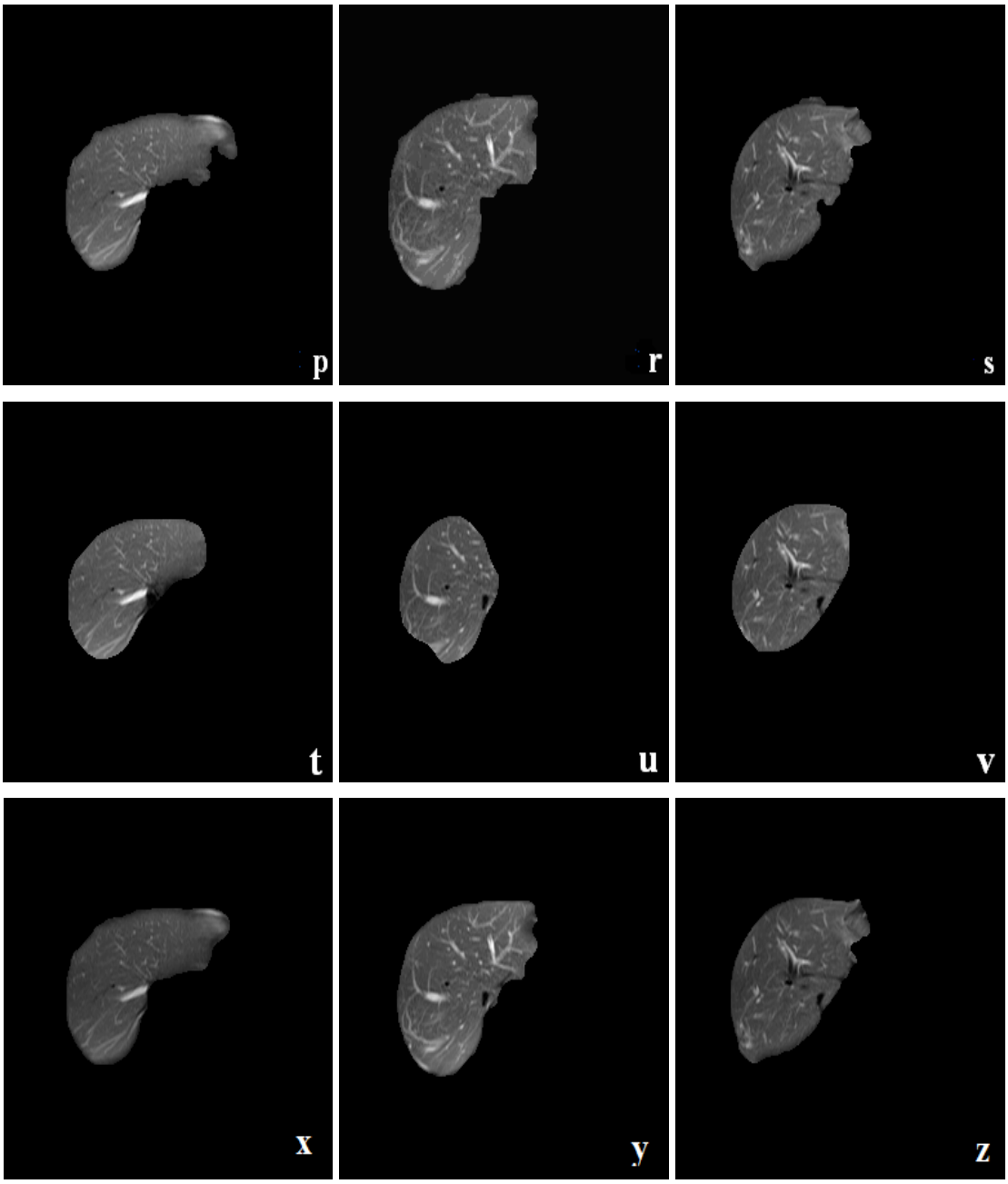

Figure 5.2. (cont.)

Figure 5.3.a, Figure 5.3.b and Figure 5.3.c show original slices which have kidneys and gallbladder. The results obtained from these slices by using the automatic GMM (Figure 6.3.d, Figure 6.3.e and Figure 6.3.f), automatic K-means (Figure 5.3.g, Figure 5.3.h and Figure 5.3.i), MLP (Figure 5.3.j, Figure 5.3.k and Figure 5.3.l), FTC method (Figure 5.3.m, Figure 5.3.n and Figure 5.3.o), automatically applied FTC based method (Figure 5.3.p, Figure 5.3.r and Figure 5.3.s), DRLSE with SPF function based method (Figure 5.3.t, Figure 5.3.u and Figure 5.3.v) and also the proposed liver

segmentation method (Figure 5.3.x, Figure 5.3.y and Figure 5.3.z) are shown in Figure 5.3.

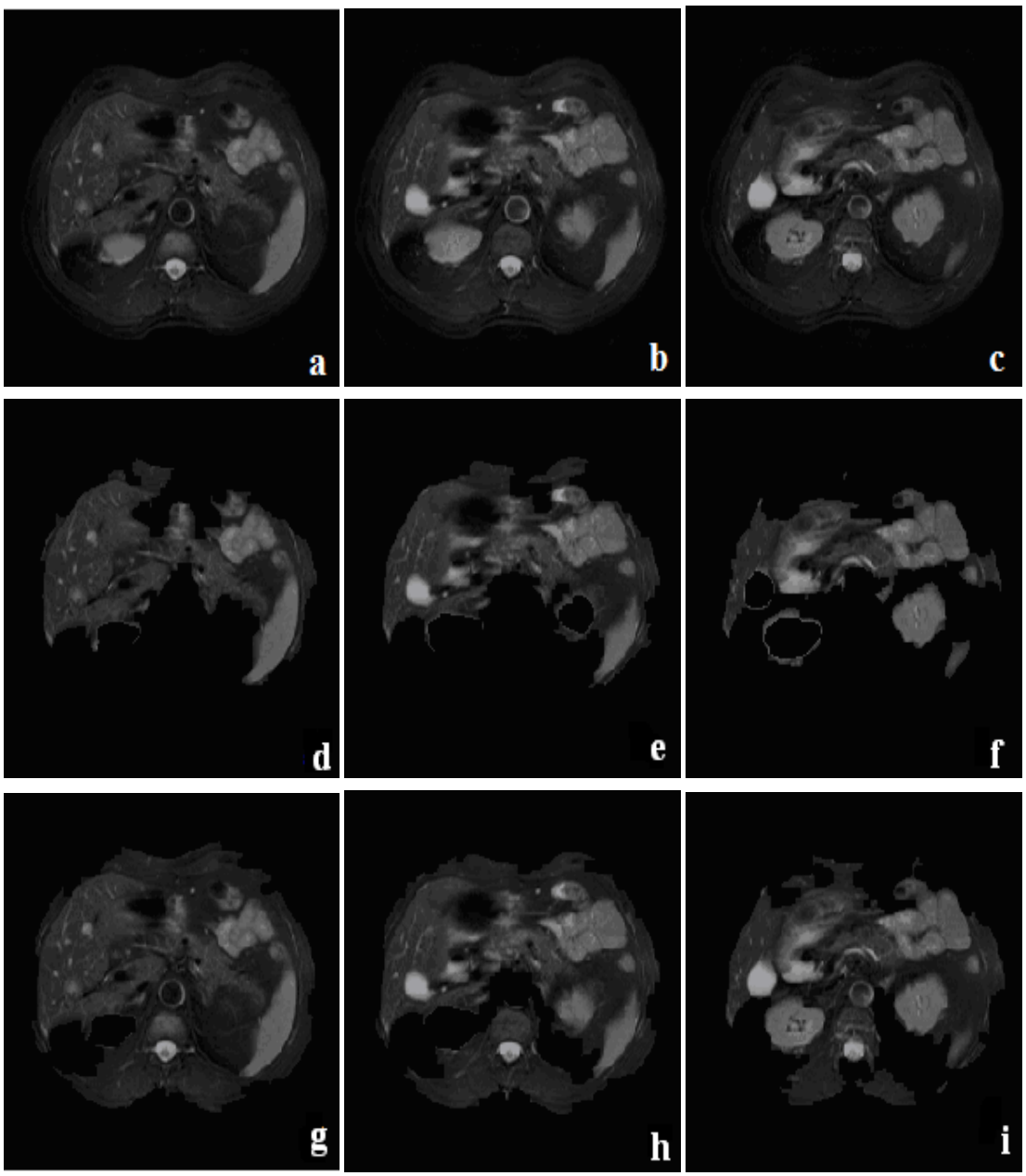

Figure 5.3. Original slices (a, b, c); Results of the automatic GMM (d, e, f); K-means (g, h, i); MLP (j, k, l); FTC method (m, n, o); Automatically applied FTC method (p, r, s); DRLSE with SPF function (t, u, v); Proposed liver segmentation method (x, y, z)

(cont. on next page)

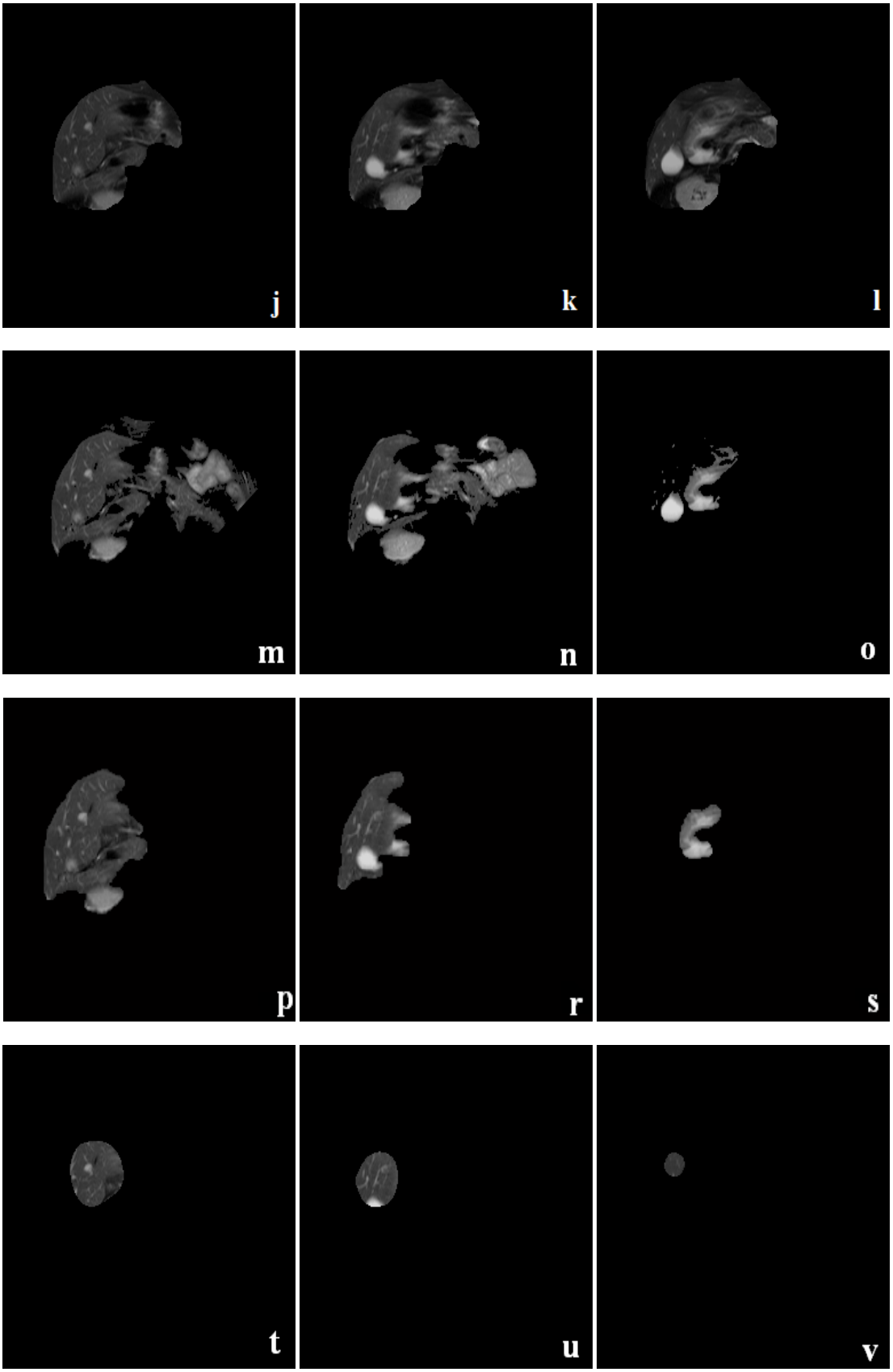

Figure 5.3. (cont.)

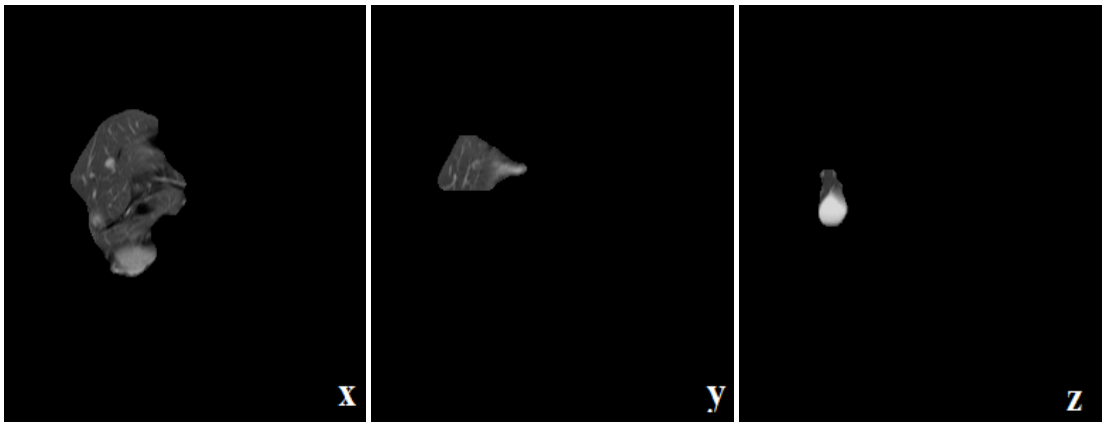

Figure 5.3. (cont.)

Figure 5.4.a, Figure 5.4.b and Figure 5.4.c show pre-processed images of the slices given in Figure 5.3.a, Figure 5.3.b and Figure 5.3.c. The liver segmentation results from these preprocessed images by using the automatic GMM (Figure 5.4.d, Figure 5.4.e and Figure 5.4.f), automatic K-means (Figure 5.4.g, Figure 5.4.h and Figure 5.4.i), MLP (Figure 5.4.j, Figure 5.4.k and Figure 5.4.l), FTC method (Figure 5.4.m, Figure 5.4.n and Figure 5.4.o), automatic FTC algorithm based method (Figure 5.4.p, Figure 5.4.r and Figure 5.4.s), DRLSE with SPF function based method (Figure 5.4.t, Figure 5.4.u and Figure 5.4.v) and also the proposed liver segmentation method (Figure 5.4.x, Figure 5.4.y and Figure 5.4.z) are presented in Figure 5.4.

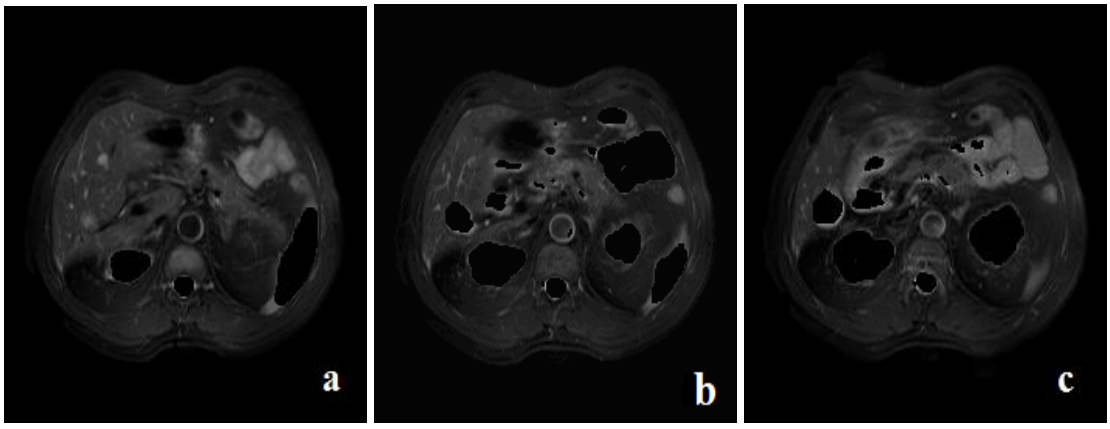

Figure 5.4. Pre-processed slices (a, b, c); Results of the automatic GMM (d, e, f); K-means (g, h, i); MLP (j, k, l); FTC method (m, n, o); Automatically applied FTC method (p, r, s); DRLSE with SPF function (t, u, v); The proposed liver segmentation method (x, y, z)

(cont. on next page)

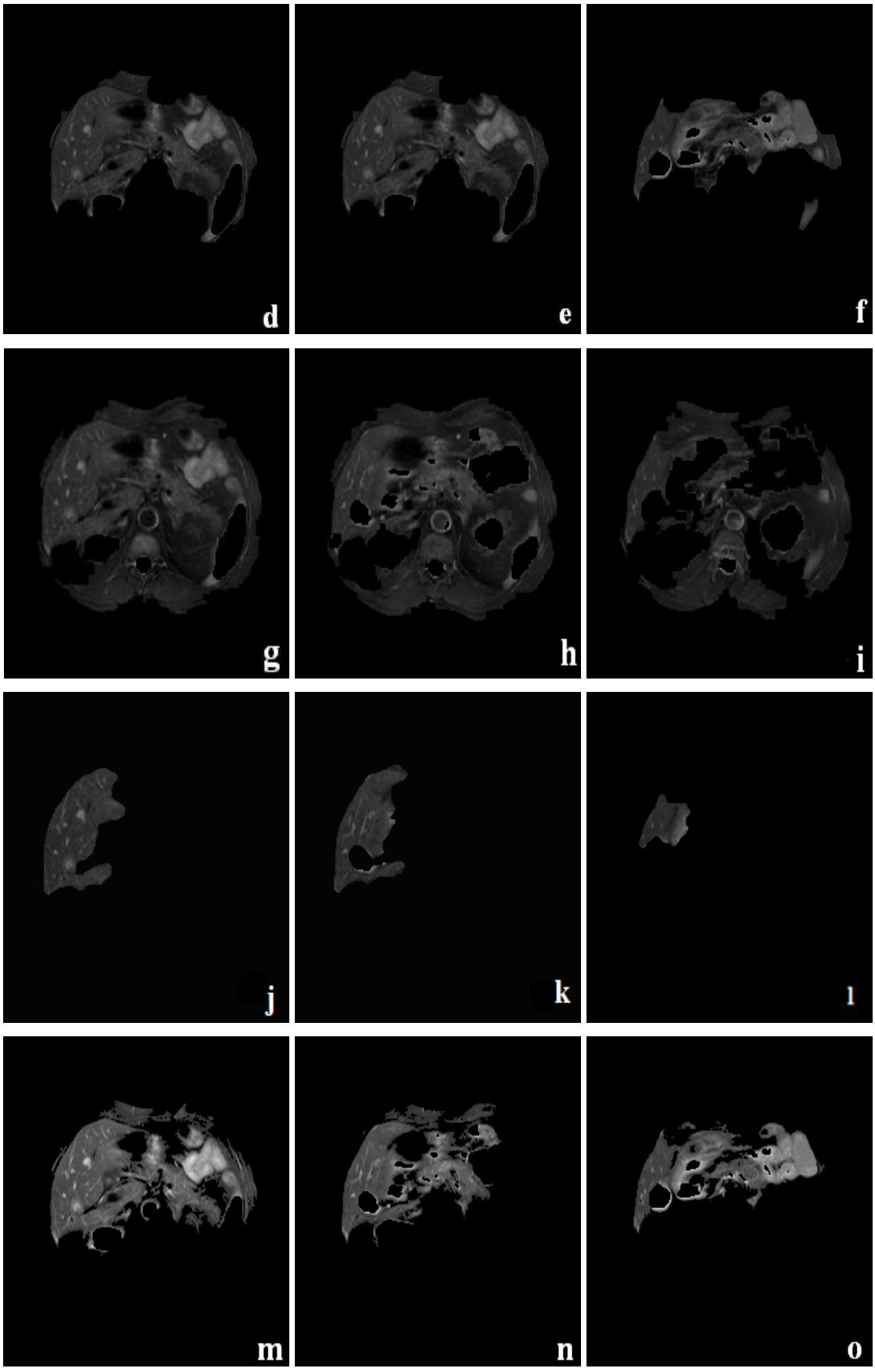

Figure 5.4. (cont.)

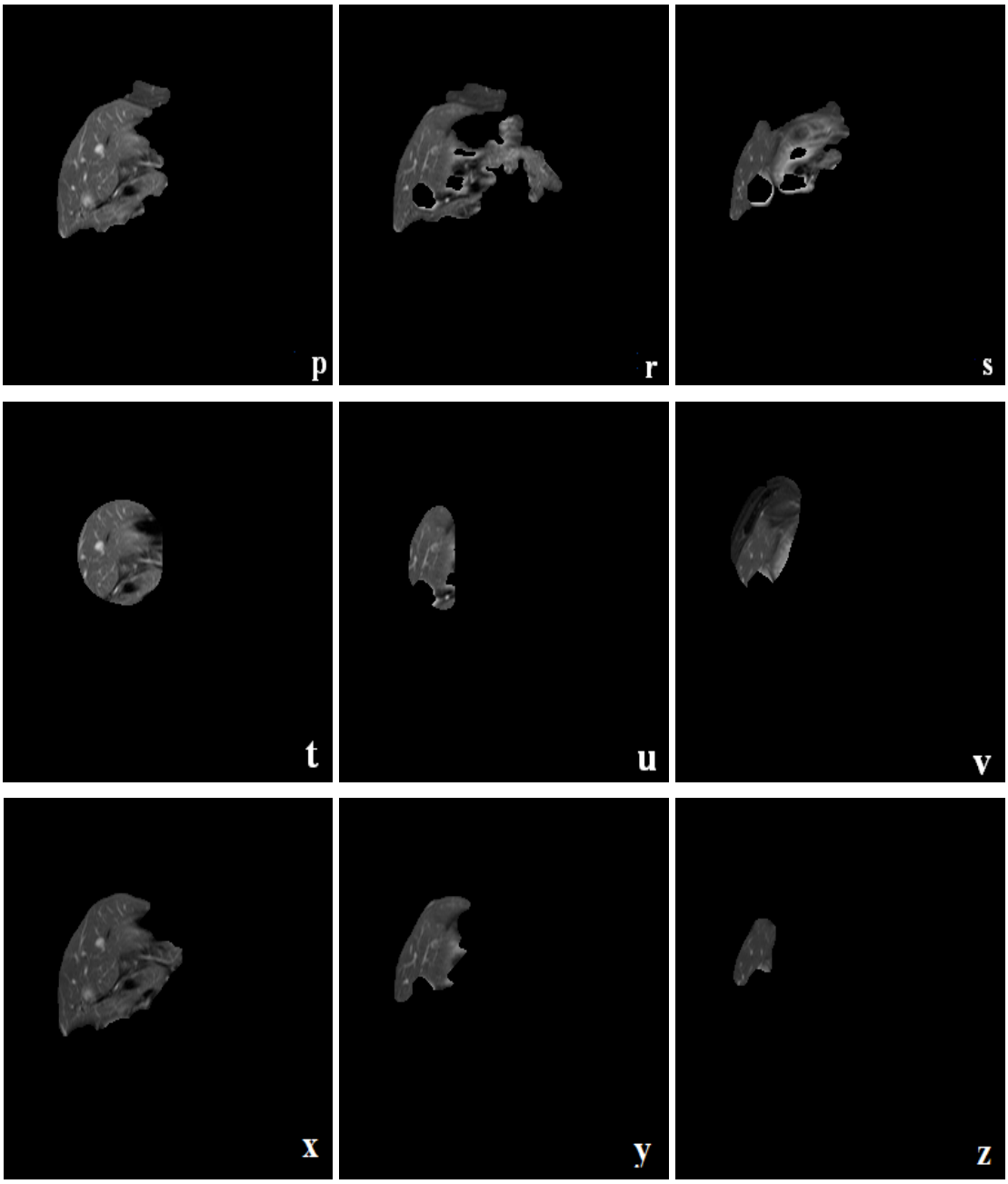

Figure 5.4. (cont.)

It is observed from the results (Figure 5.1 and Figure 5.3) that the methods presented in this thesis may not work efficiently without applying pre-processing steps. Because, gray level values of liver, which are very similar to gray level values of other abdominal organs in SPIR images, are in-homogeny. Also, existence of a gallbladder, which seems white on SPIR images and has different shape, size or position, affects intensity based liver segmentation methods presented in this paper.

We have showed with the results (Figure 5.2 and Figure 5.3) that some of the methods presented in this paper might be unsuccessful for liver segmentation in some

cases even we apply pre-processing steps. Because liver organ has a vascular structure and vessels on liver have bright white colour. Therefore, thickness of vessels and in-homogeny intensity values of liver affect segmentation performances. Low image contrastness of abdominal SPIR images is another important factor that affects efficiency of liver segmentation methods. In addition, if user defined initial contours and iteration numbers for the FTC algorithm and DRLSE with SPF function method are not chosen appropriately then segmented results may not be efficient.

The following five important statements should be identified in this section. First, it is observed that K-means and GMM based segmentation approaches are not reasonable for liver segmentation from SPIR image datasets even if preprocessed images are used. Second, the results obtained from the MLP based method are not successful when the pre-processing steps are not applied. Third, the automatic segmentation technique by using the FTC algorithm represents desired liver images from the preprocessed slices. However, this method is not successful for the slices which have kidneys or gallbladders in their originals. Next, the DRLSE with SPF function based technique is sensitive to the chosen parameters especially the variance of the Gaussian kernel function. Finally, the proposed level set based liver segmentation algorithm always yields the fastest results due to the applied SPF function and regularization method. Also, the proposed method gives the most successful result if it is not the second most successful result when the MLP, FTC or DRLSE with SPF function do not present the most accurate one.

Quantitative performance analyses have been performed to compare the results obtained from the approaches presented in this thesis according to their segmentation efficiency and required computational cost. Performance evaluations of these methods with sensitivity, specificity and accuracy measures are presented in the next Chapter.

CHAPTER 6

PERFORMANCE ANALYSES

We have performed quantitative analyses to compare segmentation performance of the results shown in Chapter 5, which have been obtained from seven different algorithms presented in Chapter 3 and 4. There are several performance measures to evaluate methods in the literature. Generally sensitivity, specificity and accuracy are used (Chen et al. 2013, Bhowmick et al. 2013, Biganzoli et al. 2013, Choi et al. 2013). These measures are defined as

$$\text{Sensitivity} = \frac{TP}{TP + FN} \tag{6.1}$$

$$\text{Specificty} = \frac{TN}{TN + FP} \tag{6.2}$$

$$\text{Accuracy} = \frac{TN + TP}{TP + TN + FP + FN} \tag{6.3}$$

where TP (True Positive) is the number of pixels of the foreground that are correctly classified, TN (True Negative) is the number of pixels of the background that are correctly classified, FP (False Positive) is the number of pixels of the background that are classified as foreground and FN (False Negative) is the number of pixels of the foreground that are classified as background. The four possible classifications are depicted in Figure 6.1 as a confusion matrix. The correct classifications, which are the TP and TN, are shown along the diagonal of the table. The model errors, which are the FP and FN, are shown in the other fields of the table. We only see the TP and TN fields as filled out while the remaining fields are set as zero for a perfect classification.

		Observed	
		True	False
Predicted	True	True Positive (TP)	False Positive (FP)
	False	False Negative (FN)	True Negative (TN)

Figur 6.1. Confusion matrix

We have evaluated all segmentation methods presented in this paper by using these three metrics. Table 6.1 shows measured values of sensitivity, specificity and accuracy for the example results shown in Figure 5.2 and Figure 5.4. In addition, Table 6.1 lists the computational cost, which have been obtained by using 2 GB RAM and 2.40 GHz. Intel Pentium CPU, for each method. It has been observed from the values in Table 6.1 that the proposed method gives always fast and the closest result to the most accurate result if it is obtained from either MLP or automatic FTC or DRLSE with SPF method. Otherwise, the proposed method gives the most accurate result with the lowest computational cost.

Table 6.1 Quantitative analysis of all methods presented in this paper

Original Image	Method	In percentage			Required Time (in second)
		Sensitivity	Specificity	Accuracy	
Figure5.4.a	GMM	**84.43**	82.76	83.06	63.83
	K-means	81.11	75.51	75.97	8.32
	MLP	58.63	**95.00**	92.03	564.29
	FTC	82.34	86.55	86.21	40.22
	Automatic FTC	83.04	94.27	**93.35**	3.03
	DRLSE with SPF	52.92	94.81	91.40	11.65
	Proposed method	66.16	94.29	92.00	9.28
Figure5.4.b	GMM	**84.77**	84.55	84.56	70.94
	K-means	72.06	76.48	76.26	9.06
	MLP	78.01	94.81	**94.00**	675.61
	FTC	72.87	89.65	88.84	29.97
	Automatic FTC	75.00	91.03	90.26	3.75
	DRLSE with SPF	43.91	**94.95**	92.50	11.63
	Proposed method	50.51	94.81	92.68	7.28

(cont. on next page)

Table 6.1. (cont.)

Figure 5.4.c	GMM	68.27	84.54	85.15	85.77
	K-means	59.16	81.36	80.83	9.80
	MLP	54.04	94.70	93.72	785.85
	FTC	64.11	88.54	87.95	23.48
	Automatic FTC	**69.55**	93.34	92.76	6.03
	DRLSE with SPF	55.69	93.79	92.87	11.67
	Proposed method	41.58	**94.94**	**93.82**	3.96
Figure 5.2.a	GMM	86.44	85.61	85.70	79.71
	K-means	86.59	85.19	85.35	7.56
	MLP	85.18	93.21	92.30	11798.03
	FTC	**86.75**	93.51	92.75	6.60
	Automatic FTC	86.30	93.82	92.97	14.42
	DRLSE with SPF	77.78	**94.91**	**92.98**	12.35
	Proposed method	70.60	94.19	91.53	4.18
Figure5.2.b	GMM	85.95	84.15	84.38	55.45
	K-means	86.08	81.26	81.87	6.04
	MLP	84.72	94.14	92.95	965.89
	FTC	**88.08**	94.10	88.97	39.28
	Automatic FTC	88.07	**94.79**	**93.94**	11.69
	DRLSE with SPF	54.28	94.85	89.73	11.69
	Proposed method	86.92	94.51	93.55	8.61
Figure 5.2.c	GMM	90.28	86.41	86.84	51.24
	K-means	85.10	81.60	81.99	4.54
	MLP	**91.70**	94.00	93.75	229.19
	FTC	86.91	89.22	88.96	41.65
	Automatic FTC	86.55	93.96	93.13	8.81
	DRLSE with SPF	80.98	95.93	**94.26**	11.65
	Proposed method	76.67	**94.08**	92.13	6.84

Figure 6.2 shows manually segmented reference images (Figure 6.2.a, b, c, d, e and f) that we have used for quantitative analyses of the implementation results.

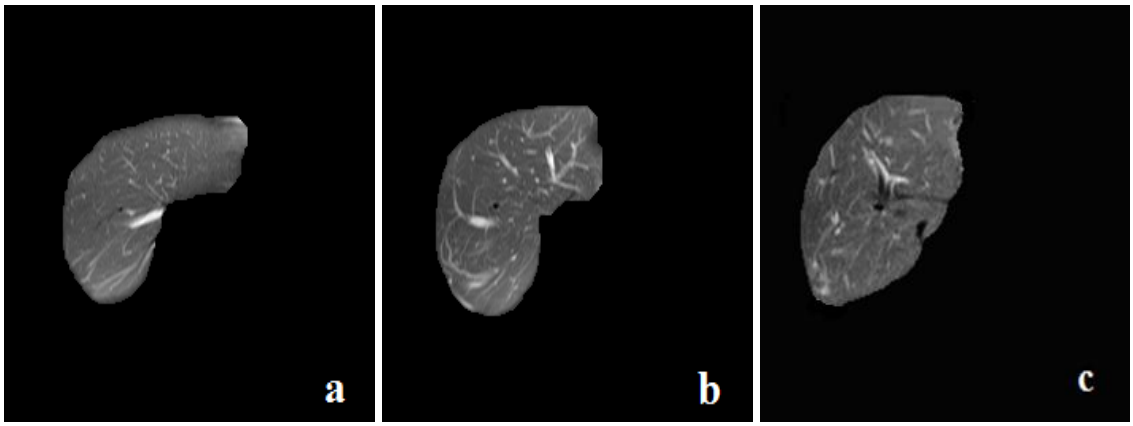

Figure 6.2 Manually segmented reference images (a, b, c, d, e and f)

(cont. on next page)

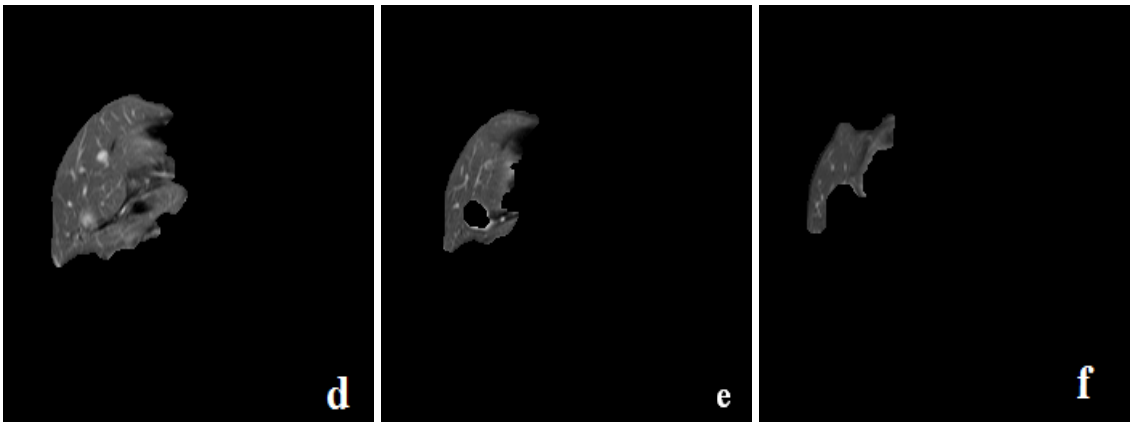

Figure 6.2. (cont.)

Sensitivity measures success of a method about identification of the TP and FP cases. Specificity indicates that how well the method can identify the TN and FN cases. Therefore, accuracy is low (high) when both specificity and sensitivity are low (high). However, only accuracy is not a good measure for performance evaluation. Because the value of accuracy is biased towards either specificity or sensitivity when any one of specificity or sensitivity has high value and the other has low value. Therefore, we have presented images whose sensitivity and specificity values are mostly close to each other. The comparison in Table 6.2 summarizes the advantages and disadvantages of the applied methods in terms of accuracy, computational cost, requirement of manual initialization and number of parameters.

Table 6.2. Advantages and disadvantages of presented methods for liver segmentation from SPIR images

Method	Requirement of Manual Initialization	Required Number of Parameter	Requirement of Post-processing	Accuracy	Fast/Slow
GMM	No	3 (number of classes, variance of the Gaussian function, selected initial slice number)	Yes	• Higher than K-means method • Lower than all presented methods in this paper except K-means method	• Faster than MLP method • Slower than all presented methods in this paper except MLP method
K-means	No	2 (number of classes, selected initial slice)	Yes	• Lower than all methods presented in this paper	• Faster than GMM and MLP method

(cont. on next page)

Table 6.2. (cont.)

MLP	No	4 (number of iterations, learning rate, error tolerance, selected initial slice)	Yes	• Higher than GMM, K-means and FTC method	• Slower than all methods presented in this paper
FTC	Yes	5 (number of iterations for regularization and data dependent cycles, initial curve, size of Gaussian filter, variance of Gaussian filter)	Yes	• Higher than GMM and K-means method • Lower than DRLSE with SPF, automatic FTC and the proposed method • Accuracy decreases when image contrastness decreases or intensity in-homogeneity increases	• Slower than automatic FTC method • Faster than GMM and MLP method
Automatic FTC	No	4 (number of iterations for regularization and data dependent cycles, size of Gaussian filter, variance of Gaussian filter)	Yes	• Higher than GMM, K-means and FTC method • Lower than DRLSE with SPF and the proposed method • Accuracy decreases when image contrastness decreases or intensity in-homogeneity increases (even if post-processing is applied)	• Faster than GMM and MLP method
DRLSE with SPF	Yes	6 (3 coefficients for the area, length and regularization terms, number of iterations, variance of the Gaussian kernel, initial curve)	No	• Higher than GMM, K-means and FTC • Highly sensitive to chosen constant coefficients and sigma parameter in the energy function	• Slower than K-means, automatic FTC and the proposed method • Faster than GMM and MLP method
Proposed Method	No	6 (3 coefficients for area, length and regularization terms, number of iterations, variance of the Gaussian, initial curve)	No	• Higher than K-means, GMM and FTC method	• Faster than GMM, MLP, FTC and DRLSE with SPF method

CHAPTER 7

CONCLUSION

The thesis compares the performance of various approaches in liver segmentation from SPIR images by explaining all the steps of the methods under consideration. Also, a novel level set based approach by using a SPF function has been proposed for liver segmentation in this thesis.

The implemented GMM based segmentation with EM algorithm has an advantage over other methods since the correlation of gray values can be potentially accounted by the covariance structure. Therefore, the probabilistic technique is more flexible than K-means that is a heuristic method, which uses distance values of gray levels and lacks of a statistical foundation. In other words, the GMMs are soft than K-means since each data item has either 0% or 100% membership to its closest cluster in K-means. However, in GMM, each data x_n belongs to cluster Θ_k with $p(\Theta_k \mid x_n)100\%$ and each data contributes to some extent. K-means is a limited version of GMM with equal weight and equal spherical covariance, $\sum_k = \sigma^2 I$. K-means algorithm can not adapt to any cluster shape. Its cluster modeling capability is limited to spherical clusters with similar number of data points. In the GMM, each mixture component is viewed as clusters of arbitrary ellipsoidal shapes. Therefore, the decision in K-means clustering algorithm is hard due to the assigning each data item to a single cluster. The decision in GMM clustering algorithm is soft due to having a posterior probability for each data item, which presents that each data item has a probability to belong to each cluster. However, the drawback of EM algorithm is its sensitivity to chosen initial values. The result of GMM method depends on the number of chosen components. We have chosen a constant kernel number in the implementation for the abdominal organ segmentation from SPIR datasets. The parameter values of the GMM are recalculated iteratively by starting from initial parameters until convergence.

We showed that neither the proposed GMM based nor the K-means based iterative segmentation method has not the ability of accurate segmentation of the liver organ in SPIR datasets because of the gray level similarities, intensity inhomogeneities and the partial volume effects. Only unsupervised approaches such as K-means or

model-based techniques to segment liver organ from SPIR images do not give sufficient results. Therefore, we have applied MLP based liver segmentation method, which is a supervised learning approach, after several preprocessing steps and obtained successful results. However, the drawback of this method is very high computational cost.

LSMs have an important advantage over other image segmentation algorithms like watershed, edge detection, thresholding or region growing methods since they can be formulated by an energy minimization functional. Global or local image information (such as shape or gray level distribution) can be used in the energy formulation to perform image segmentation efficiently **(**Chan and Vese 2001, Chen et al. 2002, Thieu et al 2011). Therefore, we have explained the properties of recently published two different level set based segmentation techniques and presented their implementation results for liver segmentation. The FTC algorithm, which uses a switching mechanism, seems successful and can give acceptable results when preprocessed abdominal images are used. However, the drawback of the FTC algorithm is its sensitivity of initial contours that are defined on each slice. Because the accuracy of the results obtained from the FTC method depends on not only the size of initial contours, which are drawn by users, but also number of initial contours and their positions. In addition, the user defined iteration numbers for each slice affect the segmentation results. Therefore, this approach is not robust and generates over-segmented or under-segmented images on some slices. In order to overcome these drawbacks, we have applied an automatic method iteratively by using the FTC algorithm without any user interaction and with a small fixed number of iterations for liver segmentation from SPIR datasets. However, we have observed that the automatic liver segmentation which uses the FTC method is not successful for SPIR datasets due to in-homogeny intensity values even if preprocessed images are used. Therefore, we have applied the DRLSE with SPF function based automatic segmentation method that gives fast and reasonable results without any post-processing operation. Also, this method is more efficient than the MLP based segmentation method in terms of the required segmentation time. However, it is very sensitive to the variance of the Gaussian kernel function in the edge stopping term. Our proposed LSM that uses a novel SPF function, which can control the direction and velocity of the evolving active contour, solves this sensitivity problem since it does not include the variance parameter. Also, the proposed method has lower computational cost since it does not use a regularization term.

Both qualitative and quantitative comparison results of eight different active contour methods except the application specific methods are presented in (He L. et al 2008) for brain MRI, ultrasound pig heart image, kidney CT image, knee MRI and microscopy blood cell image. However, there is no comparative study for liver segmentation on SPIR images, which show the vascular structure of the liver very clear and very useful for vessel segmentation. None of the proposed approaches that are the deterministic iterative method, which is the K-means based segmentation, the probabilistic model based iterative method, which is the GMM based segmentation with EM, the supervised learning method, which is the MLP based segmentation and also four different level set based methods have been applied for liver segmentation from SPIR images. The contribution of this study is to make a comparison of state of the art methods and present their results for liver segmentation on abdominal MRIs. Seven different algorithms have been implemented and their results obtained from SPIR image datasets have been presented in this thesis. Also, we have proposed a LSM with an SPF function by using pre-processed images without any post-processing operation in Chapter 5. Figure 7.1 shows an example of segmented liver surface in 3D coronal view (Figure 7.1.a), sagital view (Figure 7.1.b) and axial view (Figure 7.1.c) using the segmented images, which have been obtained by the proposed method.

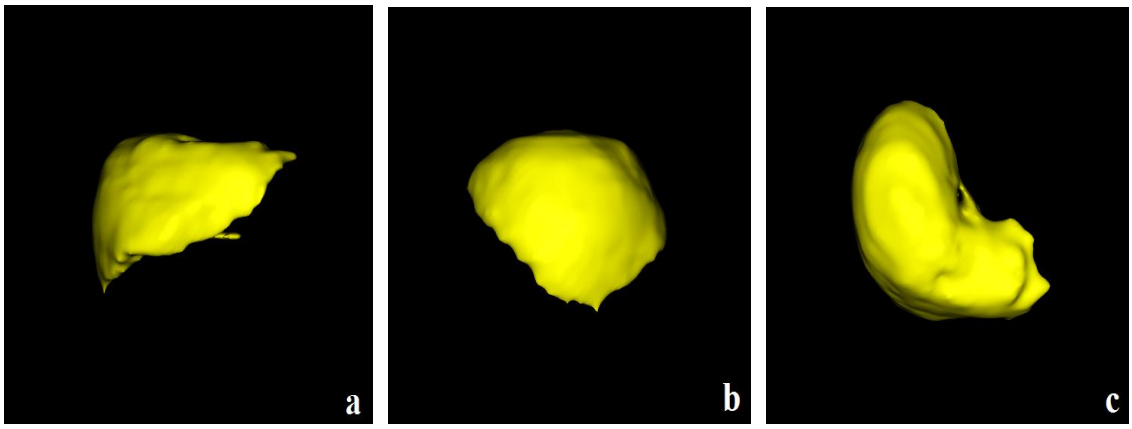

Figure 7.1. An example of segmented liver surface in 3D coronal view (a), sagital view (b) and axial view (c)

Vessel segmentation and to obtain Couinaud segments from the segmented SPIR images will be extensions of this work.

REFERENCES

Abdelmunim, H., Farag, A. A., Miller, W., AbdelGhar, M., 2008. A kidney segmentation approach from DCE-MRI using level sets. Conference on Computer Vision and Pattern Recognition Workshops (CVPRW), IEEE Press, Anchorage, 1-6.

AbdulNazeer, K. A., Sebastian, M. P., 2009. Improving the accuracy and efficiency of the k-means clustering algorithm. International Conference on Data Mining and Knowledge Engineering (ICDMKE), Proceedings of the World Congress on Engineering (WCE-2009)

Amini, A. A., Weymouth, T. E., Jain, R. C., 1990. Using dynamic programming for solving variational problem in vision. IEEE Trans. Pan. Anal. Mach. Intell., 12(9), 855-867.

Anderberg, M. R., 1973. Cluster Analysis for Applications. Academic Press, New York, NY

Aubert, G., Kornprobst, P., 2002. Mathematical Problems in Image Processing: Partial Differential Equations and the Calculus of Variations, Springer, New York, 2002.

An, J., Rousson, M., Xu, C., 2007. Γ-convergence approximation to piecewise smooth medical image segmentation. MICCAI (2), 495–502.

Bae, K.T., Giger, M. L., Chen, C. T., Kahn, C. E. Jr., 1993. Automatic segmentation of liver structure in CT images. Med. Phys., 20, 71–78.

Barles, G., Soner, H. M., Sougandis, P. E., 1993. Front propagation and phase field theory. SIAM J. Control Optim., 31(2), 439–469.

Bekes, G., Nyül, L. G., Máté, E., Kuba, A., Fidrich, M., 2007. 3D segmentation of liver, kidneys and spleen from CT images", International Journal of Computer Assisted Radiology and Surgery, 2(1), 45-46.

Bernard, O., Friboulet, D., Thevenaz, P., Unser, M., 2009. Variational B-spline level-set: A linear filtering approach for fast deformable model evolution. IEEE Trans. Image Process., 18, 1179–1191

Bhowmick, T., Mirrett, S., Reller, L. B., Price, C., Qi, C., Weinstein, M. P., Kirn, T. J., 2013. Controlled Multicenter Evaluation of a Bacteriophage Based Method for the Rapid Detection of Staphylococcus aureus in Positive Blood Cultures. Journal of Clinical Microbiology (JCM.02967-12), 51(4), 1226-30.

Bidaut, L., 2000. Data and Image Processing for Abdominal Imaging, Abdominal Imaging, 25, 341-360.

Biganzoli, L., Boni, L., Becheri, D., Zafarana, E., Biagioni, C., Cappadona, S., Bianchini, E., Oakman, C., Magnolfi, S. U., Leo D. A., Mottino, G., 2013. Evaluation of the cardiovascular health study (CHS) instrument and the Vulnerable Elders Survey-13 (VES-13) in elderly cancer patients. Are we still missing the right screening tool?. Annals of Oncology, 24, 494–500.

Blande, C., 1980. Isoperimetric inequalities and applications. Pitman, Boston

Blum, H. A., 1967. Transformation for extracting new descriptors of shapes. W. Wathen-Dunn (ed.), Models for the Perception of Speech and Visual Form, MIT Press, Cambridge, 362- 380.

Boesen, K., Rehm, K., Schaper, K., Stoltzner, S., Woods, R., Luders, E., Rottenberg, D., 2004. Quantitative comparison of four brain extraction algorithms. NeuroImage, 22, 1255–1261

Bresson, X., Esedoglu, S., Vandergheynst, P., Thiran, J., Osher, S., 2007. Fast global minimization of the active contours/snakes model. Journ. Math Imaging Vis., 28, 151–167.

Brown, M. S., Feng, W. C., Hall, T. R., McNitt-Gray, M. F., Churchill, B. M., 2001. Knowledge-based segmentation of pediatric kidneys in CT for measurement of parenchymal volume. Journal of Computer Assisted Tomography, 25(4), 639-648.

Burrel, M., Llovet, J. M., Ayuso, C. et al., 2003. MRI Angiography is superior to helical CT for detection of HCC prior to liver transplantation: An explant correlation. Hepatology, 38, 1034–1042.

Caselles, V., Catte, F., Coll, T., Dibos, F., 1993. A geometric model for active contours in image processing. Numerische Mathematic, 66(1),1–31.

Caselles, V., Kimmel, R., Sapiro, G., 1997. Geodesic active contours. Int. J. Comput. Vis., 22(1), 61–79.

Chakraborty, A., Duncan, J. S., 1999. Game-theoretic Integration for Image Segmentation. IEEE Trans. Pattern Anal. Machine Intell. 21(1), 12–30.

Chan, T., Vese, L., 2001. Active contours without edges. IEEE Trans. Image Process., 10(2), 266–277.

Chan, T., Esedoglu, S., Nikolova, M., 2006. Algorithms for finding global minimizers of image segmentation and denoising models. Siam. Journ. Appl. Math. 66(5), 1632-1648.

Charbuillet, C., Tardieu, D., Peeters, G., 2011. GMM Supervector for content based music similarity. 14th International conference on Digital Audio Effects (DAFx-11), Paris, France.

Chen, G., Gu, L., Qian, L., Xu, J., 2009. An improved level set for liver segmentation and perfusion analysis in MRIs. IEEE Trans. On Information Technology in Biomedicine 13(1), 94-103.

Chen, W., Zhuang, H., Cheng, G., Torigian, D. A., Alavi, A., 2013. Comparison of FDG-PET, MRI and CT for Post Radiofrequency Ablation Evaluation of Hepatic Tumors. Ann. Nucl. Med., 27, 58–64.

Chen, Y. W., Tsubokawa, K., Foruzan, A. H., 2010. Liver Segmentation from Low Contrast Open MR Scans Using K-Means Clustering and Graph-Cuts. Advances in Neural Networks - ISNN 2010, Lecture Notes in Computer Science, 6064, 162-169.

Chen, Y., Thiruvenkadam, S., Huang, F., Tagare, H. D., Wilson, D., Geiser, E. A., 2001. On the incorporation of shape priors into geometric active contours. Proceedings of the IEEE Workshop on Variational and Level Set Methods, 145–152.

Chen, Y., Tagare, H., Thiruvenkadam, S., Huang, F., Wilson, D., Gopinath, K., Briggs, R., Geiser, E., 2002. Using prior shapes in geometric active contours in a variational framework. Int. J. Comput. Vis., 50, 315-328.

Cheng, K., Lixu, G., Jianghua, W., Wei, L., Jianrong, X., 2008. A novel level set based shape prior method for liver segmentation from MRI images", MIAR-2008, LNCS 5128, 150–159.

Chopp, D., 1993. Computing minimal surfaces via level set curvature flow. J. Comput. Phys., 106, 77–91.

Choi, J. H., Park, K., Kim, Y., 2013. Comparison of Clinical Utility between New and Old Bleeding Criteria: A Prospective Study of Evaluation for the Bleeding Academic Research Consortium Definition of Bleeding in Patients with Undergoing Percutaneous Intervention. Journal of the American College of Cardiology (JACC), 61(10), doi:10.1016/S0735-1097(13)60142-4

Chou, J. S., Chen, S.Y., Sudakoff, G. S., Hoffmann, K. R., Chen, C. T., Dachman, A. H., 1995. Image fusion for visualization of hepatic vasculature and tumors. Proc. of SPIE, 2434, 157–163.

Cohen, L. D., 1991. On active contour models and balloons. CVGIP Image Understand, 52(2), 211–218.

Cohen, L. D., Kimmel, R., 1997. Global minimum for active contour models. A Minimal Path Approach, Int. J. Comput. Vision, 24(1), 57–78.

Cohen, L., Cohen, I., 1993. Finite element methods for active contour models and balloons for 2-D and 3-D images. IEEE Trans. Pattern Anal. Machine Intell., 15(11), 131–1147.

Coleman, G. B., Andrews, H. C., 1979. Image segmentation by clustering. Proceedings of IEEE, 5, 773–785.

Condon, B. R., Patterson, J., Wyper, D., Jenkins, A., Hadley, D. M., 1989. Image non-uniformity in magnetic resonance imaging: its magnitude and methods for its correction. The British Journal of Radiology, 60, 83–87.

Couinaud, C., 1999. Liver anatomy: Portal (and suprahepatic) or biliary segmentation. Digestive Surgery, 16, 459-467.

Delingette, H., Montagnat, J., 2001. Shape and topology constraints on parametric active contours. Comput. Vis. Image Understand., 83,140–171.

Dempster, A., Laird, N., Rubin, D., 1977. Maximum likelihood from incomplete data via the EM algorithm. Journal of the Royal Statistical Society, 39,1–38

Dice, L., 1945. Measures of the amount of ecologic association between species. Ecology, 26, 297–302

Duda, R. O., Hart, P. E., 1973. Pattern Classification and Scene Analysis. John Wiley and Sons Inc.

Drake, R., 2004. Gray's anatomy for students. 1995-2012 Lavoisier S.A.S., Chp.4, 218.

Dongxiang, C., Tiankun, L., 2009. Iterative quadtree decomposition segmentation of liver MR Images. International Conference on Artificial Intelligence and Computational Intelligence, AICI, 3, 527-529.

Epstein, C. L., Gage, M., 1987. The curve shortening flow. In A. Chorin and A. Majda editors, Wave Motion: Theory, Modeling and Computation. Springer-Verlag, New York, 37-38.

Eschrich, S., Ke, J., Hall, L.O., Goldgof, D. B., 2003. Fast accurate fuzzy clustering through data reduction. IEEE Trans. Fuzzy Systems, 11 (2), 262–270.

Evans, L., 1998. Partial differential equations. American Mathematical Society.

Everitt, B., Hand, D., 1981. Finite mixture distributions monographs on applied probability and statistics. Chapman & Hall, London.

Fahim, A. M., Salem, A. M., Torkey, F. A., Ramadan, M. A., 2006. An Efficient enhanced k-means clustering algorithm. Journal of Zhejiang University 10(7), 1626-1633.

Fenchel, M., Thesen, S., Schilling, A., 2008. Reconstructing liver shape and position from MR image slices using an active shape model. Proc. of SPIE, 6914, 69144N.

Fenster, S. D., Kender, J. R., 2001. Sectored snakes: Evaluating learned energy segmentations. IEEE Trans. Pattern Anal. Machine Intell., 23(9), 1028–1034.

Figueiredo, M. A. T., Jain, A. K., 2002. Unsupervised learning of finite mixture models. IEEE Transactions on Pattern Analysis and Machine Intelligence 24(3), 381–396.

Flohr G., Schaller S., Stierstorferi K., Bruder H., Ohnesorge B.M., Schoepf U. J., 2005. Multi detector row CT systems and image reconstruction techniques. Radiology, 235, 756-773.

Fraley, C., Raftery, A. E., 2002. Model-based clustering, discriminant analysis, and density estimation. Jour. Am. Statist. Assoc. 97, 611–631.

Frangi, A. F., Niessen W. J., Viergever M. A., 2001. Three-dimensional Modelling for Functional Analysis of Cardiac Images: A review. IEEE Trans. Med. Imaging 20(1), 2–25.

Frühwirth S. S., 2006. Finite Mixture and Markov Switching Models. Springer, New York.

Gao, L., Heath, D. G., Kuszyk, B. S., Fishman, E. K., 1996. Automatic liver segmentation technique for three-dimensional visualization of CT data. Radiology, 201, 359–364.

Gao, J., Kosaka, A., Kak, A., 2000. A deformable model for automatic CT liver extraction. Medical Imaging 2000, SPIE Proc. 2434, 157–163.

Gibby, W. A., 2005. Basic principles of magnetic resonance imaging. Neurosurg Clinics of North America, 16, 1–64.

Giraldi, G. A., Strauss, E., Oliveira, A. A., 2000. A boundary extraction method based on dual-T-snakes and dynamic programming. Proc. IEEE Comput. Vis. Pattern Recognit. (CVPR), 44–49.

Gloger, O., Kühn, J., Stanski, A., Völzke, H., Puls, R., 2010. A fully automatic three-step liver segmentation method on LDA-based probability maps for multiple contrast MR images. International Journal of Magnetic Resonance Imaging, 28(6), 882–897.

Goceri, E., Unlu, M. Z., Guzelis, C., Dicle, O., 2012. An automatic level set based liver segmentation from MRI data sets. IPTA2012: 3rd International Conf. on Image Processing Theory, Tools and Applications, Turkey, 192-197.

Goceri, E., Ünlü, M. Z., Güzeliş, C., Dicle, O., 2012. A liver segmentation method based on partial differential equation and signed pressure force function. BIYOMUT: 17th National Biomedical Engineering Meeting Proceedings (IEEE Biomedical Engineering), Turkey, 237-240.

Goldenberg, R., Kimmel, R., Rivlin, E., Rudzsky, M., 2001. Fast geodesic active contours. IEEE Trans. Image Process., 10(10), 1467–1475.

Gomes, J., Faugeras, O., 2000. Reconciling distance functions and level sets. Journ. Vis. Commun. Image Represent, 11(2), 209–223.

Gonzalez, R. C., Woods, R. E., 1992. Digital image processing, Addison-Wesley Publications

Goryawala, M., Guillen, M. R., Cabrerizo, M., Barreto, A., Gulec, S., Barot, T. C., Suthar, R. R., Bhatt, R. N., Mcgoron, A., Adjouadi, M., 2011. A 3D liver segmentation method with parallel computing for selective internal radiation therapy", IEEE Transactions on Information Technology in Biomedicine, 16(1), 62-69.

Grayson, M. A., 1987. The heat equation shrinks embedded plane curves to round points. J. Differential Geometry,26(2), 285-314.

Hall, L. O., Bensaid, A. M., Clarke, L. P., Velthuizen, R. P., Silbiger, M. S., Bezdek, J. C., 1992. A comparison of neural network and fuzzy clustering techniques in segmenting magnetic resonance images of the brain. IEEE Transactions on Neural Networks, 3, 672–682.

Hagspiel, K. D., Neidl, K. F., Eichenberger, A. C., Weder, W., Marincek, B., 1995. Detection of liver metastases: Comparison of superparamagnetic iron oxide-enhanced and unenhanced MR imaging at 1.5T with dynamic CT, intraoperative US, and percutaneous US. Radiology, 196, 471–478.

Hawighorst, H., Schoenberg, S., Knopp, M. V., et al., 1999. Hepatic lesions: Morphologic and functional characterization with multiphase breath-hold 3D gadolinium-enhanced MR angiography-initial results. Radiology, 210,89–96.

Haykin, S., 1999. Neural networks: A comprehensive foundation, (2nd ed.) Upper Saddle River, NJ: Prentice-Hall

He, L., Peng, Z., Everding, B., Wang, X., Han, C. Y., Weiss, K. L., Wee, W. G., 2008. A comparative study of deformable contour methods on medical image segmentation. Image and Vision Computing, 26, 141–163.

Heimann, T., Wolf, I., Meinzer, H. P., 2006. Active shape models for a fully automated 3D segmentation of the liver : An evaluation on clinical data. Proceedings of MICCAI 2006, Lecture Notes in Computer Science, 4191, 41–48.

Heimann, T., Meinzer, H. P., Wolf, I., 2007. A statistical deformable model for the segmentation of liver CT volumes", MICCAI 2007 Workshop Proceedings: 3D Segmentation in the Clinic - A Grand Challenge, 161–166.

Hermoye, L., Laamari-Azjal, I., Cao, Z., Annet, L., Lerut, J., Dawant, B. M., Van Beers, B. E., 2005. Liver segmentation in living liver transplant donors: Comparison of semiautomatic and manual methods. International Journal of Radiology, 234, 171–178.

Hornak, J., 2012. The Basics of NMR http://www.cis.rit.edu/htbooks/nmr/

Huang, C. L., Kuo, L. Y., Huang, Y. J., Lin, Y. H., 2009. Shape-based level set method for kidney segmentation on CT image. 22nd Conference on Computer Vision, Graphics, and Image Processing (CVGIP), Nantou, Taiwan

Huppertz, A., Haraida, S., Kraus, A., et al., 2005. Enhancement of focal liver lesions at gadoxetic acid-enhanced MR imaging: Correlation with histopathologic findings and spiral CT-initial observations. Radiology, 243,468–478.

Husain, S. A., Shigeru, E., 2000. Use of neural networks for feature based recognition of liver region on CT images. Neural Networks for Signal Processing - Proceedings of the IEEE Workshop, 2, 831–840.

Huttenlocher, D. P., Klanderman, G. A., Rucklidge, W. J., 1993. Comparing images using the Hausdorff distance. IEEE Transactions on Pattern Analysis and Machine Intelligence, 15, 850 – 863

Ichikawa, T., 2004. MRI in the evaluation of hepatocellular nodules: Role of pulse sequences and contrast agents. Intervirology 47, 252–270.

Jain, A. K., Duin, R., Mao, J., 2000. Statistical pattern recognition review. IEEE Trans. Pattern Analysis and Machine Intelligence, 22(1),4-38

Jain, A. K., Dubes, R. C., 1988, Algorithms for clustering data. Prentice Hall.

Jha, K., Rodriguez, J. J., Stephen, R. M., Stopeck, A. T., 2010. A clustering algorithm for liver lesion segmentation of diffusion weighted MR images. IEEE SSIAI, 93-96.

Jian, B., Vemuri, B. C., 2011. Robust point set registration using Gaussian mixture models. Pattern Analysis and Machine Intelligence, IEEE Transactions, 33 (8), 1633 – 1645

Joshi, A. A., Shattuck, W.D., Damasio, H., Leahy M. R., 2012. Geodesic curvature flow on surfaces for automatic sulcal delineation. 9th IEEE International Symposium on Biomedical Imaging (ISBI), 430-433, Barcelona.

Juang, L. H., Wu, M. N., 2010. MRI brain lesion image detection based on color-converted K-means clustering segmentation. Measurement 43, 941–949

Kainmueller, D., Lange, T., Lamecker, H., 2007. Shape constrained automatic segmentation of the liver based on heuristic intensity model. MICCAI Wshp. 3D Segmentation in the Clinic: A Grand Challenge, 109-116.

Kaufman, L., Peter, R. J., 2005. Finding groups in data: An introduction to cluster analysis. Wiley series in Probability and Statistics

Katscher, U., Börnert, P., 2007. Parallel Magnetic Resonance Imaging. Neurotherapeutics, 4, 499–510.

Kimia, B. B., Tannenbaum, A., Zucker, S. W., 1990. Toward a computational theory of shape: an overview. Computer Vision–ECCV 90. (Ed. O.Faugeras). Lecture Notes in Computer Science,**427**,402–407.

Kimmel, R., 2003. Numerical Geometry of Images: Theory, Algorithms and Applications. ISBN:0-387-95562-3, Springer-Verlag New York, Inc.,17-45.

Kobashi, L., Shapiro, M., 1995. Knowledge-based organ identification from CT images. Pattern Recognition, 28, 475-491.

Kondo, H., Kanematsu, M., Hoshi, H., et al., 2000. Preoperative detection of malignant tumors: Comparison of combined methods of MR imaging with combined methods of CT. Am. J. Roentgenol, 174,947–954.

Kong, D., Liu, K., Wang, Z., 2009. Hyperbolic mean curvature flow: evolution of plane curves. Acta Mathematica Scientia, 29(3),439-514.

Kwak, H. S., Lee, J. M., Kim, C. S., 2004. Preoperative detection of hepatocellular carcinoma: Comparison of combined contrast-enhanced MR imaging and combined CT during arterial portography and CT hepatic arteriography. Eur. Radiology, 14, 447–457

Lafortune, M., Madore, E., Patriquin, H., Breton, G., 1991. Segmental anatomy of the liver: a sonographic approach to the Couinaud nomenclature. Radiology, 181, 443-448

Lankton, S., Melonakos, J., Malcolm, J., Dambreville, S, Tannenbaum, A., 2008. Localized statistics for DW-MRI fiber bundle segmentation. Computer Vision and Pattern Recognition Workshops, 1–8.

Lee, C. C, Chung, P. C., Tsai, H. M., 2003. Identifying multiple abdominal organs from CT image series using a multimodule contextual neural network and spatial fuzzy rules. IEEE Trans. Inf. Technol. Biomed, 7(3), 208–217.

Lee, J., Kim, N., Lee, H., Seo, J. B., Won, H. J., Shin, Y. M., Shin, Y. G., 2007. Efficient liver segmentation exploiting level-set speed images with 2.5D shape propagation. MICCAI Workshop. 3D Segmentation in the clinic: A Grand Challenge, 189-196.

Leemput, K. V., Maes, F., Vandermeulen, D., Suetens, P., 1999. Automated model-based tissue classification of MR images of the brain. IEEE Trans. Med. Imag. 18(10), 897–908

Lencioni, R., Della, P. C, Bruix, J., et al., 2005. Clinical management of hepatic malignancies: Ferucarbotranenhanced magnetic resonance imaging versus contrast-enhanced spiral computed tomography. Dig. Dis. Sci.,50,533–537.

Levinski, K., Sourin, A., Zagorodnov, V., 2009. Interactive surface-guided segmentation of brain MRI data, Computers in Biology and Medicine, 39, 1153–1160.

Leventon, M., Grimson, E., Faugeras, O., 2000. Statistical shape influence in geodesic active contour. Proc. IEEE Comput. Vis. Pattern Recognit. (CVPR), 316–322.

Li, C., Xu, C., Gui, C., Fox, M. D., 2010. Distance Regularized Level Set Evolution and Its Application to Image Segmentation. IEEE Transactions on Image Processing, 19(12), 3243-3254.

Li, C., Xu, C., Gui, C., Fox, M. D., 2005. Level set evolution without re-initialization: A new variational formulation. Proc. IEEE Conf. Computer Vision and Pattern Recognition, 1, 430–436.

Li, C. M., Kao, C., Gore, J., Ding, Z., 2007. Implicit active contours driven by local binary fitting energy. IEEE Conference on Computer Vision and Pattern Recognition, (CVPR), 1, 1–7.

Li, C., Huang, R., Ding, Z., Gatenby, J. C., Metaxas, N. D., Gore, J. C., 2011. A level set method for image segmentation in the presence of intensity inhomogeneities with application to MRI. IEEE Transactions on Image Processing, 20(7), 2007-2016

Lim, S. J., Jeong, Y. Y., Ho, Y. S., 2006. Automatic liver segmentation for volume measurement in CT images. Journal of Vis. Commun. Image Reconstruction,17, 860–875.

Lin, D. T., Lei, C. C., Hsiung, S. Y., 2003. An efficient method for kidney segmentation on abdominal CT images. 8th Australian and New Zealand Intelligent Information Systems Conference, Sydney, Australia, 75-82.

Linguraru, M. G., Sandberg, J. K., Li, Z., Shah, F., Summers R. M., 2010. Automated segmentation and quantification of liver and spleen from CT images using normalized probabilistic atlases and enhancement estimation. Med. Phys.,37(2), 771-783.

Liu, B., Cheng, H. D., Huang, J., Tian, J., Tang, X., Liu, J., 2010. Probability density difference-based active contour for ultrasound image segmentation. Pattern Recognition, 43(6), 2028–2042.

Liu, J., Hu, Q., Chen, Z., Heng, P., 2008. Adaptive liver segmentation from multi-slice CT scans. 7th Asian-Pacific Conference on Medical and Biological Engineering IFMBE Proceedings, 19(9), 381-384

Liu, H., Yan, T., Cheng, Y., Zhang, D. W., Meng, Max, Q.-H., 2012. Image segmentation by improved level set evolution algorithm. Proceeding of the IEEE International Conference on Information and Automation Shenyang, China.

Lu, D., Zhang, J., Wang, X., Fang, J., 2007. A fast and robust approach to liver nodule detection in MR images. IEEE Bioscience and Info. Tech. Conf., 493 – 497

MacQueen, J., 1967. Some methods for classification and analysis of multivariate observations. Proceedings of the Fifth Berkeley Symposium on Mathematics Statistics and Probability, 281.

Maintz , J. B. A., Viergever, M. A., 1998. A survey of medical image registration. Medical Image Analysis, 2, 1–36.

Maitra, R., 2009. Initializing partition - optimization algorithms. IEEE/ACM Transactions on Computational Biology and Bioinformatics, 6,144–157

Malladi, R., Sethian, J. A., Vemuri, B. C., 1995. Shape modeling with front propagation: A level set approach. IEEE Transactions on Pattern Analysis and Machine Intelligence, 17(2), 158–175.

Malladi, R., Sethian, J. A., 1996. Image processing: Flows under min/max curvature and mean curvature. Graphical Models and Image Processing, 58(2),127-141.

Mumford, D., Shah, J., 1989. Optimal approximations by piecewise smooth functions and associated variational problems. Communications on Pure and Applied Mathematics, 42(5), 577–685.

Marques, J., Moreno, P. J., 1999. A study of musical instrument classification using gaussian mixture models and support vector machines. Tech. rep., COMPAQ, Cambridge Research Laboratory

Massoptier, L., Casciaro, S., 2007. Fully automatic liver segmentation through graph-cut technique. IEEE EMBS 29th International Conf., 5243-5246.

Masumoto, J., Hori, M., Sato, Y., Murakami, T., Johkoh, T., Nakamura, H., Tamura, S., 2003. Automated liver segmentation using multislice CT images. Systems Comput. Jpn., 34(9), 2150–2161.

McCoy, J. A. 2009. A new class of fully nonlinear curvature flows. East Journal on Approximations, 15 (3), 349-373.

McGowan, C. J., 2008. Basic Principles of Magnetic Resonance Imaging. Neuroimag Clinics of North America, 18, 623–636.

McInerney, T., Terzopoulos, D., 2000. T-snakes: Topologically Adaptive Snakes. Med. Image Anal. 4(2),73–91.

McLachlan, G., Peel, D., 2000. Finite Mixture Models. John Wiley & Sons, New York.

McLachlan, G. J, Basford, K. E., 1988. Mixture models: Inference and applications to Clustering. New York: Marcel Dekker

McNicholas P. D., Murphy T. B., 2008. Parsimonious Gaussian mixture models. Stat.Comput., 18, 285–296.

McNicholas, P. D., Murphy, T. B., 2010. Model-based clustering of longitudinal data. Can. J. Stat., 38, 153–168.

Melnykov, V., Maitra, R., 2010. Finite mixture models and model-based clustering. Statistics Surveys, 4 (2010), 80–116, ISSN: 1935-7516, DOI: 10.1214/09-SS053

Mharib A. M., Ramli A. R., Mashohor S., Mahmood R. B., 2012. Survey on liver CT image segmentation methods. Artificial Intelligence Review, 37(2), 83-95.

Mikula, K., Sevcovic, D., 1999. Solution of nonlinearly curvature driven evolution of plane curves. Applied Numerical Mathematics, 31,191–207

Montagnat, J., Delingette, H., 1996. Volumetric medical image segmentation using shape constrained deformable models. CVRMed-MRCA, Lecture Notes in Computer Science, Springer Verlag Publisher, Berlin, 1205, 13–22.

Mojsilovic, A., Popovic, M. V., Neskovic, A. N., Popovic, A. D., 1997. Wavelet image extension for analysis and classifcation of infarcted myocardial tissue. IEEE Transactions on Biomedical Engineering, 44, 856–866.

Moore, K. L., Dalley, A. R., 1999. Clinically Oriented Anatomy, (4th Ed.), Lippincott Williams & Wilkins, Toronto.

Muller, R. D., Vogel, K., Neumann, K., et al., 1999. SPIO-MR imaging versus double-phase spiral CT in detecting malignant lesions of the liver. Acta. Radiol, 40,628–635.

Nacher, P. J., 2008. Magnetic Resonance Imaging: From Spin Physics to Medical Diagnosis. Quantum Spaces, 1-35.

Ning, J., Wu, C., Liu, S., Wen, P., 2006. A new active contour model: Curvature gradient vector flow. Computer Vision – ACCV2006, Lecture Notes in Computer Science, 3851,633-642.

Nocedal, J., Wright, S. J., 2006. Numerical Optimization, Springer Series in Operations Research, USA.

Nowozin, S., Lixu, G., 2005. A novel Liver Perfusion Analysis Method, IEEE Engineering in Medicine and Biology 27th Annual Conf., Shanghai, China, September 1-4, 3063-3066.

Osher, S., Fedkiw, R., 2002. Level set methods and dynamic implicit surfaces. New York: Springer Verlag

Osher, S., Sethian, J. A., 1988. Fronts propagating with curvature-dependent speed: Algorithms based on Hamilton–Jacobi formulation. Journal of Computational Phys., 79(1), 12–49.

Osserman, R., 1978. The isoperimetric inequality. Bullettin of the American Mathematical Society, 84(6), 1182-1238.

Ostlad, B., Tonp, A., 1996. Encoding of a priori information in active contour models. IEEE Trans. Pattern Anal. Machine Intell., 18(9),863–872.

Otsu, N., 1979. A threshold selection method from gray-level histograms. IEEE Transactions on Systems, Man and Cybernetics, 9(1),62-66.

Paragios, N., Deriche, R., 2002. Geodesic active region and level set methods for supervised texture segmentation. Int. Journal of Comput. Vision, 46(3), 223–247

Park, H., Bland, P. H., Meyer, C. R., 2003. Construction of an abdominal probabilistic atlas and its application in segmentation. IEEE Trans. on Medical Imaging, 22(4), 483-492.

Peng, D., Merriman, B., Osher, S., Zhao, H., Kang, M., 1999. A PDE-based fast local level set method. Journal of Comput. Phys., 155, 410–438.

Perona, P., Malik, J., 1987. Scale-space and edge detection using anisotropic diffusion. Proceedings of IEEE Computer Society Workshop on Computer Vision, 16–22.

Piovano, J., Rousson, M., Papadopoulo, T., 2007. Efficient segmentation of piecewise smooth images. SSVM. 709–720.

Platero, C., Gonzalez, M., Tobar, M. C., Poncela, J. M., Sanguino, J., Asensio, G., Santas, E., 2008. Automatic method to segment the liver on multi-phase MRI", Computer Assisted Radiology and Surgery (CARS), 22nd International Congress and Exhibition, Barcelona, Spain.

Poeckler, S. C., Koepke, J., Gueckel, F., et al., 1999. MRI with superparamagnetic iron oxide: Efficacy in the detection and characterization of focal hepatic lesions. Magn Reson Imaging, 17,383–392.

Pohle, R., Toennies, K. D., 2001a. Segmentation of medical images using adaptative region growing. Proc. SPIE Medical Imaging, 2(27), 1337-1346.

Pohle, R., Toennies, K. D., 2001b. A new approach for model-based adaptive region growing in medical image analysis. 9th International Conference on Computer Analysis of Images and Patterns, Warsaw, Poland, 2124, 238–246.

Pohle, R., Toennies, K. D., 2001c. Self-learning model-based segmentation of medical images. Image Processing & Communication, 7, 97–113.

Positano, V., Salani, B., Scattini, B., Santarelli, M. F., Ramazzotti, A., Pepe, A., Lombardi L. M. L., 2007. A robust method for assessment of iron overload in liver by MRI. IEEE Eng. in Medicine and Biology Conf., 2895-2898.

Prakash, K.N., Zhou, S., Morgan, T.C., Hanley, D.F., Nowinski, W. L., 2012. Segmentation and quantification of intra-ventricular/cerebral hemorrhage in CT scans by modified distance regularized level set evolution technique. Int. J. Comp. Assist. Radiology Surg., 7(5),785-798.

Rada, L., Chen, K., 2012. A new variational model with dual level set functions for selective segmentation. Commun. Comput. Phys., 12(1), 261-283.

Rafiee, A., Masoumi, H., Roosta, A., 2009. Using neural network for liver detection in abdominal MRI images. IEEE Int. Conf. on Signal and Image Proc. Lumpur, 21-25.

Reynolds, D., Rose, R., 1995. Robust text-independent speaker identification using gaussian mixture speaker models. IEEE Transactions on Speech and Audio Processing, 3(1), 72–83.

Robinson, P. J. A., Ward, J., 2006. MRI of the liver - A practical guide. Taylor & Francis Group, New York, Published by e-man, ISBN: 0824728718, NY 10016.

Ronfard, R., 1994. Region-based Strategies for Active Contour Models. Int. Journal of Computer Vision, 13(2), 229–251.

Rosenblatt, F., 1958. The Perceptron: A probabilistic model for information storage and organization in the brain. Cornell Aeronautical Laboratory, Psychological Review 65(6), 386-408.

Rousson, M., Paragios, N., 2002. Shape priors for level set representations. Proceedings of the Seventh European Conference on Computer Vision (ECCV), 78–92.

Ruskó, L., Bekes, G., Németh, G., Fridrich, M., 2007. Fully automatic liver segmentation for contrast-enhanced CT images. MICCAI Wshp. 3D Segmentation in the Clinic: A Grand Challenge, 143-150.

Ruskó, L., Bekes, G., 2010. Liver Segmentation for Contrast-enhanced MR Images Using Partitioned Probabilistic Model. International Journal of Computer Assisted Radiology and Surgery (CARS), 5, 1861-6410.

Russo, G., Smereka, P., 2000. A Remark on computing distance functions. Journ. Comput. Phys., 163, 51-67.

Rutkauskas, S., Gedrimas, V., Pundzius, J., Barauskas, G., Basevicius, A., 2006. Clinical and anatomical basis for the classi_cation of the structural parts of liver. Medicina, 42(2), 98-106.

Sandeep, V. M., Kulkarni, S., Kohir, V., 2011. Level set issues for efficient image segmentation. International Journal of Image and Data Fusion, 2(1), 75-92.

Sapiro, G., 2001. Geometric partial differential equations and image analysis, chp. 2, Cambridge University Press, Cambridge, UK.

Sefidpour, A., Bouguila, N., 2012. Spatial color image segmentation based on finite non-Gaussian mixture models. Expert Systems with Applications, 39(10), 8993–9001

Semelka, R. C., Cance, W. G., Marcos, H. B., Mauro, M. A., 1999. Liver Metastases: Comparison of current MR techniques and spiral CT during arterial portography for detection in 20 surgically staged cases. Radiology, 213,86–91.

Seneterre, E., Taourel, P., Bouvier, Y., et al., 1996. Detection of hepatic metastases: Ferumoxides-enhanced MR imaging versus unenhanced MR imaging and CT during arterial portography. Radiology, 200,785–792.

Selver, M. A., Kocaoğlu, A., Demir, G. K., Doğan, H., Dicle, O., Güzeliş, C., 2008. Patient oriented and robust automatic liver segmentation for pre-evaluation of liver transplantation. Computers in Biology and Medicine, 38, 765 – 784.

Sethian, J. A., 1999. Level set methods and fast marching methods. Cambridge, U.K.: Cambridge Univ. Press, Chp. 2,15-73.

Sethian, J. A., 2001. Evolution, implementation, and application of level set and fast marching methods for advancing fronts. Journal of Computational Physics, 169, 503–555.

Shi, Y., Karl, W. C., 2008. A real-time algorithm for the approximation of level-set based curve evolution. IEEE Trans. Image Process., 17, 645-656.

Shitong, W., Duan, F., Min, X., Dewen, H., 2007. Advanced fuzzy cellular neural network: Application to CT liver images. Artificial Intelligence in Medicine, 39, 65-77.

Siebenthal, M. V., 2008. Analysis and Modelling of Respiratory Liver Motion using 4D MRI, Phd Thesis in Electrical Engineering and Information Technology, ETH Zurich.

Simmons, A., Tofts, P. S., Barker, G. J., Arridge, S. R., 1994. Sources of intensity nonuniformity in spin echo images at 1.5T. Magnetic Resonance in Medicine, 32, 121–128.

Skandalakis, J. E., Skandalakis, L. J., Skandalakis, P. N., Mirilas, P., 2004. Hepatic surgical anatomy. Surg Clin North Am. Apr.,84(2), 413-435.

Slone, R. M., Fisher, A. J., Pickhardt, P. J., Gutierrez, F. R., Balfe, D. M., 2000. Body CT: A practical approach. New York: McGraw-Hill.

Soler, L., Delingette, H., Malandain, G., Montagnat, J., Ayache, N., Koehl, C., Dourthe, O., Malassagne, B., Smith, M., Mutter, D., Marescaux, J., 2005. Fully automatic anatomical, pathological and functional segmentation from CT scans for hepatic surgery. Acad. Radiol., 12, 1178–1189.

Spiegel, M., Hahn, D. A., Daum, V., Wasza, J., Hornegger, J., 2009. Segmentation of kidneys using a new active shape model generation technique based on non-rigid image registration. Computerized Medical Imaging and Graphics, 33, 29–39.

Stewart, J., 2003. Calculus, Academic Internet Publishers, 5th edition, ISBN: 9780534393397, 29, pg.8.

Strzelecki, M., Certaines, J., Ko, S., 2007. Segmentation of 3D MR liver images using synchronised oscillators network. IEEE, Info. Tech. Conf., 259-263.

Sussman, M., Fatemi, E., 1999. An efficient, interface-preserving level set redistancing algorithm and its application to interfacial incompressible fluid flow. SIAM J. Sci. Comput., 20(4), 1165–1191.

Sussman, M., Smereka, P., Osher, S., 1994. A level set approach for computing solutions to incompressible two-phase flow. Journ. Comp. Phys., 114, 146-159.

Suzuki, K., Kohlbrenner, R., Epstein, M. L., Obajuluwa, A. M., Xu, J., Hori, M., 2010. Computer-aided measurement of liver volumes in CT by means of geodesic active contour segmentation coupled with level-set algorithms. Med. Phys. 37(5), 2159-2166.

Tang, S., Wang, Y., 2010. MR-guided liver cancer surgery by nonrigid registration. IEEE International Conf. on Medical Image Analysis and Clinical Application (MIACA), 113-117.

Tang, Y., Jackson, H., Lee, S., Nelson, M., Moats, R. A., 2009 Shape-aided kidney extraction in MR urography. 31st Annual International Conference on Engineering in Medicine and Biology Society (EMBS), IEEE Press, Minneapolis, 5781-5784.

Thieu, Q. T., Luong, M., Rocchisani, J. M., Viennet, E., Tran, D., 2011. Novel Convex Active Contour Model Using Local and Global Information. International Conference on Digital Image Computing, Techniques and Applications, 346-351.

Titterington, D. M., Smith, A. F. M, Makov, U. E., 1985. Statistical analysis of finite mixture distributions. Chichester, U.K. Wiley

Tsagaan, B., Shimizu, A., Kobatake, H., Kunihisa, M., Hanzawa, Y., 2001. Segmentation of kidney by using a deformable model. ICIP: International conference on image processing, IEEE Press, Greece, 1059–1062

Tsagaan, B., Shimizu, A., Kobatake, H., Miyakawa, K., 2002. An automated segmentation method of kidney using statistical information. Proceedings of the 5th International Conference on Medical Image Computing and Computer Assisted Intervention - MICCAI 2002. LNCS, Springer, Heidelberg,2488, 556–563.

Tsai, D., 1994. Automatic segmentation of liver structure in CT images using a neural network. IEICE Trans. Fundamentals E77-A, 11, 1892–1895.

Vese, L. A., Chan, T. F., 2002. A multiphase level set framework for image segmentation using the mumford and shah model. Int. J. Comput. Vis., 53(3), 271–293.

Vilarino, D. L., Brea, V. M., Cabello, D., Pardo, J. M., 1998. Discrete-time CNN for image segmentation by active contours. Pattern Recognition Letters, 19, 721–734.

Vincent, L., 1993. Morphological grayscale reconstruction in image analysis: Applications and efficient algorithms. IEEE Trans. Image Process. 2(2), 176–201.

Yan, G., Wang, B., 2010. An automatic kidney segmentation from abdominal CT images. Intelligent Computing and Intelligent Systems (ICIS), IEEE International Conference, 1, 280-284.

Yang, G., Zhou, G. T., Yin, Y., Yang, X., 2010. K-means based fingerprint segmentation with sensor interoperability sensor interoperability. EURASIP Journal on Advances in Signal Processing

Yang, F., Qin, W., Xie, Y., Wen, T., Gu, J. 2012. A shape-optimized framework for kidney segmentation in ultrasound images using NLTV denoising and DRLSE. Biomedical engineering online, 11(1), 82.

Yezzi, A., Mennucci, A., 2005. Metrics in the space of curves. ArXiv:math.DG/ 0412454, 2.

Yijun, H., Guirong, W., 2009. Segmentation of cDNA microarray spots using k-means Clustering Algorithm and Mathematical Morphology. WASE International Conference on Information Engineering (ICIE 2009), Shanxi, China, Vol. 2.

Yuan, Y., He, C., 2012. Variational level set methods for image segmentation based on both L2 and Sobolev gradients, Nonlinear Analysis: Real World Applications, 13(2), 959–966

Web1.2012. http://medical-dictionary.thefreedictionary.com

Wang, X., Zheng, C., Li, C., Yin, Y., Feng, D. D., 2011. Automated CT liver segmentation using improved Chan-Vese model with global shape constrained energy. 33rd Annual International Conference of the IEEE EMBS, Boston, Massachusetts USA.

Wang, X., He, L., Wee, W. G., 2004a. Deformable contour method: a constrained optimization approach. Int. Journal of Comput. Vis., 59 (1), 87–108.

Wang, Z., Bovik, A. C., Sheikh, H. R., Simoncelli, E. P., 2004b. Image quality assessment: From error visibility to structural similarity. IEEE Transactions on Image Processing, 13(4), 600-612.

Wang, L., Chen, Y., Pan, X., Hong, X., Xia, D., 2010. Level set segmentation of brain magnetic resonance images based on local Gaussian distribution fitting energy. Journal of Neuroscience Methods 188, pp 316–325.

Ward, J., Robinson, P. J., 2001. Combined use of MR contrast agents for evaluating liver disease. Magn. Reson. Imaging Clin. N. Am., 9,767–802.

Ward, J., Robinson, P. J., Guthrie, J. A., et al., 2005. Liver metastases in candidates for hepatic resection: Comparison of helical CT and gadolinium-and SPIO-Enhanced MR imaging. Radiology, 237,170–180.

Ward, J., Guthrie, J. A., Wilson, D., et al., 2003. Colorectal hepatic metastases: Detection with SPIO-enhanced breathhold MR imaging - Comparison of optimized sequences. Radiology, 228,709–718.

Weeratunga, S. K., Kamath, C., 2004. An investigation of implicit active contours for scientific image segmentation. San Jose, CA, USA, 210-221.

Whitaker, R., 1998. A level-set approach to 3D reconstruction from range data. Int. J. Comput. Vis., 29(3), 203–231.

Williams, D. J., Shah, M. A., 1992. Fast algorithm for active contours and curvature estimation. CVGIP Image Understand., 55(1),14–26.

Wu, C., Tai, X. 2010. A level set formulation of geodesic curvature flow on simplicial surfaces. IEEE Transactions on Visualization and Computer Graphics, 16(4),647-662.

Xie, X., 2010. Active contouring based on gradient vector interaction and constrained level set diffusion. IEEE Trans. Image Processing, 19(1), 154-164.

Xu, C., Pham, D. L., Prince, J. L., 2000. Medical Image Segmentation Using Deformable Models. Handbook of Medical Imaging,SPIE Press, Medical Image Processing and Analysis,3,129–174

Xu, C., Prince, J. L., 1998a. Snake, Shapes, And Gradient Vector Flow. IEEE Trans. Image Process., 7(3), 359–369.

Xu, C., Prince, J. L., 1998b. Generalized gradient vector flow external forces for active contours. Signal Process., 71(2), 131–139.

Xu, C., Yezzi, A., 2000. On the relationship between parametric and geometric active contours. Thirty-Fourth Asilomar Conference on Signals, Systems and Computers, 483-489.

Zeng, Z. G., Ding, L. X., Yi, S. Q., Zeng, S. Y., Qiu, Z. H., 2011. Video image segmentation using Gaussian mixture models based on the differential evolution-based parameter estimation. Key Engineering Materials, 442-447.

Zhang, Y., 2006. Advances in image and video segmentation. Hershey, PA:IRM Press, Chp.1, 1-15.

Zhang, K., Zhang, L., Song, H., Zhou, W., 2010. Active contours with selective local or global segmentation: A new formulation and level set method. Image and Vision Computing, 28(4), 668–676.

Zhang, J., Chen, K., Yu, B., 2012. A 3D multi-grid algorithm for the Chan–Vese model of variational image segmentation. International Journal of Computer Mathematics, 89(2), 160-189.

Zhao, H., Chan, T., Merriman, B., Osher, S., 1996. A variational level set approach to multiphase motion. Journ. Comp. Phys., 127, 179-195.

Zhu, H., Barish, M., Pickhardt, P., Liang, Z. 2013. Haustral Fold Segmentation With Curvature-Guided Level Set Evolution. IEEE Transactions on Biomedical Engineering, 60,321-331.

Zhu, S. C., Yuille, A., 1996. Region competition: Unifying snakes, region growing, and Bayes/MDL for multiband image segmentation. IEEE Trans. Pattern Anal. Machine Intell., 18(9), 884–900.

APPENDIX A

PRINCIPLE DEFINITIONS AND A SHORT REVIEW OF DIFFERENTIAL GEOMETRY OF CURVES

A.1. Lebesgue Integration Theory

We define domain as a Lebesgue-measurable (closed or open) subset of $\mathbb{R}^n$ with non-empty interior. We denote the Lebesgue integral of function *f* on a given domain Ω by $\int_\Omega f(x)dx$. Let $\|f\|_{L^p(\Omega)} := \left(\int_\Omega f^p dx\right)^{\frac{1}{p}}$ for $1 \le p < \infty$. Then, the definition of the Lebesgue space is $L^p(\Omega) := \left\{ f(x) : \|f\|_{L^p(\Omega)} < \infty \right\}$.

A.2. Inner-Product Spaces

A bilinear form, $b\langle \cdot, \cdot \rangle$, on a linear space *V* is a mapping $b : V \times V \to \mathbb{R}$ such that each of the maps $v \to b\langle v, w \rangle$ and $w \to b\langle v, w \rangle$ is a linear form on *V*. It is symmetric when $b\langle v, w \rangle = b\langle w, v \rangle$ for $\forall v, w \in V$. An inner product $b\langle \cdot, \cdot \rangle$ is a symmetric bilinear form on a linear space *V* that satisfies $\langle v, v \rangle \ge 0 \ \forall v \in V$ and $\langle v, v \rangle = 0 \leftrightarrow v = 0$.

A linear space *V* (i.e. $x, y \in V \Rightarrow x + y \in V,$ and $kx \in V$ for all $k \in \mathbb{R}$) together with an inner product defined on it is called an inner-product space and is denoted by $\left(V, \langle \cdot, \cdot \rangle\right)$. Example inner-product spaces are,

$$V = \mathbb{R}^n, \ \langle x, y \rangle := \sum_{i=1}^{n} x_i y_i \tag{A.1}$$

$$V = L^2(\Omega), \ \Omega \subseteq \mathbb{R}^n, \langle u, v \rangle_{L^2(\Omega)} := \int_\Omega u(x) v(x) dx \tag{A.2}$$

Geometric active contours usually use Lebesgue (L^2) type inner product.

A.3. Norm and Distance (metric) for points

We define a norm $\|\cdot\|$ on a given vector (linear) space V as a function on V with non-negative real values having following properties:

1. $\|v\| \geq 0 \ \forall v \in V, \ \|v\| = 0 \Leftrightarrow v = 0$ (A.3)
2. $\|c \cdot v\| = |c| \cdot \|v\| \quad \forall c \in \mathbb{R}, v \in V$ (A.4)
3. $\|v + w\| \leq \|v\| + \|w\| \quad \forall v, w \in V$ (the triangle inequality) (A.5)

We define metric, or distance, for points $v, w \in V$ as $d\langle v, w\rangle = \|v - w\|$

A.4. Completeness of a Metric Space

A metric space is called complete if every Cauchy sequence $\{v_j\} \in V$ has a limit $v \in V$. For a normed linear space a Cauchy sequence is one such that $\|v_j - v_k\| \to 0$ as $j, k \to \infty$. If $\|v - v_j\| \to 0$ as $j \to \infty$ then the normed linear space is complete.

A.5. Hilbert Spaces

A Hilbert space H is a vector space with an inner product $\langle f, g\rangle$ such that the norm defined by $|f| = \sqrt{\langle f, f\rangle}$ turns H into a complete metric space. Therefore, we can say that any inner-product space $(V, \langle\cdot,\cdot\rangle)$ is a Hilbert space if the associated normed linear space $(V, \|\cdot\|)$ is complete. An example Hilbert space is $V = \mathbb{R}^n$, $\langle x, y\rangle \coloneqq \sum_{i=1}^{n} x_i y_i$.

A.6. Curve Definition and Plane Curves

There are two ways of considering plane curves. One of them is to consider as a set of points in the plane, which is a geometric view. The other considering is as a function from an interval to $\mathbb{R}^2$, which are parameterized curves and much easier than the geometric view to use in practice.

A plane curve is the graph of a function given in the *xy*-plane. Vertical line test is used to decide whether a given curve corresponds to the graph of a function or not. Because, the vertical line test, which is shown in Figure A.1, says that if there is not any vertical line that intersects a curve more than one time then the curve in the *xy*-plane is defined as the graph of a function of *x*. If every vertical line $x=a$ intersects a curve only one time, at (a,b), then only one functional value can be defined as $f(a)=b$. However, the curve can not represent a function when a line $x=a$ intersects the curve two times, at (a,c) and (a,b), since assignment of two different values to a point by a function is not possible (Stewart 2003).

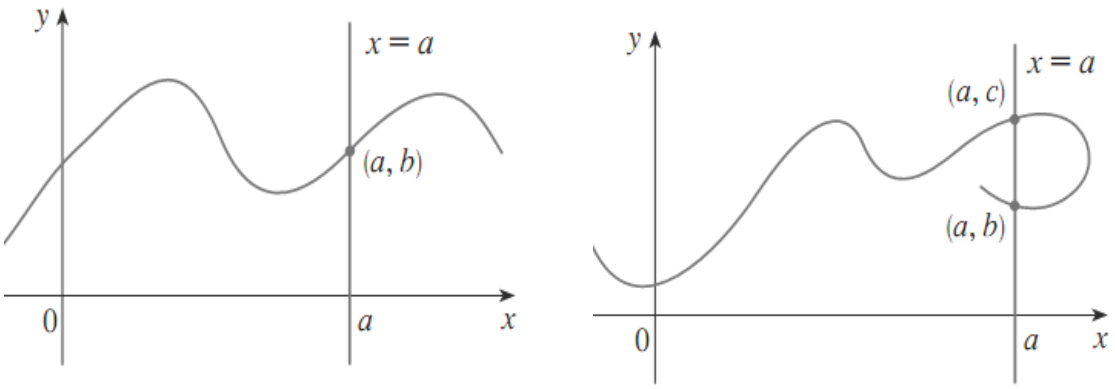

Figure A.1. Vertical Line Test

(Source: Stewart 2003)

A.7. Parametric Representation of Curves

Coordinates of a point on the curve is specified by using separate functions of an other variable, which is called as a parameter, in parametric representation of curves.

Imagine as shown in Figure A.2 that a particle is moving on a curve. The curve C does not provide the Vertical Line Test. Therefore, this curve can not be defined as $y=f(x)$. However, it is possible to write $x=f(t)$ and $y=g(t)$ since the coordinates are functions of time. Each point (x,y) is determined by values of the variable *t*. Therefore, the points $(x,y)=(f(t),g(t))$ corresponds to a curve that is called as a parametric curve (Stewart 2003).

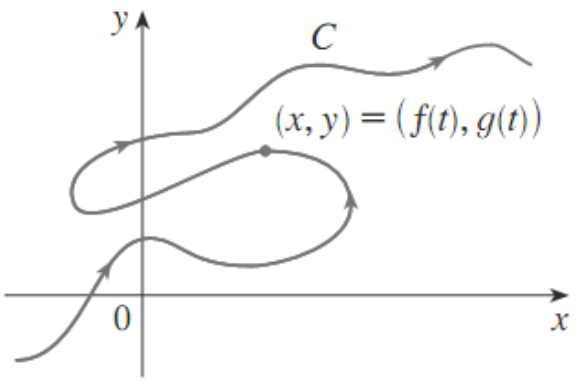

Figure A.2. A moving particle on a curve

(Source: Stewart 2003)

Parametric curves represent points with a vector-valued function by using a scalar parameter. The main drawback of parameterized curves is their non-intrinsic property, which means that there might be two different parametric curves of the same set. Therefore, an equivalent relation is required for the parametric curves. There is only one curve that is parametrized by arc-length has intrinsic properties.

If a curve does not intersect itself then it is called as simple. Assume that a simple parametric curve is given as $C(p)=\{x(p),y(p)\}$, where $p\in[0,1]$. The curve maps the interval $I=[0,1]$ to the Euclidean plane R^2. *C(p)* corresponds to a coordinate point on the curve for each value of the parameter *p* along the curve.

The tangent (velocity) vector is the first derivative of the curve *C(p)* and represented as,

$$\vec{T}=\frac{\partial C(p)}{\partial p}=C_P=\left\{x_p,y_p\right\} \tag{A.6}$$

The unit tangent vector is the normalization written as,

$$\vec{T}=\frac{T}{|T|}=\frac{\{x_p,y_p\}}{\sqrt{x_p^2+y_p^2}} \tag{A.7}$$

Similarly, the unit normal vector, which can be obtained by changing the sign and position of the arguments of a given tangent vector, is written as,

$$\vec{N}=\frac{\{-y_p,x_p\}}{\sqrt{x_p^2+y_p^2}} \tag{A.8}$$

The inner product of the normal and tangent vector is,

$$\left\langle \vec{T}, \vec{N} \right\rangle = x_p \frac{-y_p}{|C_p|} + y_p \frac{-x_p}{|C_p|} = 0 \tag{A.9}$$

A.8. Arc-length Parameterization

Consider a curve, $C(p) = \{x(p), y(p)\}$, shown in Figure A.3 that have two points A and B with coordinates $[x_A, y_A]$ and $[x_B, y_B]$. The distance between these two points is obtained by approximating the curve by a polygon with straight lines and then taking a limit as the number of segments of the polygon is increased.

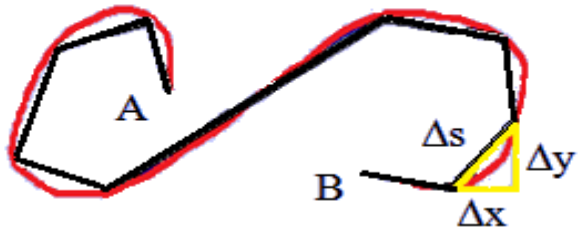

Figure A.3. Approximate with straight lines

The length of a line segment shown in Figure 2.9 is written as,

$$\Delta s = \sqrt{(\Delta x)^2 + (\Delta y)^2} \tag{A.10}$$

Sum of lengths of lines can be written as,

$$\sum_k \sqrt{(x_{k+1} - x_k)^2 + (y_{k+1} - y_k)^2} \tag{A.11}$$

Therefore, the length between the points A and B can be obtained by rewriting the sum in a more convenient form and passing to the limit as $p \rightarrow 0$ that gives,

$$\sum_k \sqrt{\left(\frac{x_{k+1} - x_k}{\Delta p}\right)^2 + \left(\frac{y_{k+1} - y_k}{\Delta p}\right)^2} \Delta p \rightarrow \int_{p_A}^{p_B} \sqrt{\left(\frac{dx}{dp}\right)^2 + \left(\frac{dy}{dp}\right)^2} dp \tag{A.12}$$

Let $s(p)$ denotes the length from the p_0 as

$$s(p) = \int_{p_A}^{p_B} \|C_p(p)\| dp = \int_{p_0}^{p_B} |C_p(p)| dp = \int_{p_0}^{p_B} \sqrt{\left(\frac{dx}{dp}\right)^2 + \left(\frac{dy}{dp}\right)^2} dp \tag{A.13}$$

Then, the change rate of arc-length is,

$$\frac{ds}{dp} = \sqrt{\left(\frac{dx}{dp}\right)^2 + \left(\frac{dy}{dp}\right)^2} = \left|\frac{dC}{dp}\right| = \left\|C_p(p)\right\| \tag{A.14}$$

It is clear that the function *s* maps the interval of *p*, which is given as *I=[0,1]*, to another interval, which is *[0,L]* where *L* is the total length. The *s(p)* is an increasing function, i.e. $|C_p| > 0,$ and $s:[0,1] \to [0,L]$ is one-to-one. Therefore, the inverse function *p(s)* exists. Now, it is possible to change the curve parameter to the arc-length parameter as follows, since the distance measure is intrinsic,

$$C(p(s)) = C(s) = [x(s), y(s)] \tag{A.15}$$

The arc-length tangent vector has always unit length, $|C_s| = 1,$ (i.e. the speed along the curve is one, which means that C_s always lies on a unit circle), which can be proved by applying the chain rule as,

$$C_s = \frac{dC}{ds} = \frac{dC}{dp}\frac{dp}{ds} = \frac{\frac{dC}{dp}}{\left|\frac{dC}{dp}\right|} = \frac{C_p}{|C_p|} = \vec{T}(s) \tag{A.16}$$

Therefore, the arc-length parametrization has a special importance among all possible parametrizations. The arc-length parameterization and the curve derivatives according to it are intrinsic, geometric and invariant to Euclidean transformation of the coordinates (Kimmel 2003).

A.9. Curve Evolution Theory

In this section, motion of curves is explained by adding a new variable (*t*) to the curve and assuming that the curve is the first in a family of curves, *C(p,t)=(x(p,t), y(p,t))*. Differentiation of a curve gives the velocity of the motion. The following differential equation describes motion of a curve.

$$\frac{\partial C(p,t)}{\partial t} = \vec{V}(p,t) \tag{A.17}$$

Figure A.4 shows the points on the initial curve *A* move to *B* to generate a new curve. Assume that each point of the curve in Figure A.4.a move by some arbitrary

amount in some arbitrary direction. Figure A.4.b shows the tangent and normal vector components of a velocity vector $\vec{V}$.

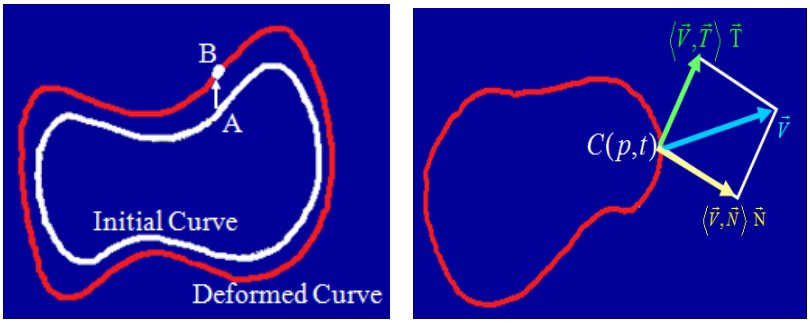

Figure A.4. Motion of a point from A to B (a); Vectors at a point on the curve (b)

Therefore, the curve evolution is described by,

$$\frac{\partial C}{\partial t} = \alpha \vec{T} + \beta \vec{N} \tag{A.18}$$

$$C_t(p,t) = \left\langle \vec{V}, \vec{N} \right\rangle \vec{N} + \left\langle \vec{V}, \vec{T} \right\rangle \vec{T} = \vec{V}_N \vec{N} + \vec{V}_T \vec{T} \tag{A.19}$$

Here, $\vec{T}$ is tangent vector, $\vec{N}$ is outward normal vector, $\vec{V}_N$ is the normal velocity component, $\vec{V}$ is the tangential velocity component, α and β are arbitrary functions.

The Epstein-Gage lemma (Epstein and Gage 1987) proves that the family of curves *C(p,t)* that evolves by the equation $C_t = \vec{V}_N \vec{N} + \vec{V}_T \vec{T}$, where the normal component does not depend on the parameterization, can be converted to $C_t = \vec{V}_N \vec{N}$. This means that a curve evolving under a velocity vector $\vec{V}(\vec{V} = \vec{V}_N \vec{N} + \vec{V}_T \vec{T})$, gives the same curves when it is evolved under only the component of normal velocity. The tangential velocity component $\vec{V}_T$, which does not affect the shape (geometry) of the evolving curve, influences only the parameterization. This result is considered as an evidence of the level set implementation for a geometric curve evolution and only the normal projection of the gradient is used.

A.10. Definition of the Gradient

Assume that ϕ is a real-valued function on R^n for a positive integer n and $x = (x_1, x_2, ...x_n) \in R^n$. Then the gradient is defined as the function written by,

$$\nabla\phi(x)=\left(\frac{\partial\phi}{\partial x_1},\frac{\partial\phi}{\partial x_2},.....,\frac{\partial\phi}{\partial x_n}\right) \tag{A.20}$$

on R^n. An equivalent definition (or a property of the gradient) is that the gradient is the element of R^n such that it satisfies the following equation,

$$d\phi(x)\cdot h=\langle h,\nabla\phi(x)\rangle,\quad h\in R^n \tag{A.21}$$

For $x\in R^n$. Here,

$$d\phi(x)\cdot h=\lim_{t\to 0}\frac{(\phi(x+th)-\phi(x))}{t},\quad x,h\in R^n \tag{A.22}$$

and $\langle\cdot,\cdot\rangle$ denotes the inner product on R^n. The gradient definitions in (A.20) and (A.21) are equivalent in Hilbert spaces as in R^n.

A.11. Gradient on the Manifold of Curves in Hilbert Spaces

Let assume that *M* is a differentiable manifold and denotes a space of immersed curves in R^2. Let T_cM be the tangent space of the manifold *M* at a curve *c* for $c\in M$. The tangent space shows valid smooth perturbations of curves by the function $h:S^1\to R^2$, where $S^1\subset R^2$ is the circle. Also, assume energy functional is given by $E:M\to R$. For a curve $c\in M$ and $h\in T_cM$, the variation (or differentiation at *c*) of the energy function *E* in the direction *h* is given by

$$dE(c)\cdot h=\frac{d}{dt}E(c+th)\Big|_{t=0} \tag{A.23}$$

Here, $(c+th)(\theta):=c(\theta)+th(\theta)$ and $\theta\in S^1$. Let $\langle\cdot,\cdot\rangle_c$ is an inner product on the tangent space T_cM at *c*. There is a unique gradient, which is a vector field $\nabla E(c)\in T_cM$, according to the Reisz representation theorem which satisfies that

$$dE(c)\cdot h=\langle h,\nabla E(c)\rangle_c \tag{A.24}$$

for all $h\in T_cM$, where $dE(c)\cdot h$ is the directional derivative. Therefore, gradient is interpreted as the most efficient perturbation of the curve. In other words, maximization

of the change in energy for each cost of perturbation is presented by the gradient (Yezzi and Mennucci 2005).

Assume that $\|\cdot\|_c$ is the norm obtained from the inner product $\langle\cdot,\cdot\rangle_c$ on tangent space. If $dE(c) \neq 0$ and $\nabla E(c)$ exists then the following problem,

$$\sup_{\{h \in T_c M,\ \|h\|_c = 1\}} dE(c) \cdot h = \sup_{\{k \in T_c M,\ k \neq 0\}} \frac{dE(c) \cdot k}{\|k\|_c} \tag{A.25}$$

yields a unique solution that is

$$k = \nabla E(c) \in T_c M, \quad h = k / \|k\| \tag{A.26}$$

Because, we can write by the Cauchy-Schwartz inequality that

$$dE(c) \cdot h = \langle \nabla E(c), h \rangle_c < \|\nabla E(c)\|_c \|h\|_c \tag{A.27}$$

Also, $dE(c) \cdot \nabla E(c) = \|\nabla E(c)\|_c^2$. Therefore, if $\nabla E(c)$ exists then we have that $k = \nabla E(c)$ attains the supremum as given in (A.23).

Studies on geometric active contours usually use Lebesgue (L^2) type inner product (A.2) that can be written by using *h(s)* and *k(s)* as,

$$\langle h, k \rangle_{L^2} := \int_c h(s) \cdot k(s) ds \tag{A.28}$$

where $h, k \in T_c M$, which are written as parameterized by the arc-length parameter *s*.

A.12. Steepest Descent (Gradient Descent Flow)

A gradient of a function gives the direction of the greatest increase in the argument of the function for each unit change. It is easy to prove this statement. Let we have the inner product $\langle \nabla E(c), h \rangle$ and the norm $\|h\| = 1$ is the rate of change in an energy function *E(c)* in the direction *h*. Then, we can write by Cauchy-Schwarz inequality that

$$\langle \nabla E(c), h \rangle \leq \|\nabla E(c)\| \tag{A.29}$$

However, if $h = \dfrac{\nabla E(c)}{\|\nabla E(c)\|}$ then we have

$$\left\langle \nabla E(c), \frac{\nabla E(c)}{\|\nabla E(c)\|} \right\rangle = \|\nabla E(c)\| \tag{A.30}$$

Therefore, the most rapid decrease in the function is opposite direction to the gradient. The line search method is generally written as,

$$c_{k+1} = c_k + \lambda_k d_k \quad \text{for } k=0,1,2,\ldots\ldots \tag{A.31}$$

Where d_k is the descent direction, λ_k is the step size that can be obtained by many different ways. Also, $E(c_k + \lambda_k d_k) < E(c_k)$. The term d_k satisfies the condition that

$$d_k^T \nabla E(c_k) < 0 \tag{A.32}$$

The descent direction for steepest descent in Euclidean space is $-\nabla E(c)$. Therefore, the gradient flow is known as steepest descent flow or gradient descent flow and it is written by,

$$c_{k+1} = c_k - \lambda_k \nabla E(c_k) \tag{A.33}$$

If $\|c_{k+1} - c_k\| < \varepsilon$ then we have a solution; else we put $c_k = c_{k+1}$ and repeat the computation.

Steepest descent (Necedal and Wright 2006) is a widely used line search technique for finding a relative minimum or maximum of a function. Solution of differential equations by using steepest descent requires that we find a function whose minimum values are solutions to the differential equation.

VITA

EVGİN GÖÇERİ

EDUCATION

[2007 – 2013] Ph.D.

Izmir Institute of Engineering and Science

Department of Electrical and Electronics Engineering, İzmir, Turkey

Dissertation : A Comparative Evaluation for Liver Segmentation from SPIR Images and A Novel Level Set Method Using Signed Pressure Force Function

[2004 - 2006] M.Sc.

XIOS Limburg

Department of Industrial Science and Technology, Hasselt, Belgium [2005 – 2006]

Pamukkale University

Department of Computer Engineering, Denizli, Turkey [2004 – 2005]

[1998 – 2002] B.Sc.

Ege University, Department of Computer Engineering, Denizli, Turkey

WORK EXPERIENCE

[2007 - Present] Instructor

Pamukkale University, Department of Computer Engineering, Denizli, Turkey

[2004 - 2007] Research Assistant

Pamukkale University, Department of Computer Engineering, Denizli, Turkey

[2002 - 2003] System Analyst

Aydınel Textile A.Ş., System Department, İzmir, Turkey

[2001 - 2001] Trainee & Web Developer

Pınar Süt Mamulleri Gıda Sanayi A.Ş., İzmir, Turkey

[1999 - 2001] Trainee & Software Developer

YGM (Software Development Center), İzmir, Turkey